A Full Core Resonance Self-shielding Method Accounting for Temperature-dependent Fuel Subregions and Resonance Interference

by

Yuxuan Liu

A dissertation submitted in partial fulfillment
of the requirements for the degree of
Doctor of Philosophy
(Nuclear Engineering and Radiological Sciences)
in the University of Michigan
2015

Doctoral Committee:

Professor William R. Martin, Chair
Professor Thomas J. Downar
Professor Shravan Veerapaneni
Distinguished Research Staff Mark L. Williams, Oak Ridge National Laboratory
Research Scientist Yunlin Xu, Argonne National Laboratory

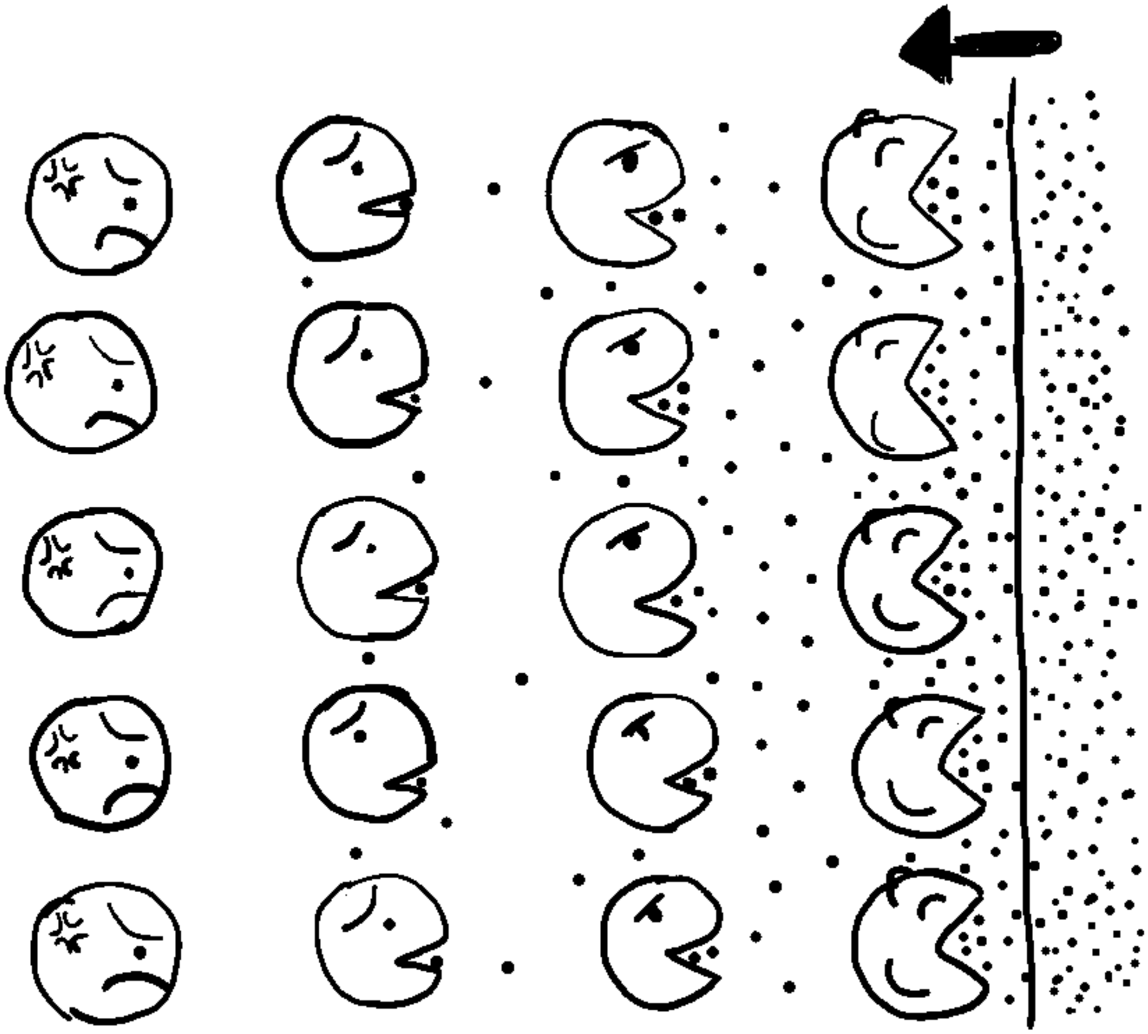

Image courtesy of Yu Fang

To: Yu and my parents,
for your love and endless support

Acknowledgements

I feel fortunate to work with my advisor Professor William Martin over the past four years. Professor Martin not only taught me the academic skills to conduct research, his character of being generous to others but strict to himself also had a great impact on my perspective of life. I appreciate all his mentoring, support and patience throughout the way of this process. I am also grateful to other members of my PhD committee, Professor Thomas Downar, Professor Shravan Veerapaneni, Dr. Mark Williams and Dr. Yunlin Xu for being a great source of feedback in the development of this work.

I must acknowledge CASL program, not only for funding this research, but also for embracing many excellent researchers to work together with students. I owe an enormous debt to Dr. Mark Williams and Dr. Kang-Seog Kim of Oak Ridge National Laboratory, who had me as a summer intern in 2012. This experience was so irreplaceable to me that I can easily find many points in this thesis that I would hardly understand without their generous help.

I also would like to thank Professor Han Gyu Joo who taught me the fundamentals of this topic. His lectures of NERS 561 were so excellent that I still remember the thousands of lines of codes he encouraged us to write, which turned out to be precious sources for later research. I also feel in indebted to Dr. Yunlin Xu for his insight of this topic which prevented me from deviating too much from the unknown truth.

Many thanks are given to my officemates who created a wonderful environment for study and communication. Special thanks go to Dr. Ben Collins, Dr. Brendan Kochunas, Dr. Zhouyu Liu, Dr. Adam Nelson, Jipu Wang, Mitch Young and Ang Zhu, who had provided many insights and advices on my study.

At last, I feel I should save a concluding paragraph to thank my family. Yu, everything becomes so dull without your love and smile. My parents, please forgive me for being many thousands miles away from you for pursuing the PhD study. Your loves are definitely the reason that makes me striding without any hesitation.

Table of Contents

List of Tables

List of Figures

List of Appendices

Abstract

This work presents a new resonance self-shielding method for deterministic neutron transport calculation. The new method is a fusion of two types of conventional methods, direct slowing-down equation and integral table based methods. The direct slowing-down method is essentially accurate in terms of using continuous-energy cross section data but is computationally expensive for the reactor assembly or whole core calculation. The integral table based methods use pre-calculated tables so that these methods are much more efficient than directly solving the slowing-down equation. However, the derivation of integral table based methods introduces a couple of approximations, leading to limitations of these methods to treat resonance interference, spatially distributed self-shielding, and non-uniform temperature profile within the fuel rod.

To overcome these limitations, the new method incorporates a correction scheme. The conventional iteration of the embedded self-shielding method (ESSM) is still performed without subdivision of the fuel regions to capture the global inter-pin shielding effect. The resultant self-shielded cross sections are modified by correction factors incorporating the intra-pin effects due to radial variation of the shielded cross section, radial temperature distribution, and resonance interference. An efficient quasi-1D slowing-down equation is developed to calculate these correction factors. In essence, the assumption that underpins this new method is that the global Dancoff effect is treated satisfactorily with ESSM, while the effects of radial fuel regions and resonance interference are local phenomena that can be solved with the quasi-1D model. The new method yields substantially improved results for both radially dependent and energy-dependent reaction rates, which help to improve the within-pin physics for multi-region depletion and multiphysics calculations, as well as the overall eigenvalue estimation.

Chapter 1

Introduction

The main task in the field of nuclear reactor physics is to solve the Boltzmann neutron transport equation, which is an integro-differential equation with seven independent variables in respect to time, space, energy and angle. Analytic solution of the neutron transport equation can be found for very simple problems, but is practically infeasible for realistic problems in reactor core analysis. Numerical methods have been devised to solve the neutron transport equation, which are generally divided into two groups, deterministic methods and stochastic methods. Since the computational resources are limited with regard to the computational complexity of the equation, the efforts of deterministic methods are based on making approximations, physical and mathematical, to reduce the complexity of the high dimensional phase space and give accurate results within a reasonable computing time.

The independent variables of the neutron transport equation, namely, time t, neutron position r, energy E and direction Ω are numerically treated by either of the two approaches, discretization or modal expansion [1]. The time, neutron position and energy variables are often approximated to be discrete, while the discretization and expansion approaches of treating the angular variable yields discrete ordinates (Sn) and spherical harmonics (Pn) methods, respectively. To emphasize, since the neutron flux is very dependent on the cross section by which neutron interacts with the background medium, energy discretization of the transport equation demands extra care to resolve the complicated energy dependence of cross sections, which is one of the most challenging problems for reactor core analysis. Figure 1.1 contains an example of the energy dependence of cross sections for neutron interactions with U-238. In the resonance energy range, say, from roughly 1eV to 100keV, the cross sections are sharply varied according to the numerous resonance peaks, and thus yielding a fine structure of neutron flux distribution over the energy domain.

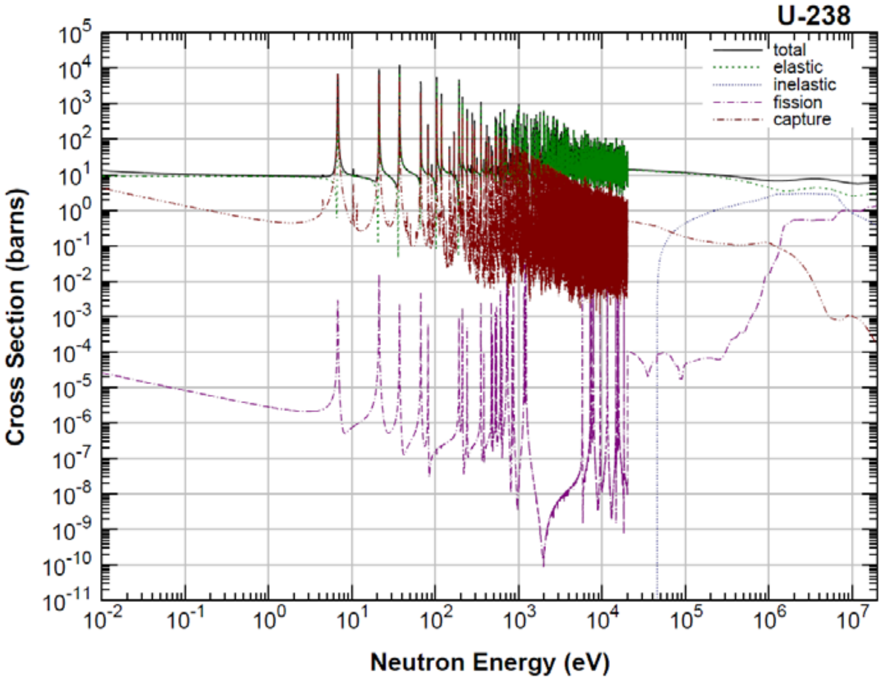

Figure 1.1 Continuous-energy cross sections of U-238 [2]

Histogram approximation is a straightforward approach for energy discretization. In order to resolve the resonance cross section, an ultra-fine energy mesh should be applied so that within each mesh, the cross section can be treated as a constant. Histogram approximation is computationally expensive due to the hundreds of thousands of energy meshes that are needed to resolve the complex energy dependence shown in Figure 1.1. In practice, one would like to solve the neutron transport equation by a small number of energy meshes, which leads us to multigroup theory. In the multigroup method, the continuous-energy transport equation is integrated over a set of pre-defined energy groups to achieve a multigroup form of the transport equation. The width of each energy group could be broad, covering one or more resonances of the typical reactor materials. To be consistent with the original continuous-energy equation, rather than arithmetically averaging the continuous-energy cross sections, the multigroup cross sections should be weighted by the neutron flux of the specific problem, which is not available until one rigorously solves the continuous-energy transport equation. Therefore, approximations are indispensable in evaluating the flux-weighted multigroup cross sections. Once the multigroup cross sections are complete, multigroup transport calculation can be performed to determine the neutron flux distribution. Clearly, the ability of generating multigroup cross sections to preserve the physics of continuous energy plays a crucial role for the accuracy of reactor core analysis. The focus of this work is to develop a method by which the multigroup cross sections can be generated more consistently with a continuous-energy solution in energy and a radially dependent mesh in the space domain.

1.1 Neutron Transport and Multigroup Theory

The steady-state neutron transport equation that describes the motion of neutron and its iteration with matter is defined as

$$\begin{aligned}\Omega \cdot \nabla \psi(r,\Omega,E) + \sum_{iso} N_{iso}\sigma_{t,iso}(r,E)\psi(r,\Omega,E) \\ = \int_0^\infty \int_{4\pi} \sum_{iso} N_{iso}\sigma_{s,iso}(r,\Omega'\cdot\Omega,E'\to E)\psi(r,\Omega',E')d\Omega' dE' \\ + \frac{\chi(r,E)}{4\pi k}\int_0^\infty \int_{4\pi} \sum_{iso} N_{iso}\nu\sigma_{f,iso}(r,E')\psi(r,\Omega',E')d\Omega' dE'\end{aligned} \tag{1.1}$$

In this equation, the neutron flux $\psi(r,\Omega,E)$ is allowed to vary with position r, direction Ω and energy E. $\sigma_{x,iso}$ is the microscopic cross section of reaction channel x (t for total, s for scattering and f for fission) for isotope iso. N_{iso} is the atomic number density of isotope iso. ν is the average number of neutrons generated per fission, and $\chi(E)$ is the fission spectrum distribution. k is the multiplication factor of the system. To obtain a multigroup form of the transport equation, Equation (1.1) is integrated over the range of energies corresponding to Group g. We define the multigroup flux and cross sections as,

$$
\begin{aligned}
&\psi_g(r,\Omega) = \int_{E_g}^{E_{g-1}} \psi(r,\Omega,E)dE \\
&\sigma_{t,iso,g}(r,\Omega) = \int_{E_g}^{E_{g-1}} \sigma_{t,iso}(r,E)\psi(r,\Omega,E)dE \Big/ \int_{E_g}^{E_{g-1}} \psi(r,\Omega,E)dE \\
&\sigma_{f,iso,g}(r,\Omega) = \int_{E_g}^{E_{g-1}} \sigma_{f,iso}(r,E)\psi(r,\Omega,E)dE \Big/ \int_{E_g}^{E_{g-1}} \psi(r,\Omega,E)dE \\
&\chi_g(r) = \int_{E_g}^{E_{g-1}} \chi(r,E)dE \\
&\sigma_{s,iso,g'\to g}(r,\Omega',\Omega) = \int_{E_g}^{E_{g-1}} \int_{E_{g'}}^{E_{g'-1}} \sigma_{s,iso}(r,\Omega'\cdot\Omega,E'\to E)\psi(r,\Omega',E')dE'dE \Big/ \int_{E_{g'}}^{E_{g'-1}} \psi(r,\Omega',E')dE'
\end{aligned}
\tag{1.2}
$$

Then the multigroup transport equation is given as

$$
\begin{aligned}
\Omega\cdot\nabla\psi_g(r,\Omega) &+ \sum_{iso} N_{iso}\sigma_{t,iso,g}(r)\psi_g(r,\Omega) \\
&= \sum_{g'=1}^{G}\int_{4\pi}\sum_{iso} N_{iso}\sigma_{s,iso,g'\to g}(r,\Omega'\cdot\Omega)\psi_{g'}(r,\Omega')d\Omega' \\
&\quad + \frac{\chi_g(r)}{4\pi k}\sum_{g'=1}^{G}\int_{4\pi}\sum_{iso} N_{iso}\nu\sigma_{f,iso,g'}(r)\psi_{g'}(r,\Omega')d\Omega'
\end{aligned}
\tag{1.3}
$$

The knowledge of the continuous-energy angular flux is needed in advance to determine the multigroup constants of Equation (1.2). For most reactor applications of interest, it is a reasonable approximation to separate the energy and angular variables

$$
\psi(r,\Omega,E) \approx \phi(r,E)\Psi(r,\Omega) \tag{1.4}
$$

By substituting Equation (1.4) into (1.2), the angular dependence of flux can be eliminated. The multigroup cross sections approximately preserve the true reaction rate and are called ‘effective cross section’. In addition, the flux weighted cross section integral (the numerators of multigroup cross section in Equation (1.2)) is called resonance integral (RI).

The methods of determining neutron flux for collapsing the effective cross section depend on the range of neutron energies of interest [3]. At the high energies above resonances, one might approximate the flux by the fission spectrum. In the thermal energy range, the neutron energy is comparable to the thermal motion of nuclei, and as well to the binding energy of the atoms in molecular or crystalline materials. These features complicate the determination of thermal cross sections. Fortunately, in the applications of thermal reactors where the neutron energy spectrum is sufficiently well thermalized, rather crude models of the neutron scattering process are sufficient for the generation of thermal group constants. It is the intermediate energy range where numerous resonances occur, where the neutron spectrum can be very problem-dependent, making it difficult to pre-determine the multigroup cross sections. In this energy range, resonance self-shielding is the primary reason for problem-dependent multigroup cross sections.

1.2 Phenomena of Resonance Self-shielding

The resonance self-shielding effect can be broken into two types, energy self-shielding and spatial self-shielding. Energy self-shielding is caused by the strong dependence of the neutron spectrum on the energy-dependent cross section, while spatial self-shielding is primarily due to the heterogeneous configuration of the reactor.

1.2.1 Energy Self-shielding

A neutron with an energy near a resonance is likely to be absorbed by the resonance isotope, thus creating a flux dip in the vicinity of the resonance. Energy self-shielding results in a reduction of the effective absorption per nucleus due to the depression of the energy-dependent flux near the resonance as compared to a flat flux. Figure 1.2 compares the spectrum of a typical PWR cell for a range of densities of fuel materials. When the fuel density decreases, the amount of flux depression versus energy becomes less severe. If these fluxes are used in Equation (1.2) to evaluate the multigroup cross section, the case with the largest fuel density should result in the smallest effective absorption per nucleus. In other words, although the total absorption rate in a resonance group is increased by adding more fuel material, the effective absorption per nucleus is reduced, thus being ‘shielded by the material itself’.

The material temperature also affects the energy self-shielding through Doppler-broadening of the microscopic resonance cross section. In Figure 1.3, as the temperature increases, the wings of resonance are broadened while its peak magnitude decreases. The resultant spectra closely follow the behavior of resonance in a reverse manner, leading to a reduction in the self-shielding and an increase in the effective microscopic absorption cross section, which is a key phenomenon that provides negative reactivity feedback against fuel temperature increase.

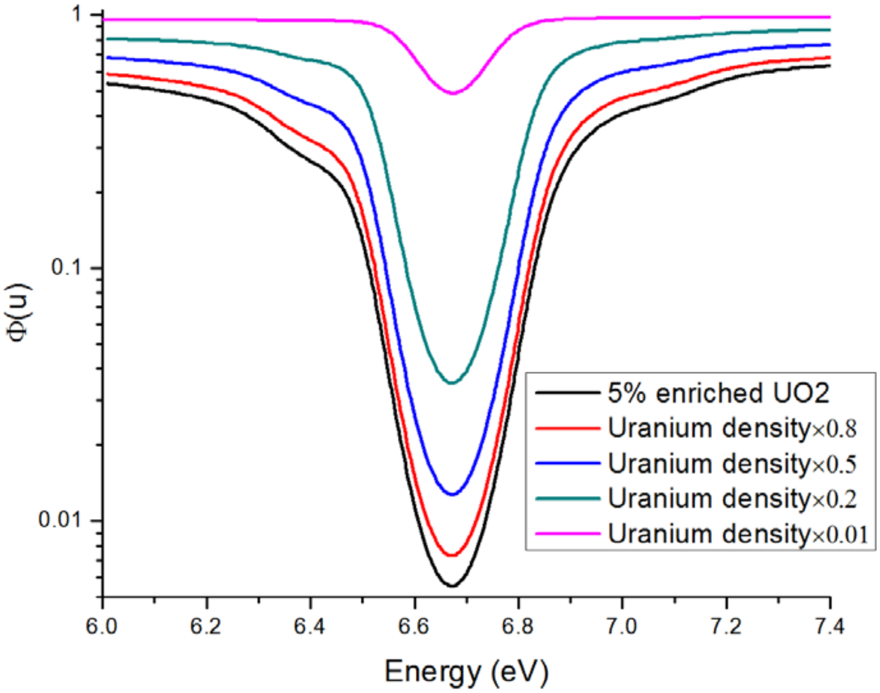

Figure 1.2 Neutron spectra versus uranium density at 6.67eV resonance of U-238

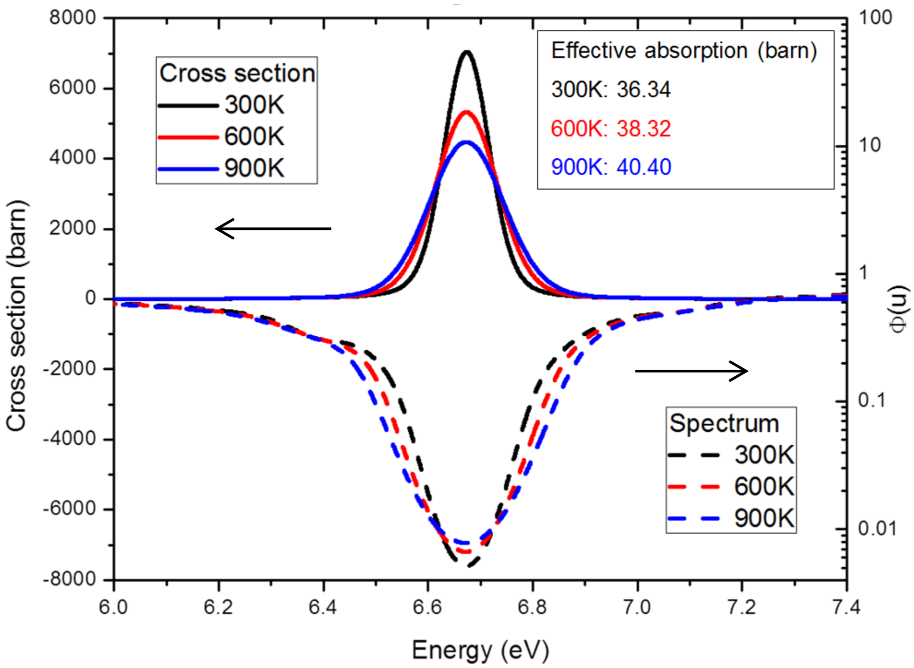

Figure 1.3 Neutron spectra versus fuel temperature at 6.67eV resonance of U-238

1.2.2 Spatial Self-shielding

The basic element of a light water reactor is a pin cell: a fuel rod is surrounded by moderator. Although the fission neutrons are born in the fuel, they are mostly slowed down by the moderator, while some of them are absorbed when they travel through the fuel. Near the energies of a resonance peak, neutrons coming from the moderator are more likely absorbed by the resonance nuclei near the fuel surface, so the fuel geometrically shields itself from neutron penetration, leading to a relatively lower neutron flux inside the fuel rod as compared to near the fuel surface. Figure 1.4 presents the neutron spectra of different fuel annuli of a typical PWR pin cell (six equal-volume annuli are divided), indicating that the effective absorption cross section differs greatly from one fuel ring to another.

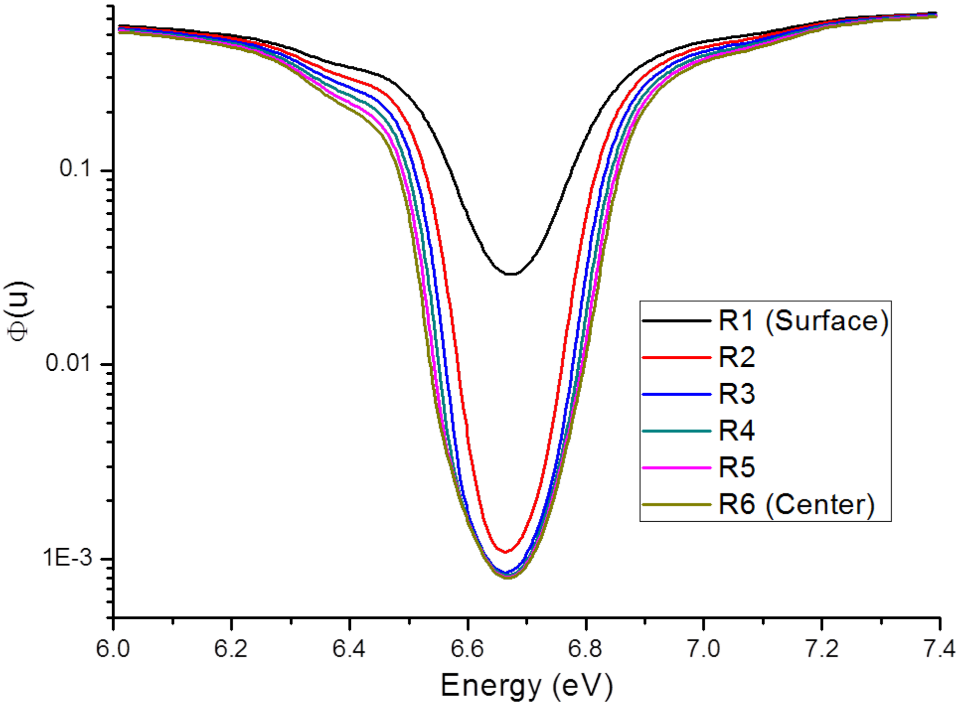

Figure 1.4 Neutron spectra versus fuel annuli at 6.67eV resonance of U-238

To summarize, because of the resonance self-shielding effect in energy and space, the neutron scalar flux in Equation (1.4) is very dependent on the problem (material, location, temperature, etc.). Therefore, the resonance calculation has to be performed for every specific case.

1.3 Resonance Calculation for Deterministic Methods

Even with the multigroup approximation, a direct transport calculation under realistic geometry, material composition and temperature profile of a reactor core configuration has only been possible since one or two decades ago. For the conventional reactor core analysis to save computing resources, a two-step methodology was adopted where the first step is generation of the homogenized few group cross sections over a subdomain (e.g., an assembly) with a transport method and the second step is a global nodal calculation with a diffusion method. Either direct transport or the two-step method begins with a multigroup cross section library containing resonance parameters. In a direct transport method, multigroup cross sections are usually prepared for all the material regions without homogenization, so the resonance calculation is performed for the explicit geometry, e.g., for each 2-D plane with detailed material region and geometrical mesh. The axial effect is usually neglected by assuming a reflective boundary condition (infinite length in z direction). In the two-step method, the first step is called lattice calculation, which determines the homogenized few group cross sections for each fuel assembly. The lattice calculation basically starts with the treatment of resonance self-shielding to produce the problem-specific multigroup effective cross sections. Those cross sections are then condensed into few groups and geometrically homogenized over the whole assembly. In addition, a leakage calculation is required to modify the infinite lattice results to include the effects of leakage for a finite reactor. In principal, the methodologies for performing the resonance calculation in the direct transport method and the two-step method are similar.

Two types of approaches for performing the resonance self-shielding calculation can be identified. The first is to obtain the direct solution of the ‘slowing-down equation’, an approximate form of the transport equation that is defined on the resonance energy range. Continuous energy or ultrafine-mesh cross sections are required, which restricts the slowing-down calculation to local geometries such as a pin cell or a single assembly. For example, RMET21 [4] and the early version of CENTRM [5] are restricted to 1-D cylindrical pin cell geometry that has been converted from the square pin cell using the Wigner-Seitz approximation. The MERIT [6] code analyzes a 2-D pin cell calculation using the Method of Characteristics (MOC), which removes the possible error arising from the Wigner-Seitz approximation. Recently, this 2-D pin cell capability has been included in the latest version of CENTRM [7]. To account for the inter-pin heterogeneity, a 2-D slowing-down code for an assembly configuration was first attempted in the GEMINEWTRN code [8]. The effective cross sections can be accurately generated by GEMINEWTRN with regard to the spatial heterogeneity, but the computing time becomes an issue when the assembly-size problem is solved by the direct slowing-down method. Currently, solving the slowing-down equation for a 2-D full core problem is still computationally prohibitive, so the influence of neighboring assemblies or reflector regions on the effective cross sections is not accounted for by the direct slowing-down method.

The second type of approaches for resonance self-shielding calculation utilizes pre-computed integral tables. Despite complexity of interactions in the resonance self-shielding, for every temperature of interest, the RI or effective cross section can be tabulated through a single parameter called the background cross section, which is a measure of dilution, the concentration of a resonance isotope relative to the background isotopes. The Bondarenko method [9] is a conventional approach that correlates RI or effective cross section with background cross section. Based on the equivalence theory [10], the heterogeneous self-shielding effect can be modeled by including an equivalence cross section into the background cross section, and variations on the Bondarenko method have been developed to treat heterogeneous geometry [10,11]. In the past two to three decades, a powerful alternative to the Bondarenko method, the subgroup method [12,13] has been developed and widely implemented in modern lattice codes. In the subgroup approach, the detailed cross section behavior of each coarse energy group is replaced by its probability density representation that preserves certain integrals. There are two methods for determining the subgroup probability tables [14]. The first is the physical probability table, in which the RI tables are converted into a set of subgroup levels and weights by preserving the RI or effective cross section over different background cross sections. The second method utilizes a mathematical probability table. Instead of preserving the RI, it preserves the cross section moments by processing the point-wise cross section data. Recently another promising RI table based method, the iterative self-shielding method [15,16] was developed by Korea Atomic Energy Research Institute (KAERI) and Oak Ridge National Laboratory (ORNL). ORNL entitled it the Embedded Self-Shielding Method (ESSM) because compared to the conventional Bondarenko method in which the lattice effect (Dancoff correction) is usually evaluated outside the transport calculation, ESSM provides tighter coupling between neutron transport and self-shielding calculations, assuring that the heterogeneous self-shielding effects are consistent with the multigroup transport calculations of the system. Since the application of integral table based methods only involve multigroup calculations, these methods are much more efficient than directly solving the CE slowing-down equation for the specific configuration. Unfortunately, approximations made on the way of deriving the integral tables result in a few issues affecting the accuracy of the resonance calculation, especially for the generation of multigroup cross sections of the direct transport calculation. These issues will be addressed in the current work.

1.4 Thesis Outline

When the thesis work started three and a half years ago, the idea of ESSM was a white paper from ORNL. The early version of ESSM implemented by this work revealed a few issues which turned out to be difficult to resolve within the framework of the original ESSM methodology. In the meantime, it was found that some of these issues are in common for the integral table based methods, say, resonance interference, which was addressed first. Therefore, a correction-based method [17,18] was devised to resolve the resonance interference effect explicitly by utilizing ESSM and a 0-D slowing-down calculation. Unfortunately, this approach was restricted to a single-mesh fuel region. Motivated by the success of the correction method using the slowing-down solution, a comprehensive method is developed in this work to account for all three issues i.e., resonance interference, spatial self-shielding, and non-uniform temperature profile, by utilizing a quasi-1D slowing-down calculation. This work is presented as follows:

Chapter 2 discusses the first type of resonance self-shielding methods using a direct slowing-down solution. Two energy mesh discretization schemes are described, as well as the solution procedure using these mesh schemes. This discussion is necessary in order to understand the slowing-down methodology developed in the new method presented in Chapter 4.

Chapter 3 discusses the second type of resonance self-shielding methods that rely on pre-computed integral tables. Three integral table based methods, the Bondarenko-type method, the ESSM and the subgroup method are described in this chapter to illustrate how these methods work and how the approximations made during the derivations of these methods lead to their being unable to account for resonance interference, distributed self-shielding effect or a non-uniform fuel temperature profile. The previous efforts for overcoming these limitations are also described, with a conclusion that these methods are either unable to resolve these issues properly, or can only resolve a single issue but not all three.

Chapter 4 presents the new resonance self-shielding method which is able to overcome the three limitations simultaneously. The new method adopts ESSM for a baseline calculation to account for the global Dancoff effect. Starting from the collision probability form of the integral transport equation, an effective quasi-1D slowing-down equation is developed to account for the intra-pin effects that correspond to the three limitations. The global ESSM calculation and the local 1D slowing-down calculation are connected by modifying the equivalence cross section rather than using explicit boundary conditions.

Chapter 5 verifies the new resonance self-shielding method through a set of benchmark problems that are representative of real LWR configurations. The subgroup method and conventional ESSM are performed for comparison. An extension of the methodology to treat azimuthal dependent self-shielding is also investigated.

Chapter 6 presents the summary, conclusions and recommendations for future work.

Chapter 2

Direct Method: Solving the Slowing-down Equation

Generation of multigroup cross sections requires a neutron spectrum with a fine energy resolution. Although it is not possible to obtain the exact flux solution before the transport equation is rigorously solved, an ‘essentially exact’ solution can be obtained by solving a simplified form of the transport equation in the resonance energy range, i.e., the neutron slowing-down equation. The assumptions needed to obtain the slowing-down equation from the transport equation are discussed in this chapter, followed by a description of a few methods for the energy discretization.

2.1 Assumptions for the Neutron Slowing-down Equation

As mentioned previously, it is customary to divide the energy range of interest into three regions, each of which features typical neutron reactions, as shown in Figure 2.1. Of interest to us is the intermediate energy region, where three major assumptions regarding the source terms are applied to obtain the slowing-down equation:

1. Direct fission source is neglected;
2. Asymptotic scattering kernel is assumed so that upscattering is neglected;
3. The scattering source is treated by only considering isotropic s-wave elastic reactions.

For the fission spectrum of U-235, which is the primary isotope sustaining fission chain reaction for light water reactors, more than 99% of the direct fission neutrons are born in the fast energy region (>10^5eV). The neutron source in the slowing-down region is primarily provided by the scattered neutrons from higher energies, so (1) is a good approximation. Assumption (2) is generally used in conventional slowing-down codes, but recent works [19,20] have shown that the explicit treatment of resonance upscattering for heavy nuclides in the epithermal energy range can increase the LWR Doppler coefficients by 10% relative to the asymptotic scattering kernel. In the current work, the asymptotic scattering kernel is still used for the slowing-down calculation as resonance upscattering is well outside the scope of this work. Assumption (3) requires a bit more discussion. Anisotropic effects of neutron transport theory usually fall into two classes: those related to the scattering cross section and those related to the anisotropy of neutron streaming due to the inhomogeneous reactor configurations. Thus if either the cross section or the flux are approximately isotropic, this would be sufficient to make Assumption (3) valid. A physical explanation supporting Assumption (3) was presented in Ref. [21] and is repeated here. As the energy ranges away from resonances, the neutron flux is almost isotropic for all material regions (fuel, cladding, moderator, etc.). However, near the resonance peaks where the absorption is large, the neutron flux is anisotropic, tending toward the fuel region from the moderator region. At such energies, the angular distribution of the scattering cross section in the lab system is nearly isotropic for heavy nuclides such as U-238, O-16 or Zr, and anisotropic for H-1. Therefore, in the fuel and cladding regions, the scattering source is isotropic in spite of the anisotropic flux. In the moderator, the neutron flux and scattering cross section of H-1 are both anisotropic near the resonance peaks. However, the neutron could lose all of its energy through a single collision with H-1, indicating that neutrons slowing down to an energy value near the resonance are coming from a far higher energy range where an isotropic flux is a reasonable assumption. Thus, an isotropic scattering source is also a good approximation in the moderator. Some numerical results are included in Ref. [21,22] showing that the effect of including anisotropic scattering in the slowing-down calculation is minimal.

Applying the three assumptions into Equation (1.1), the slowing-down equation is given as

$$\begin{aligned}\Omega\cdot\nabla\psi(r,\Omega,u)&+\sum_{iso}\Sigma_{t,iso}(r,u)\psi(r,\Omega,u)\\&=\frac{1}{4\pi}\sum_{iso}\int_{u-\varepsilon_{iso}}^{u}\Sigma_{s,iso}(r,u')\phi(r,u')\frac{e^{u'-u}}{1-\alpha_{iso}}du'\end{aligned}\tag{2.1}$$

where ϕ is the scalar flux per unit lethargy, $\alpha_{iso} = \left(\frac{A_{iso}-1}{A_{iso}+1}\right)^2$ and $\varepsilon_{iso} = \ln\left(\frac{1}{\alpha_{iso}}\right)$ are the maximum fraction of energy loss and maximum lethargy gain per neutron scattered off isotope iso, respectively. The energy E has been transformed to lethargy u, as is conventionally done for the slowing-down equation. For each lethargy point u, if the scattering source term is determined, the remaining work is to solve a fixed source transport problem by a discretization method such as MOC or Sn. Since very fine energy meshes have to be applied to model the resonances, the energy mesh scheme plays an important role in efficiently solving the slowing-down equation.

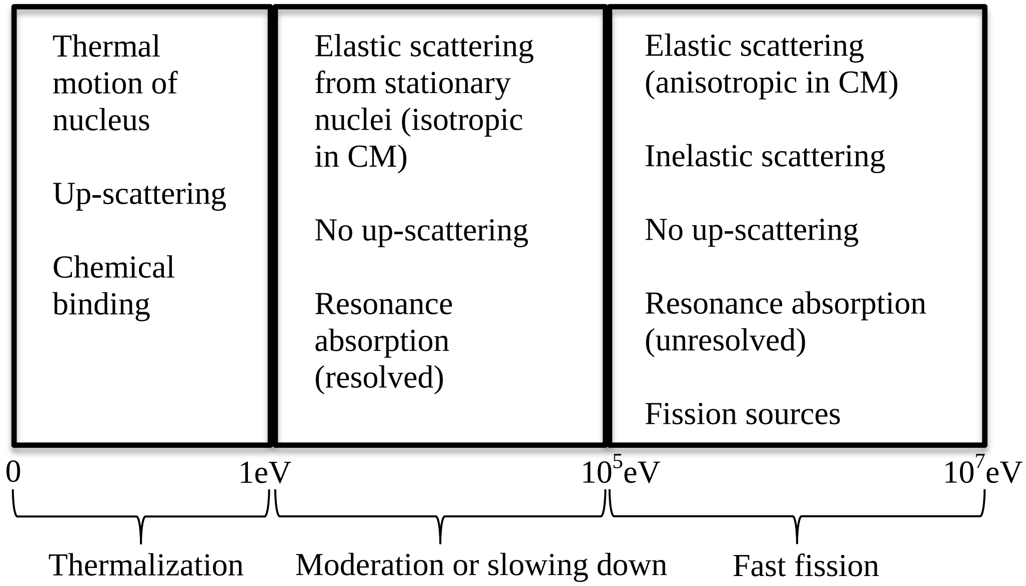

Figure 2.1 Typical neutron reactions of different energy ranges (adapted from [3])

2.2 Energy Discretization Schemes

One approach is to discretize the energy range of interest into a large number of equal-lethargy groups, where the group width is pre-determined and not dependent on the problem. A fundamental approximation of this ultrafine group scheme is that the fluxes and cross sections are constants within each group, so that the group width should be very narrow. Another approach adopts a flexible mesh scheme that assigns more meshes to the energy range where greater fluctuation of the total cross sections occurs, so the mesh size is non-uniform and problem-dependent. These two mesh schemes are discussed in the following subsections.

2.2.1 Equal Lethargy Mesh

The complicated part of solving the slowing-down equation is the evaluation of the scattering source term. The contribution to the scattering source from each isotope iso is given as

$$Q_{iso}(r,u)=\int_{u-\varepsilon_{iso}}^{u}\Sigma_{s,iso}(r,u')\phi(r,u')\frac{e^{u'-u}}{1-\alpha_{iso}}du' \tag{2.2}$$

To evaluate the integral, the constant group width Δu_g should be narrow compared with the maximum lethargy gain per scattering of the heaviest isotope. Integrating Equation (2.2) over lethargy boundaries of group g yields the scattering source for group g

$$Q_{iso,g}(r)=\int_{u_g}^{u_g+\Delta u_g}\int_{u-\varepsilon_{iso}}^{u}\frac{e^{u'-u}}{1-\alpha_{iso}}\Sigma_{s,iso}(r,u')\phi(r,u')du'du \tag{2.3}$$

To proceed, the inner (incident lethargy) integration range is split into two parts, i.e., $[u_g,u]$ and $[u-\varepsilon_{iso},u_g]$

$$\begin{aligned}Q_{iso,g}(r)&=Q_{iso,g\to g}(r)+Q_{iso,other\to g}(r)\\&=\int_{u_g}^{u_g+\Delta u_g}\int_{u_g}^{u}\frac{e^{u'-u}}{1-\alpha_{iso}}\Sigma_{s,iso}(r,u')\phi(r,u')du'du\\&\quad+\int_{u_g}^{u_g+\Delta u_g}\int_{u-\varepsilon_{iso}}^{u_g}\frac{e^{u'-u}}{1-\alpha_{iso}}\Sigma_{s,iso}(r,u')\phi(r,u')du'du\end{aligned} \tag{2.4}$$

The within-group scattering term (first term) can be evaluated by taking the constant $\Sigma_{s,iso}(r,u')\phi(r,u')=\Sigma_{s,iso,g}(r)\phi_g(r)/\Delta u_g$ out of the integral, thus

$$Q_{iso,g\to g}(r)=\frac{\Sigma_{s,iso,g}(r)\phi_g(r)}{\Delta u_g(1-\alpha_{iso})}\left(\Delta u_g+e^{-\Delta u_g}-1\right)=P_{0,iso}\Sigma_{s,iso,g}(r)\phi_g(r) \tag{2.5}$$

where $P_{0,iso}=\left(\Delta u_g+e^{-\Delta u_g}-1\right)\big/\left[\Delta u_g(1-\alpha_{iso})\right]$ is defined as the probability that a neutron stays in the group after a collision with isotope iso. To evaluate the second term in

Equation (2.4), an approximation is made on the limits of the inner integral, as illustrated in Figure 2.2.

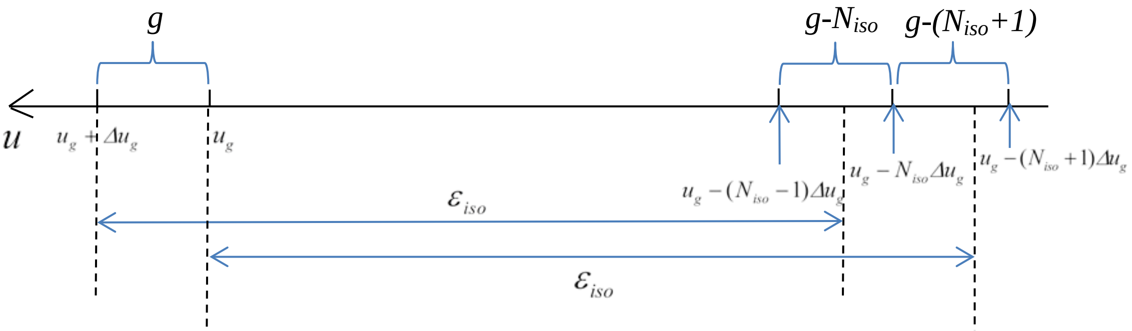

Figure 2.2 Integration intervals for equal-lethargy group scheme

We define N_{iso} as the integer part of $\varepsilon_{iso} / \Delta u_g$. Since u varies from u_g to $u_g + \Delta u_g$, the corresponding limits of inner integral are within two extreme conditions, i.e., $\int_{u_g-\varepsilon_{iso}}^{u_g} du'$ and $\int_{u_g+\Delta u_g-\varepsilon_{iso}}^{u_g} du'$. An intermediate lower limit $u_g - N_{iso}\Delta u_g$ is chosen such that the overestimated source from group *g-N_{iso}* to some large lethargy values u in $(u_g, u_g + \Delta u_g)$ is partially compensated by underestimating the source from group g-$(N_{iso}+1)$ to some small lethargy values u in $(u_g, u_g + \Delta u_g)$. Then the second term of Equation (2.4) becomes

$$\begin{aligned} Q_{iso,other->g}(r) &= \int_{u_g}^{u_g+\Delta u_g} \int_{u_g-N_{iso}\Delta u_g}^{u_g} \frac{e^{u'-u}}{1-\alpha_{iso}} \Sigma_{s,iso}(r,u')\phi(r,u')du'du \\ &= \int_{u_g}^{u_g+\Delta u_g} du \sum_{j=1}^{N_{iso}} \int_{u_g-j\Delta u_g}^{u_g-(j-1)\Delta u_g} \frac{e^{u'-u}}{1-\alpha_{iso}} \Sigma_{s,iso}(r,u')\phi(r,u')du' \end{aligned} \tag{2.6}$$

The inner integral is summed over groups from g-1 to g-N_{iso}, and within each group the constant flux and scattering cross section can be taken out to obtain

$$Q_{iso,other->g}(r) = \sum_{j=1}^{N_{iso}} \Sigma_{s,iso,g-j}(r) \frac{\phi_{g-j}(r)}{\Delta u_g} \int_{u_g}^{u_g+\Delta u_g} \int_{u_g-j\Delta u_g}^{u_g-(j-1)\Delta u_g} \frac{e^{u'-u}}{1-\alpha_{iso}} du'du \tag{2.7}$$

Evaluating the double integrals gives

$$\begin{aligned} Q_{iso,other->g}(r) &= \sum_{j=1}^{N_i} \varSigma_{s,iso,g-j}(r) \frac{\phi_{g-j}(r)}{(1-\alpha_{iso})\varDelta u_g} \left(e^{-(j-1)\varDelta u_g} \left(1-e^{-\varDelta u_g}\right)^2 \right) \\ &= \sum_{j=1}^{N_i} \varSigma_{s,iso,g-j}(r)\phi_{g-j}(r) P_{j,iso} \end{aligned} \tag{2.8}$$

where $P_{j,iso} = \dfrac{\left(e^{-(j-1)\varDelta u_g} \left(1-e^{-\varDelta u_g}\right)^2 \right)}{(1-\alpha_{iso})\varDelta u_g}$ is the probability that a neutron traverses '*j*' energy groups after a collision with the isotope *iso*. Direct evaluation of the summation in Equation (2.8) repeatedly for every group would be time-consuming, since the number of groups that a neutron can traverses easily reach up to several thousands. Thus a cumulative approach is applied to make use of the source of the previous group [23],

$$\begin{aligned} Q_{iso,other->g} &= \varSigma_{s,iso,g-1}\phi_{g-1}P_{1,iso} + \sum_{j=2}^{N_{iso}} \varSigma_{s,iso,g-j}\phi_{g-j}P_{j,iso} \\ &\quad + \varSigma_{s,iso,g-N_{iso}-1}\phi_{g-N_{iso}-1}P_{N_{iso}+1,iso} - \varSigma_{s,iso,g-N_{iso}-1}\phi_{g-N_{iso}-1}P_{N_{iso}+1,iso} \\ &= \varSigma_{s,iso,g-1}\phi_{g-1}P_{1,iso} + e^{-\varDelta u_g}\left(\sum_{j=2}^{N_{iso}} \varSigma_{s,iso,g-j}\phi_{g-j}P_{j-1,iso} + \varSigma_{s,iso,g-N_{iso}-1}\phi_{g-N_{iso}-1}P_{N_{iso},iso} \right) \\ &\quad - \varSigma_{s,iso,g-N_{iso}-1}\phi_{g-N_{iso}-1}P_{N_{iso}+1,iso} \\ &= \varSigma_{s,iso,g-1}\phi_{g-1}P_{1,iso} + e^{-\varDelta u_g} Q_{iso,other->g-1} - \varSigma_{s,iso,g-N_{iso}-1}\phi_{g-N_{iso}-1}P_{N_{iso}+1,iso} \end{aligned} \tag{2.9}$$

Equations (2.5) and (2.9) complete the determination of the scattering source due to isotope *iso*. The total scattering source are summed up over all isotopes, and the slowing-down equation turns out to be

$$\begin{aligned} &\Omega \cdot \nabla \psi_g(r,\Omega) + \sum_{iso} \Sigma_{t,iso,g}(r)\psi_g(r,\Omega) \\ &\qquad = \frac{1}{4\pi} \sum_{iso} \left[Q_{iso,g\to g}(r) + Q_{iso,other\to g}(r) \right] \end{aligned} \tag{2.10}$$

Starting from a threshold energy group above all the resonances, one is able to solve the slowing-down equation as an increasing order of groups (descending order of energy). As the slowing-down spectra are used for cross section weighting, the amplitude of flux is not important so one can assume a 1/E flux shape above the threshold energy to initialize the calculation. Since the energy mesh does not depend on the composition of the material, a fresh fuel pin or a depleted fuel with 100+ isotopes may use the same energy mesh which is always predetermined in a specific resonance energy range. However, the equal-lethargy mesh is time-consuming, especially for heterogeneous slowing-down calculations, because the fixed source problem has to be solved for hundreds of thousands of groups.

2.2.2 Problem Dependent Energy Mesh

Compared to the fixed energy points of an equal-lethargy mesh, the problem-dependent mesh has a more flexible mesh size which is primarily dependent on the energy dependence of the material macroscopic total cross section. To obtain an optimized problem-dependent mesh, the first step is to construct a union energy mesh from the original energy meshes for the isotopes for each material. The macroscopic total cross sections are computed on the union mesh and used to thin the union mesh in such a manner that the macroscopic total cross section of the material can be linearly interpolated according to a specific tolerance. After unionizing and thinning, the energy meshes of all materials are combined together to form the final mesh for the slowing-down calculation. This procedure is used in CENTRM [5]. The determination of the scattering source is discussed next.

Starting from Equation (2.1), the exponential quantity is written in terms of energy to avoid the exponential calculation

$$\begin{aligned}\Omega\cdot\nabla\psi(r,\Omega,u)+\sum_{iso}\Sigma_{t,iso}(r,u)\psi(r,\Omega,u)\\ =\frac{1}{4\pi}\sum_{iso}\int_{u-\varepsilon_{iso}}^{u}\frac{E\Sigma_{s,iso}(r,u')}{E'(1-\alpha_{iso})}\phi(r,u')du'\end{aligned} \tag{2.11}$$

Equation (2.11) is satisfied at each energy (lethargy) point on the problem-dependent mesh, thus

$$\begin{aligned}\Omega\cdot\nabla\psi_n(r,\Omega)+\sum_{iso}\Sigma_{t,iso}(r,u_n)\psi_n(r,\Omega)\\ =\frac{1}{4\pi}\sum_{iso}\int_{u_n-\varepsilon_{iso}}^{u_n}\frac{E_n\Sigma_{s,iso}(r,u')}{E'(1-\alpha_{iso})}\phi(r,u')du'\end{aligned} \tag{2.12}$$

Define *m* as the number of lethargy points that a neutron scattering from nuclide *iso* will traverse from lethargy $u_n-\varepsilon_{iso}$ to u_n (u_n not included), so that the integral in Equation (2.12) can be split into *m* sub-integrals plus an extra term integrated from $u_n-\varepsilon_{iso}$ to u_{n-m}

$$\begin{aligned}&\sum_{iso}\int_{u_n-\varepsilon_{iso}}^{u_n}\frac{E_n\Sigma_{s,iso}(r,u')}{E'(1-\alpha_{iso})}\phi(r,u')du'\\&=\sum_{iso}\left[\sum_{j=1}^{m}\int_{u_{n-j}}^{u_{n-j+1}}\frac{E_n\Sigma_{s,iso}(r,u')}{E'(1-\alpha_{iso})}\phi(r,u')du'+\int_{u_n-\varepsilon_{iso}}^{u_{n-m}}\frac{E_n\Sigma_{s,iso}(r,u')}{E'(1-\alpha_{iso})}\phi(r,u')du'\right]\end{aligned}\tag{2.13}$$

Except the extra term, these integrals are evaluated with trapezoidal rule,

$$\begin{aligned}&\sum_{iso}\left[\sum_{j=1}^{m}\int_{u_{n-j}}^{u_{n-j+1}}\frac{E_n\Sigma_{s,iso}(r,u')}{E'(1-\alpha_{iso})}\phi(r,u')du'+\int_{u_n-\varepsilon_{iso}}^{u_{n-m}}\frac{E_n\Sigma_{s,iso}(r,u')}{E'(1-\alpha_{iso})}\phi(r,u')du'\right]\\&=\sum_{iso}E_n\left[\frac{1}{2(1-\alpha_{iso})}\sum_{j=1}^{m}\Delta u_{n-j}\left(\frac{\Sigma_{s,iso}(r,u_{n-j+1})\phi_{n-j+1}(r)}{E_{n-j+1}}+\frac{\Sigma_{s,iso}(r,u_{n-j})\phi_{n-j}(r)}{E_{n-j}}\right)+\Delta S_{iso,n,m}(r)\right]\\&=\Sigma_{s,nn}(r)\phi_n(r)+\Sigma_{s,n'n}(r)\phi_{n-1}(r)\\&\quad+\sum_{iso}E_n\left[\frac{1}{2(1-\alpha_{iso})}\sum_{j=2}^{m}\Delta u_{n-j}\left(\frac{\Sigma_{s,iso}(r,u_{n-j+1})\phi_{n-j+1}(r)}{E_{n-j+1}}+\frac{\Sigma_{s,iso}(r,u_{n-j})\phi_{n-j}(r)}{E_{n-j}}\right)+\Delta S_{iso,n,m}(r)\right]\end{aligned}\tag{2.14}$$

where $\Delta u_{n-j}=u_{n-j+1}-u_{n-j}$

$$\Sigma_{s,nn}(r)=\sum_{iso}\frac{1}{2(1-\alpha_{iso})}\Delta u_{n-1}\Sigma_{s,iso}(r,u_n)$$

$$\Sigma_{s,n'n}(r)=\sum_{iso}\frac{E_n}{2(1-\alpha_{iso})E_{n-1}}\Delta u_{n-1}\Sigma_{s,iso}(r,u_{n-1})$$

$$\Delta S_{iso,n,m}(r)=\int_{u_n-\varepsilon_{iso}}^{u_{n-m}}\frac{\Sigma_{s,iso}(r,u')}{E'(1-\alpha_{iso})}\phi(r,u')du'$$

Even for heavy nuclides such as uranium and plutonium, the number *m* can be a few hundred. To avoid the time-consuming summation over *j* repeatedly for every energy point *n*, a cumulative term for each isotope *iso* is defined to facilitate the summation [5]

$$C_{iso,n}(r)=\frac{1}{2(1-\alpha_{iso})}\sum_{j=1}^{n-1}\Delta u_j\left(\frac{\Sigma_{s,iso}(r,u_{j+1})\phi_{j+1}}{E_{j+1}}+\frac{\Sigma_{s,iso}(r,u_j)\phi_j}{E_j}\right)\tag{2.15}$$

Thus, the summation term over *j* on the right-hand side of Equation (2.14) can be replaced by subtraction of two cumulative terms:

$$\begin{aligned}&\frac{1}{2(1-\alpha_{iso})}\sum_{j=2}^{m}\Delta u_{n-j}\left(\frac{\Sigma_{s,iso}(r,u_{n-j+1})\phi_{n-j+1}(r)}{E_{n-j+1}}+\frac{\Sigma_{s,iso}(r,u_{n-j})\phi_{n-j}(r)}{E_{n-j}}\right)\\&=C_{iso,n-1}(r)-C_{iso,n-m}(r)\end{aligned} \tag{2.16}$$

The extra term $\Delta S_{iso,n,m}(r)$ can be interpolated from $C_{iso,n-m}(r)-C_{iso,n-m-1}(r)$ by the lethargy difference. To sum up, three independent terms need to be evaluated for each lethargy point *n*, i.e., $\Sigma_{s,nn}$, $\Sigma_{s,n'n}$ and $\frac{1}{2(1-\alpha_{iso})}\Delta u_{n-1}\left(\frac{\Sigma_{s,iso,n}\phi_n}{E_n}+\frac{\Sigma_{s,iso,n-1}\phi_{n-1}}{E_{n-1}}\right)$. Note the third value is done for each isotope independently and is accumulated into $C_{iso,n}(r)$.

Similar to the equal-lethargy mesh scheme, one is able to solve the slowing-down equation as a descending order of energy from a threshold. Once the pointwise neutron spectrum is obtained, integration for multigroup effective cross sections for the problem-dependent mesh scheme needs extra consideration. As the mesh thinning is based on a specified tolerance for linear interpolation of the macroscopic total cross section for the whole material, there will be some cross section variations with energy for the original cross section, which is missing in the thinned energy mesh for the slowing-down calculation. To retrieve the cross section dependence of each isotope, the original mesh of the isotope and the thinned slowing-down mesh are unionized as the final mesh for the integration of effective cross section. The flux interpolation from the slowing-down mesh to the final mesh is performed by linearly interpolating the total reaction rate ($\Sigma_t\phi_t$) and total cross section Σ_t respectively, then dividing $\Sigma_t\phi_t$ by Σ_t. The reason of doing so is that the energy dependence of reaction rates is weaker than the energy dependence of spectrum, yielding smaller interpolation errors.

Chapter 3

Integral Table Based Methods

The neutron spectrum for collapsing effective cross sections can be accurately predicted by solving the slowing-down equation, but its prohibitive computing needs restrict its application to pin cell calculations. One would like to model the energy and spatial self-shielding effects with some simple parameters, by which the effective cross section of a specific problem can be obtained through table interpolation rather than a rigorous slowing-down calculation. From the view point of reactor physics, factors influencing the resonance self-shielding can be summarized as follows:

(1) Fuel composition (fuel type, enrichment, poison, burnup, etc.)

(2) Relative ratio of fuel to coolant (size of fuel rod, fuel and coolant densities)

(3) Arrangements of fuel pins (zoned fuel, water gap/hole, control rod, etc.)

(4) Subdivision of the fuel region (distributed self-shielding effect)

(5) Temperature

There have been a number of efforts to define and extract simple parameters to create a table of effective cross section that will account for these factors. To explain this approach, the Bondarenko method is chosen at the first place to understand the resonance self-shielding model in a homogeneous material as well as its generalization to the heterogeneous case by equivalence theory. The embedded self-shielding method and subgroup method are discussed afterward, with their limitations discussed in the last section of this chapter.

3.1 Bondarenko Method and Equivalence Theory

It would be impractical to generate the effective cross section table directly through the above physical factors. For a conventional lattice calculation, it is well-known that the self-shielding effect can be approximately modeled by two parameters, the background cross section and temperature. The methods based on using background cross sections are often called Bondarenko-type methods. The Bondarenko method is derived for homogeneous material first, and then generalized to consider heterogeneous geometry by introducing equivalence theory and the Dancoff factor.

3.1.1 Homogeneous Material

For a homogeneous material, only Factors (1) and (5) are involved in the self-shielding calculation. Even with this simplification, the fuel composition could be so complicated that one could not determine an effective cross section table by explicitly considering the weight percentages of isotopes. To obtain the weighting spectrum, Bondarenko originated an effective idea that unionizes all the isotopes other than the one in question as a single parameter σ_b [9], the 'background' cross section, which leads to the following expression for the weighting spectrum

$$\phi(u) \propto \frac{1}{\sigma_{t,res}(u) + \sigma_b} \tag{3.1}$$

In this equation, $\sigma_{t,res}(u)$ is the energy dependent microscopic total cross section of the resonance isotope in question. $\sigma_b = \sum_{iso \neq res} N_{iso}\sigma_{t,iso} \Big/ N_{res}$ is the summation of the total cross sections of all other isotopes divided by the number density of the resonance isotope. The flux is assumed to be inversely proportional to the total cross section of the material and the resonances of different isotopes are assumed to be separated from each other, so that the total cross section of other isotopes are approximated to be energy independent near the resonance of the isotope in question. Consider that the flux is used to collapse effective cross section. When σ_b dominates the denominator (for the large $\sigma_{t,res}(u)$ in the vicinity of a resonance, this usually happens when $N_{res} \ll \sum_{iso \neq res} N_{iso}$), the flux is prone to be flat. The resonance isotope is infinitely diluted and its effective cross section is unshielded, reaching the largest value at the energy group of the resonance. On the other hand, if the resonance isotope is dominant, i.e., $\sigma_b \ll \sigma_{t,res}(u)$, the resonance isotope is fully shielded by itself, leading to the smallest effective cross section. Therefore, the effective cross section can be tabulated through a range of background cross sections.

Alternatively, some cross section libraries tabulate RI instead of effective cross section

$$\overline{RI_{g,x,res}} = \frac{1}{\Delta u_g}\int_{u_{g-1}}^{u_g} \sigma_{x,res}(u)\phi(u)du \tag{3.2}$$

where x is the reaction channel. Substituting $\phi(u)$ in Equation (3.2) by Equation (3.1) gives

$$\overline{RI_{g,x,res}} = \frac{1}{\Delta u_g}\int_{u_{g-1}}^{u_g} \sigma_{x,res}(u)\frac{C}{\sigma_{t,res}(u)+\sigma_b}du \tag{3.3}$$

where C is an arbitrary constant that will cancel out when collapsing the effective cross section. To facilitate a simple correlation between RI and effective cross section, C is set to σ_b, then

$$\overline{RI_{g,x,res}} = \frac{1}{\Delta u_g}\int_{u_{g-1}}^{u_g} \sigma_{x,res}(u)\frac{\sigma_b}{\sigma_{t,res}(u)+\sigma_b}du \tag{3.4}$$

Using the same form to compute the group flux per lethargy

$$\begin{aligned}\overline{\phi_g} &= \frac{1}{\Delta u_g}\int_{u_{g-1}}^{u_g}\phi(u)du = \frac{1}{\Delta u_g}\int_{u_{g-1}}^{u_g}\frac{\sigma_b}{\sigma_{t,res}(u)+\sigma_b}du \\ &= 1-\frac{1}{\sigma_b\Delta u_g}\int_{u_{g-1}}^{u_g}\frac{\sigma_{t,res}(u)\sigma_b}{\sigma_{t,res}(u)+\sigma_b}du = 1-\frac{\overline{RI_{g,t,res}}}{\sigma_b}\end{aligned} \tag{3.5}$$

So the effective cross section is given as

$$\sigma_{g,x,res} = \frac{\overline{RI_{g,x,res}}}{\overline{\phi_g}} = \frac{\overline{RI_{g,x,res}}}{1-\overline{RI_{g,t,res}}\big/\sigma_b} \tag{3.6}$$

Using Equation (3.6), RI and effective cross section can be converted back and forth, so the tabulation of RI or effective cross section is equivalent. In addition to the background cross section, the table should be generated through a few temperatures of interest as well.

Similar flux forms to Equation (3.1) can be derived from the slowing-down equation by introducing resonance approximations. The slowing-down equation for a homogeneous medium is given as

$$\sum_{iso}\Sigma_{t,iso}(u)\phi(u)=\sum_{iso}\int_{u-\varepsilon_{iso}}^{u}\Sigma_{s,iso}(u')\phi(u')\frac{e^{u'-u}}{1-\alpha_{iso}}du' \tag{3.7}$$

One way to approximate the scattering source is to consider the resonance width narrow with respect to the energy loss of a neutron scattered off a nucleus, indicating that the neutrons appearing near the resonance peak come from far outside the peak and the scattering source originating inside the resonance is negligible. With this Narrow Resonance (NR) approximation, $\phi(u')$ in the scattering source term is assumed to be constant (normalized to unity above resonance) and the scattering cross section is approximated to be potential scattering $\Sigma_{p,iso}$ above resonance. Therefore, Equation (3.7) simplifies to

$$\phi(u)=\frac{\sum_{iso}\Sigma_{p,iso}}{\sum_{iso}\Sigma_{t,iso}(u)}=\frac{\Sigma_{p,res}+\sum_{iso\neq res}\Sigma_{p,iso}}{\Sigma_{t,res}(u)+\sum_{iso\neq res}\Sigma_{p,iso}} \tag{3.8}$$

On the right hand side of this equation, the total cross sections of the other isotopes are treated as potential scattering only, indicating that the resonance interference is neglected in this equation. By defining the background cross section $\sigma_b=\frac{\sum_{iso\neq res}\Sigma_{p,iso}}{N_{res}}$, the flux can be written in the conventional form for the NR approximation:

$$\phi(u)=\frac{\sigma_{p,res}+\sigma_b}{\sigma_{t,res}(u)+\sigma_b} \tag{3.9}$$

Contrary to the NR approximation, the resonance width can be considered wide with respect to the energy loss of a neutron scattered off the resonance isotope. Assuming the mass of the resonance isotope is infinite, no energy loss is expected in the elastic scattering reaction, so the integral of Equation (3.7) for the resonance isotope simplifies to

$$\int_{u-\varepsilon_{res}}^{u} \Sigma_{s,res}(u')\phi(u')\frac{e^{u'-u}}{1-\alpha_{res}}du' = \Sigma_{s,res}(u)\phi(u)\int_{u-\varepsilon_{res}}^{u}\frac{e^{u'-u}}{1-\alpha_{res}}du' = \Sigma_{s,res}(u)\phi(u) \tag{3.10}$$

Then the flux can be written as

$$\phi(u) = \frac{\sum\limits_{iso \neq res} \Sigma_{p,iso}}{\Sigma_{a,res}(u) + \sum\limits_{iso \neq res} \Sigma_{p,iso}} = \frac{\sigma_b}{\sigma_{a,res}(u) + \sigma_b} \tag{3.11}$$

where $\sigma_b = \frac{\sum_{iso \neq res} \Sigma_{p,iso}}{N_{res}}$. Since the NR approximation is still applied to the non-resonant isotopes, the equation above is usually called Narrow Resonance Infinite Mass (NRIM) approximation.

As the two resonance approximations are developed by comparing the resonance width with the scattering energy loss, the NRIM approximation is more suitable for the broad resonances in the epithermal low energy range while the NR approximation is more suitable for the resonances in the high resonance energy range. Ref. [24] presents some verification results for the U-238 capture cross section using the two approximations, as compared to the rigorous slowing-down solution.

The NR and IM approximations are two limiting conditions. The actual resonances are better represented as an interpolation of these limiting conditions, which is the motivation for the Intermediate Resonance (IR) approximation [25]. The portion due to the narrow resonance effect is denoted by the IR factor $\lambda_{iso}\,(0 \le \lambda \le 1)$ for isotope *iso*, so Equation (3.7) is written as

$$\sum_{iso} \Sigma_{t,iso}(u)\phi(u) = \sum_{iso} \lambda_{iso}\Sigma_{p,iso} + \sum_{iso}(1-\lambda_{iso})\Sigma_{s,iso}(u)\phi(u) \tag{3.12}$$

Rearranging the flux gives a similar form to Equations (3.9) and (3.11)

$$\phi(u) = \frac{\lambda_{res}\sigma_{p,res} + \sigma_b}{\sigma_{a,res}(u) + \lambda_{res}\sigma_{s,res}(u) + \sigma_b} \tag{3.13}$$

where $\sigma_b = \frac{\sum_{iso \neq res} \lambda_{iso} \Sigma_{p,iso}}{N_{res}}$. By properly determining the IR factor, the scattering source can be calculated with good accuracy. Discussion of the numerical generation of the IR factor can be found in Reference [24,26].

The neutron spectrum obtained from the resonance approximations can be directly used to determine the collapsed effective cross section. Alternatively, the slowing-down solution is solved to obtain a more accurate neutron spectrum. By varying the background cross section and temperature, an effective cross section or RI table is established for every resonance isotope. For a specific homogeneous problem, once the background cross section is determined, the effective cross section can be estimated by table interpolation.

3.1.2 Heterogeneous Isolated System and Equivalence Theory

Let us consider an isolated heterogeneous model consisting of a single fuel rod surrounded by an infinite moderator. In this case Factor (2) is involved (see beginning of this chapter). The goal is to develop a flux expression similar to that for the homogeneous media with an extra term accounting for the heterogeneous effect. The extra term is then absorbed into the background cross section so that the homogeneous RI table can be directly used for heterogeneous problems. The derivation of the flux starts from the neutron slowing-down equation in collision probability form

$$V_F \Sigma_{t,F}(u)\phi_F(u) = V_F P_{F\to F}(u) Q_F(u) + \sum_{J\in M} V_J P_{J\to F}(u) Q_J(u) \tag{3.14}$$

In this equation, ***F*** is denoted as fuel material and ***M*** denotes materials other than fuel (cladding, coolant, etc.). V_X is the volume of region *X*. We assume a flat flux ϕ_X for each fuel region that has a single mesh without subdivision. $P_{F\to F}(u)$ and $P_{J\to F}(u)$ are the first flight collision probabilities from fuel to fuel and from material *J* to fuel. The source term $Q_X(u)$ can be explicitly written as

$$Q_X(u) = \sum_{iso} \int_{u-\varepsilon_{iso}}^{u} \Sigma_{s,X,iso}(u')\phi_X(u') \frac{e^{u'-u}}{1-\alpha_{iso}} du' \tag{3.15}$$

where ε_{iso} and α_{iso} are the maximum lethargy gain and the fractional energy loss as previously defined. In order to achieve an equivalence relation, the IR approximation is applied to the fuel region, while the NR approximation is applied to other regions. The latter rests on the fact that nuclides of non-fuel regions are light or intermediate, so the resonances can be assumed to be narrow resonances. Utilizing these approximations, the scattering source terms simplify to

$$\begin{gathered} Q_F(u) = \sum_{iso} \lambda_{iso} \Sigma_{p,F,iso} + \sum_{iso} (1-\lambda_{iso}) \Sigma_{s,F,iso}(u) \phi_F(u) = \lambda_F \Sigma_{p,F} + (1-\lambda_F) \Sigma_{s,F}(u) \phi_F(u) \\ Q_J(u) = \Sigma_{p,J} \quad \left(J \in M \right) \end{gathered} \tag{3.16}$$

Note that the notation for fuel region drops isotope index for brevity. Substitution of Equation (3.16) into Equation (3.14) for $Q_F(u)$ and $Q_J(u)$ yields

$$V_F \Sigma_{t,F}(u) \phi_F(u) = V_F P_{F \to F}(u) \left[\lambda_F \Sigma_{p,F} + (1-\lambda_F) \Sigma_{s,F}(u) \phi_F(u) \right] + \sum_{J \in M} V_J P_{J \to F}(u) \Sigma_{p,J} \tag{3.17}$$

Assuming $\Sigma_{t,J}(u) = \Sigma_{p,J}$ for the non-fuel materials and using the reciprocity relation, $V_X P_{X \to Y}(u) \Sigma_{t,X}(u) = V_Y P_{Y \to X}(u) \Sigma_{t,Y}(u)$, Equation (3.17) can be transformed into

$$\Sigma_{t,F}(u) \phi_F(u) = \left(1 - P_{esc}(u)\right) \left[\lambda_F \Sigma_{p,F} + (1-\lambda_F) \Sigma_{s,F}(u) \phi_F(u) \right] + \Sigma_{t,F}(u) P_{esc}(u) \tag{3.18}$$

where the escape probability is defined as $P_{esc}(u) = \sum_{J \in M} P_{F \to J}(u)$. Physically, the escape probability is the first flight collision probability from the fuel region to the non-fuel regions. Various approximations have been developed for evaluating the escape probability [27,28,29,30,31] and the basic idea is to obtain an expression for the flux that gives an analytic form equivalent to the flux for a homogeneous system. Rational approximations have been proven effective to form this equivalence by introducing an equivalence cross section

$$\Sigma_e = \frac{1}{l} \qquad \text{where } l = \text{ mean chord length of the fuel region} \tag{3.19}$$

Table 3-1 shows some examples of rational approximations widely used in lattice codes.

Table 3-1 Rational approximations of escape probability for cylindrical geometry

Item	Formula
Wigner's rational approx.	$P_{esc}(u) = \dfrac{\Sigma_e}{\Sigma_{t,F}(u) + \Sigma_e}$
Bell Factor	$P_{esc}(u) = \dfrac{a_B \Sigma_e}{\Sigma_{t,F}(u) + a_B \Sigma_e} \quad (a_B = 1.1 \sim 1.4)$
Carlvik's two term	$P_{esc}(u) = 2\dfrac{2\Sigma_e}{\Sigma_{t,F}(u) + 2\Sigma_e} - \dfrac{3\Sigma_e}{\Sigma_{t,F}(u) + 3\Sigma_e}$
General N-term rational approx.	$P_{esc}(u) = \sum_{n=1}^{N} b_n \dfrac{a_n \Sigma_e}{\Sigma_{t,F}(u) + a_n \Sigma_e} \quad \left(\sum_{n=1}^{N} b_n = 1 \right)$

For the general case, the N-term rational approximation is substituted into Equation (3.18) to yield the flux of the fuel region,

$$\phi_F(u) = \frac{\sum_{n=1}^{N} b_n \dfrac{\lambda_F \Sigma_{p,F} + a_n \Sigma_e}{\Sigma_{t,F}(u) + a_n \Sigma_e}}{\sum_{n=1}^{N} b_n \dfrac{\Sigma_{t,F}(u) - (1-\lambda_F)\Sigma_{s,F}(u) + a_n \Sigma_e}{\Sigma_{t,F}(u) + a_n \Sigma_e}} \tag{3.20}$$

However, an equivalent form to the homogeneous media can be achieved only for two cases. One is applying NR to the fuel material as well ($\lambda_F = 1$) and then the flux becomes

$$\phi_F(u) = \sum_{n=1}^{N} b_n \frac{\Sigma_{p,F} + a_n \Sigma_e}{\Sigma_{t,F}(u) + a_n \Sigma_e} \tag{3.21}$$

The second is to use the single-term rational approximation, which yields an equivalent form of flux

$$\phi_F(u) = \frac{\lambda_F \Sigma_{p,F} + \Sigma_e}{\Sigma_{a,F}(u) + \lambda_F \Sigma_{s,F}(u) + \Sigma_e} \tag{3.22}$$

We choose Equation (3.22) to formulate the equivalence relation. As before, the resonance interference is neglected, so

$$\phi_F(u) = \frac{\lambda_{res}\sigma_{p,res} + \sigma_b}{\sigma_{a,res}(u) + \lambda_{res}\sigma_{s,res}(u) + \sigma_b} \tag{3.23}$$

where $\sigma_b = \frac{\sum_{iso \neq res} \lambda_{iso}\Sigma_{p,iso} + \Sigma_e}{N_{res}}$. Equation (3.23) has an identical form with Equation (3.13) except the additional term Σ_e defined in σ_b. Therefore, the effective cross section of a heterogeneous case can be obtained from a homogeneous RI table as long as the equivalence cross section is properly determined. This is the equivalence relation that unifies the two effects of resonance self-shielding, e.g., the leakage effect and the volume effect, thus significantly simplifying the self-shielding calculation for heterogeneous cases. Sometimes, the $\lambda_{res}\sigma_{p,res}$ term is absorbed into σ_b,

$$\phi_F(u) = \frac{\sigma_b}{\sigma_{a,res}(u) + \lambda_{res}\sigma_{RS,res}(u) + \sigma_b} \tag{3.24}$$

where $\sigma_b = \frac{\sum_{iso} \lambda_{iso}\Sigma_{p,iso} + \Sigma_e}{N_{res}}$ and $\sigma_{RS,res}(u) = \sigma_{s,res}(u) - \sigma_{p,res}(u)$. Both Equations (3.23) and (3.24) are valid to formulate the RI table, as long as the determination of background cross section is consistent in generating and using the table.

3.1.3 Heterogeneous Lattice System and Dancoff Correction

So far, the heterogeneous consideration is limited to an isolated fuel rod surrounded by infinite moderator. In reality for a fuel lattice system, a neutron that leaves a fuel rod could have its first collision in another fuel rod rather than the moderator. In order words, the fuel escape probability should be reduced due to the shadowing effect of neighboring fuel rods. This effect is modeled by introducing the Dancoff factor to the rational-type fuel escape probability. Compared to an isolated pin cell, the fuel escape probability for a fuel lattice system should be multiplied by $P_M(u)$, the probability that a neutron leaving isotropically from a fuel rod will have its next collision in the materials other than fuel,

$$P_{esc,F}(u) = P_{esc,f}(u) \cdot P_M(u) \tag{3.25}$$

where $P_{esc,f}(u)$ is the fuel escape probability for an isolated pin cell with infinite moderator and $P_{esc,F}(u)$ is the fuel escape probability for the fuel lattice.

Conventionally, the Dancoff factor D is defined by its complementary value $C = 1 - D$, where C is the probability that a neutron leaving isotropically from a fuel rod will enter another fuel rod without any collision in the non-fuel materials. When the fuel is black (absorption macroscopic cross section is considered infinite), the Dancoff factor is simply the P_M, which equals to the first flight blackness of the non-fuel materials. Here we also assume that the cross sections of non-fuel materials are energy independent, so Dancoff factor is energy independent as well. The assumption of black fuel is quite general for the evaluation of Dancoff factor. Analytic expressions for the Dancoff factor have been found for certain geometries [32], while numerical procedures are generally used to determine the Dancoff factor of a complex reactor system [33,34]. To apply the Dancoff factor of black fuel to the realistic fuels that are usually 'grey' materials (finite absorption macroscopic cross section), we consider a regular lattice in which the fuel escape probability of a target fuel pin is given as an infinite sum,

$$\begin{aligned} P_{esc,F}(u) &= P_{esc,f}(u)D_B + P_{esc,f}(u)(1-D_B)\left(1-\gamma_f(u)\right)D_B \\ &+ P_{esc,f}(u)(1-D_B)^2\left(1-\gamma_f(u)\right)^2 D_B + \cdots = \frac{P_{esc,f}(u)D_B}{1-(1-D_B)\left(1-\gamma_f(u)\right)} \end{aligned} \tag{3.26}$$

where D_B is the Dancoff factor and $\gamma_f(u)$ is the first flight blackness of the realistic fuels. Equation (3.26) holds only if the fuel pins are similar, otherwise the series cannot end up with a uniform $\gamma_f(u)$. Furthermore, reciprocity yields the following relation

$$\gamma_f(u) = P_{esc,f}(u)\Sigma_{t,f}(u)l_f \tag{3.27}$$

where $\Sigma_{t,f}(u)$ is the total cross section and l_f is the mean chord length of the fuel. Substitution of Equation (3.27) into Equation (3.26) gives

$$P_{esc,F}(u) = \frac{P_{esc,f}(u)D_B}{1-(1-D_B)\left(1-P_{esc,f}(u)\Sigma_{t,f}(u)l_f\right)} \tag{3.28}$$

By writing $P_{esc,f}(u)$ with the Wigner rational approximation,

$$P_{esc,F}(u) = \frac{\dfrac{1}{\Sigma_{t,f}(u)l_f + 1} D_B}{1-(1-D_B)\left(1-\dfrac{1}{\Sigma_{t,f}(u)l_f + 1}\Sigma_{t,f}(u)l_f\right)} = \frac{D_B\Sigma_e}{\Sigma_{t,f}(u) + D_B\Sigma_e} \tag{3.29}$$

As before, Σ_e is defined as $1/l_f$. Using Equations (3.29) and (3.18), the flux for the fuel lattice can be written as

$$\phi_F(u) = \frac{\sigma_b}{\sigma_{a,res}(u) + \lambda_{res}\sigma_{RS,res}(u) + \sigma_b} \tag{3.30}$$

where $\sigma_b = \frac{\sum_i \lambda_i \Sigma_{p,i} + D_B\Sigma_e}{N_{res}} = \frac{\sum_i \lambda_i \Sigma_{p,i} + \widetilde{\Sigma_e}}{N_{res}}$ and $\widetilde{\Sigma_e} = D_B\Sigma_e$ is the Dancoff corrected equivalence cross section. The limiting conditions for the Dancoff factor correspond to the homogeneous media ($D_B = 0$) and isolated fuel rod with infinite moderator ($D_B = 1$), so the self-shielding effect of the fuel lattice is an interpolation between these two conditions.

To summarize, the Bondarenko-type method derives a simplified flux expression by which the effective cross section can be tabulated only through the background cross section and temperature. Equivalence theory links a basic heterogeneous case (isolated fuel rod) with the homogeneous case, leading to the union of self-shielding effects of volume and leakage. Furthermore, the realistic fuel lattice effect is retrieved by introducing the Dancoff factor as interpolation of the homogeneous media and isolated fuel cases. Compared to the direct slowing-down method, the Bondarenko method is subject to the following approximations:

(1) Resonance approximations are utilized to simplify the scattering source. Although the IR approximation improves the flux accuracy in the epithermal energy range, the determination of the IR factor still requires certain approximations.

(2) The resonance interference effect is neglected.

(3) Rational approximations have been used to determine the escape probability.

(4) The Dancoff correction assumes a regular lattice with similar fuel pins.

(5) The fuel rod is treated as a single region with a flat flux, so the distributed self-shielding effect within the fuel rod is not accounted for.

(6) A temperature distribution within the fuel region is also not accounted for, consistent with (5).

3.2 Embedded Self-shielding Method

ESSM is an extension of the Bondarenko method to account for the Dancoff effect but in the actual problem. Compared to the conventional Bondarenko method where the Dancoff factor is usually evaluated by an auxiliary calculation with black fuel regions separate from the transport calculation, ESSM resolves the heterogeneous effect within the same configuration as the target transport calculation. The Dancoff effect is not calculated explicitly, but embedded in the equivalence cross section which is iteratively determined between interpolating effective cross section and solving a fixed-source transport problem for the geometry and composition of interest, typically a 2-D plane of the core and reflector. In our context, a fixed source transport problem (FSP) for each energy group is defined by only considering the scattering source with a resonance approximation. The iteration concept and formulation of ESSM are discussed in the following two subsections, respectively.

3.2.1 How to Iterate

Assuming the RI table has been generated, ESSM iteratively determines the Dancoff corrected equivalence cross section for a heterogeneous system. Convergence of ESSM iteration is based on two facts. The real physics is that the effective absorption cross section increases as the equivalence cross section increases because the weighting flux under the resonance becomes flatter. This is the correlation already built into the RI table. The effective physics that sets up the multigroup effective cross section for the fixed source calculation behaves in a reverse manner. If an overestimated effective absorption is used in the fixed source problem, the resultant equivalence cross section will be smaller than the one with correct effective absorption, thus leading to a converged effective cross section. To verify this statement, the fuel escape probability of an isolated pin cell is rigorously calculated using the Carlvik method (see Appendix A) for a range of fuel total cross sections. The resultant fuel escape probability is converted to equivalence cross section by using single-term rational approximation:

$$P_{esc} = \frac{\Sigma_e}{\Sigma_{t,F} + \Sigma_e} \tag{3.31}$$

Figure 3.1 shows that the equivalence cross section computed in this way is a monotonically decreasing function of the fuel total cross section. As indicated in Equation (3.29), inclusion of the Dancoff effect for a realistic fuel lattice does not change the monotonic relationship of the equivalence cross section (Dancoff corrected) with the fuel total cross section. This completes the verification for the above statement that the interactions between real and effective physics result in a converged effective cross section.

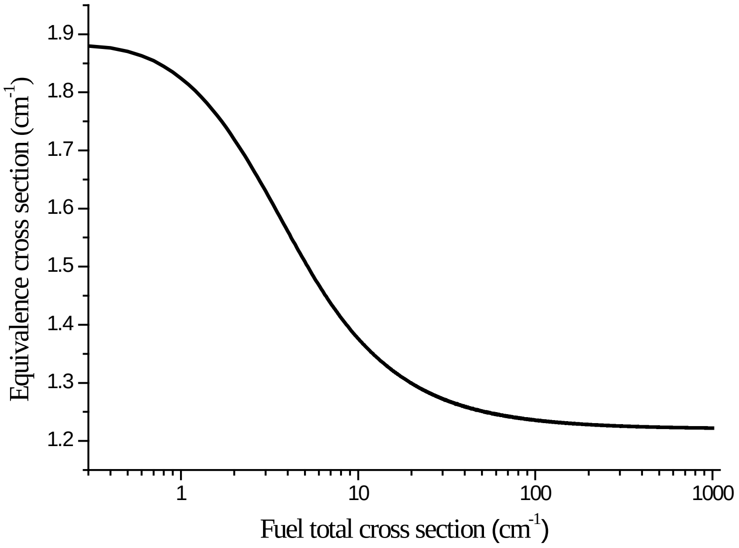

Figure 3.1 Equivalence cross section vs fuel total cross section

Although the equivalence cross section is treated as a constant for the single-term rational approximation, Figure 3.1 indicates a moderate dependence of the equivalence cross section on total cross section (or lethargy). Since the range of equivalence cross section is relatively small and the single-term rational approximation causes the equation for the flux in the fuel lattice to strongly resemble the flux for the homogeneous case, the single-term rational approximation was widely used in the early lattice codes.

The overall concept of ESSM iteration is depicted in Figure 3.2. The iteration target is the true background cross section $\sigma_{b,real}$ and the associated effective cross sections $\sigma_{a,real}$ of every resonant material region of the system. An arbitrary $\sigma_{b,0}$, e.g., with $\widetilde{\Sigma_e} = 0$ may initialize the iteration. Using the RI table, an initial set of effective absorption cross section $\sigma_{a,0}$ is obtained. Next, these $\sigma_{a,0}$'s are used in the FSP to determine a new set of background cross section $\sigma_{b,1}$. Since $\sigma_{a,0} < \sigma_{a,real}$, the computed equivalence cross section is larger than the real one, then $\sigma_{b,1} > \sigma_{b,real}$. Interpolation of the effective cross section using $\sigma_{b,1}$ gives $\sigma_{a,1}$, which should be bigger than $\sigma_{a,real}$, hence the overestimated $\sigma_{a,1}$ yields an underestimated $\sigma_{b,2}$. The table interpolation and FSP solutions repeat until convergence of σ_b and σ_a is achieved. A detailed definition of the FSP and the determination of σ_b from the FSP will be discussed in the next subsection.

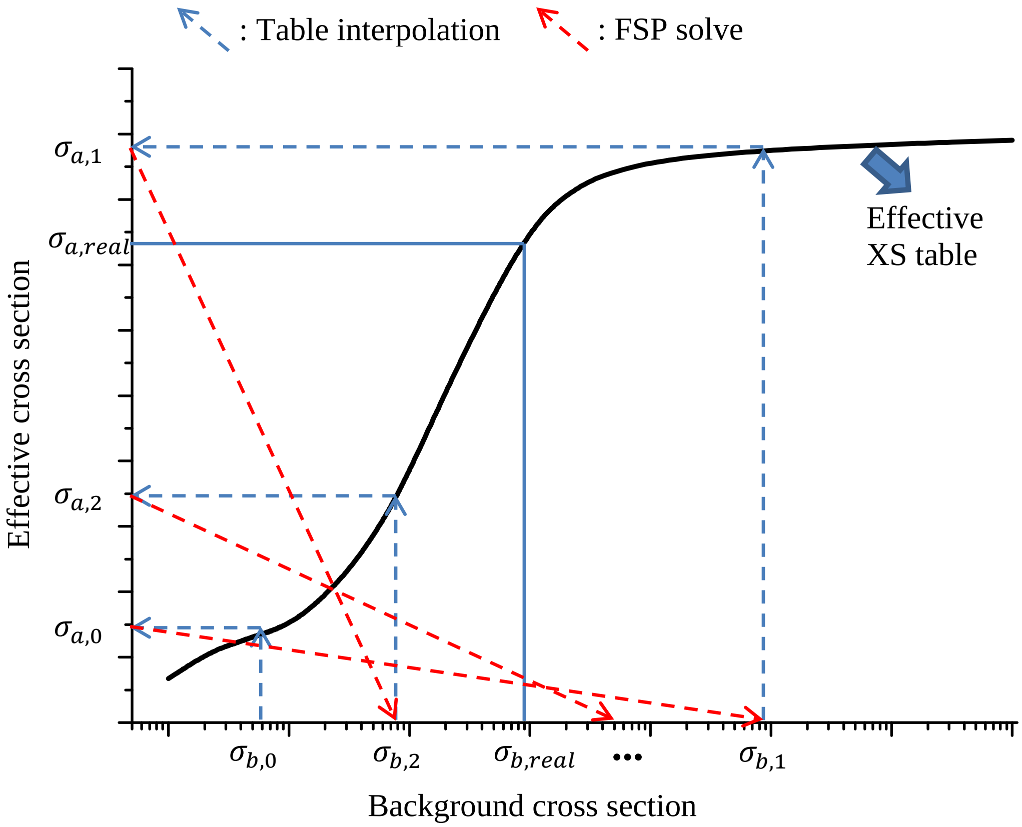

Figure 3.2 Iteration scheme of ESSM

3.2.2 Formulation of ESSM

For the ESSM calculation, one could generate the RI table by a series of homogeneous problems using either a resonance approximation or a slowing-down calculation. However, a more consistent way is to use a set of heterogeneous pin cell configurations in the realistic reactor geometry by varying the fuel and moderator densities or fuel to moderator ratios to achieve a range of background cross sections. The transition from homogeneous to 1D cylindrical geometry was first attempted when performing verification calculations in Ref. [35] and later this approach was adopted for the generation of subgroup weights in the HELIOS code [36]. Other efforts employing the heterogeneous RI table rather than the homogeneous RI table can be found in Ref. [37,38]. ESSM employs a search for the equivalence cross section by iterating between the pre-computed RI tables and the fixed source problem, and this consistency between generating and using the tables is essential for the accuracy of the method.

The multigroup form of Equation (3.30) can be obtained by first rearranging the denominator to the left hand side, and then integrating over the group boundaries,

$$\phi_{F,g} = \frac{\sigma_{b,g}\Delta u_g}{\sigma_{a,res,g} + \lambda_{res}\sigma_{RS,res,g} + \sigma_{b,g}} \tag{3.32}$$

As discussed, $\widetilde{\Sigma_e}$ is slightly energy dependent, so the $\widetilde{\Sigma_{e,g}}$ term in $\sigma_{b,g}$ is determined by forcing the equality of Equation (3.32). Alternatively, $\sigma_{b,g}$ can be solved in terms of the multigroup flux

$$\sigma_{b,g} = \frac{\left(\sigma_{a,res,g} + \lambda_{res}\sigma_{RS,res,g}\right)\phi_{F,g}}{\Delta u_g - \phi_{F,g}} \tag{3.33}$$

Equation (3.33) indicates that if the effective cross section of a resonance isotope for a heterogeneous problem is obtained, one may estimate the background cross section by solving a FSP for the same heterogeneous case. The advantage of estimating the background cross section from the FSP is that the Dancoff corrected equivalence cross section is already embedded into the background cross section, so a separate routine to compute Dancoff factor is not required to determine the lattice shielding effect.

To vary the background cross section, a series of 2-D pin cell problems are defined in Table 3-2. Case 3 is the base case which is a typical PWR pin cell. The other cases, by varying the cell pitch, moderator density or fuel density, give a range of effective cross sections against background cross sections.

Table 3-2 Variations of 2-D pin cell for RI table generation

Case #	1	2	3	4	5	6	7	8	9	10
Ratio of pitch	1.0	1.0	1.0	1.13	1.35	1.35	1.35	1.35	1.35	1.35
Ratio of Mod. density	0.3	0.7	1.0	1.0	1.0	1.0	1.0	1.0	1.0	1.0
Ratio of fuel density	1.0	1.0	1.0	1.0	1.0	0.7	0.5	0.25	0.1	0.025

Specifically, for each configuration the multigroup effective cross sections are computed from the exact 2-D slowing-down calculation. To obtain the corresponding background cross section, the unknown flux in Equation (3.33) is solved from a fixed source problem of the same 2-D pin cell configuration formulated by IR approximation

$$\nabla \cdot \Omega \varphi_g(r,\Omega) + \Sigma_{t,g}(r)\psi_g(r,\Omega) = \frac{1}{4\pi}\Big[(1-\lambda)\big(\Sigma_{RS,g}(r) + \Sigma_p(r)\big)\phi_g(r) + \lambda\Sigma_p(r)\Delta u_g\Big] \quad (3.34)$$

Note that the multigroup effective cross sections in this equation are computed from the 2-D slowing-down calculation. To summarize, the procedure of generating heterogeneous RI table for ESSM consists of three steps: (a) Solve the exact slowing-down equation for every pin cell configuration to obtain the multigroup effective cross sections; (b) Solve Equation (3.34) to obtain the scalar flux for the fixed source problem for every pin cell configuration; (c) Obtain the background cross section by Equation (3.33) so that the effective cross section and background cross section are linked. This procedure is performed for every resonance isotope independently at several temperatures of interest.

When performing the resonance calculation for a specific problem, ESSM directly uses these RI tables for cross section interpolation. An initial set of self-shielded cross sections can be obtained by assuming $\widetilde{\Sigma_e} = 0$ so that $\sigma_b = \lambda_F \Sigma_{p,F} / N_{res}$. With the coefficients of these multigroup shielded cross sections, Equation (3.34) is solved for every 2-D plane and the resulting flux is used in Equation (3.33) to update the background cross sections. Then a new set of self-shielded cross sections can be obtained by RI table interpolation. The procedure iterates until the equivalence cross sections $\widetilde{\Sigma_e}$ of all resonant regions of the 2-D plane converge.

To be consistent with RI table generation, the ESSM iteration should be performed for each resonance isotope independently, where other resonance isotopes are treated as background isotopes with only potential scattering. However, in order to save computing time, a simplification was introduced into the original description of ESSM that the ESSM iteration is performed only once with all the resonance isotopes combined as a whole absorber [16]. The resonance interference can be considered later with separate interference models without affecting the ESSM iteration loop. This assumption might be good for the fresh fuel, but could bias the results for complicated material compositions, say MOX fuel or depleted fuel. The conventional interference models will be discussed in the last section of this chapter.

Also, it has been verified that $\lambda\sigma_{RS,g}$ can be eliminated in Equations (3.33) and (3.34) without sacrificing accuracy, as long as they are consistently eliminated when generating and using RI tables [36,38]. This can be explained as $\lambda\sigma_{RS,g}$ only imposes a shift of RI versus background cross sections. By eliminating $\lambda\sigma_{RS,g}$, Equations (3.33) and (3.34) simplify to

$$\sigma_{b,g} = \frac{\sigma_{a,res,g}\phi_{F,g}}{\Delta u_g - \phi_{F,g}} \tag{3.35}$$

$$\nabla \cdot \Omega\varphi_g(r,\Omega) + \Sigma_{t,g}(r)\psi_g(r,\Omega) = \frac{1}{4\pi}\Big[\big(\Sigma_{s,g}(r) - \lambda\Sigma_p(r)\big)\phi_g(r) + \lambda\Sigma_p(r)\Delta u_g\Big] \tag{3.36}$$

These two equations are actually used in the ESSM calculation.

The ESSM differs from the Bondarenko method, because the equivalence cross section is evaluated by iteration rather than using the rational approximation and the Dancoff correction. Other approximations such as the need for a resonance approximation (e.g., IR), neglect of resonance interference and the need for a single fuel region without distributed self-shielding effects are still inherited from the Bondarenko method. Although one can extend the method to solve a multiple fuel-region problem by calculating the multi-region fluxes from Equation (3.36) and evaluate the background cross sections of different annuli using different fluxes, the same RI table pre-computed from a single fuel region is used for all subregions, which prematurely assumes the correlations between shielded cross section and background cross section for different annuli are identical to the single fuel region. This assumption leads to significant errors in the shielded cross sections. A further investigation of this issue can be found in the last section of this chapter.

3.3 Subgroup Method

The original idea of the subgroup method (also named the multiband method) is substantially different from the multigroup concept. As is seen in solving the slowing-down equation, a sufficient number of energy groups is needed to assure that the variation of cross section within a group is small. Rather than dividing the energy range into more and more groups which is computationally expensive, the subgroup method proceeds by dividing the cross section magnitude within a broad Group *g* into a number of cross section bands (subgroups) as shown in Figure 3.3. The cross section belonging to a subgroup is in general discontinuous with regard to energy. In spite of many resonances within a broad group, a small number of subgroups are able to cover the range of the resonance cross section. Each subgroup is associated with a weight that relates to the probability that the energy dependent cross section falls into this subgroup. Evaluating a RI by the subgroup method is mathematically equivalent to performing the Lebesque integration instead of Riemann integration.

In practice, the detailed cross section behavior of each coarse energy group is replaced by its subgroup probability density representation that preserves certain integrals. There are two methods for determining the subgroup probability tables. The first is the physical probability table, in which the RI tables are converted into a set of subgroup levels and weights by preserving either the RI or effective cross section over a range of background cross sections [36]. The second method utilizes the mathematical probability table. Instead of preserving the RI, it preserves the cross section moments by processing the point-wise cross section data [39]. The l_{th} moment of the cross section of reaction channel x at group g is defined as

$$M_{x,g,l} = \frac{1}{\Delta u_g} \int_{u_{g-1}}^{u_g} \sigma_x(u) \sigma_t(u)^l du \tag{3.37}$$

where l is a set of integers that can be positive or negative. For example, $M_{x,g,l}$ is the infinite diluted RI when $l = 0$ and is the fully shielded RI when $l = -1$. Since all self-shielding conditions appear between this two limiting conditions, the moment based method was then generalized to preserve a few non-integer moments ranging from -1 to 0 [40].

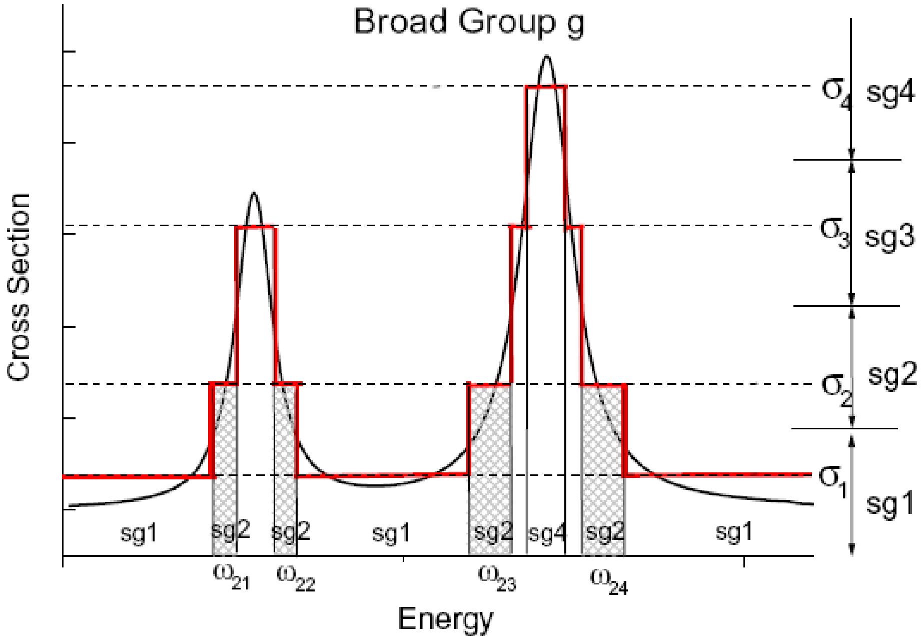

Figure 3.3 Subgroup levels and weights [38]

Since the physical probability table is more widely used, the following content will concentrate on this approach. Transformation of integration variable from neutron energy to cross section for the resonance integral gives

$$\sigma_{x,g} = \frac{\int_{u_{g-1}}^{u_g} \sigma_x(u)\phi(u)du}{\int_{u_{g-1}}^{u_g} \phi(u)du} = \frac{\int_{\sigma_{\min,g}}^{\sigma_{\max,g}} \sigma_x(\sigma)\phi(\sigma)\frac{du}{d\sigma}d\sigma}{\int_{\sigma_{\min,g}}^{\sigma_{\max,g}} \phi(\sigma)\frac{du}{d\sigma}d\sigma} \tag{3.38}$$

The integrals of Equation (3.38) can be cast into a quadrature form represented by the subgroup levels $\sigma_{x,g,n}$ and weights $w_{x,g,n}$

$$\sigma_{x,g} \cong \frac{\sum_n \sigma_{x,g,n}\phi_{g,n}w_{x,g,n}}{\sum_n \phi_{g,n}w_{x,g,n}} \tag{3.39}$$

where $\phi_{g,n}$ is the level dependent flux. Assuming the subgroup parameters have been determined, the application of the subgroup method involves obtaining the level dependent flux from a fixed source transport problem. Similar to ESSM, a fixed source problem for the subgroup method is defined by considering the scattering source with a resonance approximation. A typical fixed source problem for subgroup level *n* with the IR approximation is given as

$$\begin{aligned} &\nabla\cdot\Omega\psi_{g,n}(r,\Omega) + \left[\Sigma_{a,g,n}(r) + \Sigma_{s,g}(r)\right]\psi_{g,n}(r,\Omega) \\ &= \frac{1}{4\pi}\left[\left(\Sigma_{s,g}(r) - \lambda\Sigma_p(r)\right)\phi_{g,n}(r) + \lambda\Sigma_p(r)\Delta u_g\right] \end{aligned} \tag{3.40}$$

where $\phi_{g,n}(r)$ and $\psi_{g,n}(r,\Omega)$ are the level dependent scalar flux and angular flux. In practice, instead of directly using the level dependent flux, it is customary to rewrite the flux using the IR approximation

$$\phi_{g,n} = \frac{\Delta u_g \sigma_{b,g,n}}{\sigma_{a,g,n} + \sigma_{b,g,n}} \tag{3.41}$$

where $\sigma_{b,g,n} = \lambda\sigma_p + \sigma_{e,g,n}$ is the level dependent background cross section. No resonance interference among isotopes is assumed within the energy group *g*. As a practical matter, Equation (3.41) is used to replace the flux in Equation (3.39) for evaluation of the effective cross sections

$$\sigma_{x,g} \cong \frac{\sum_n \sigma_{x,g,n} \dfrac{\sigma_{b,g,n}}{\sigma_{a,g,n}+\sigma_{b,g,n}} w_{x,g,n}}{\sum_n \dfrac{\sigma_{b,g,n}}{\sigma_{a,g,n}+\sigma_{b,g,n}} w_{x,g,n}} \tag{3.42}$$

This alternative is chosen because the dependence of $\sigma_{b,g,n}$ on $\sigma_{a,g,n}$ is much weaker than the dependence of $\phi_{g,n}$ on $\sigma_{a,g,n}$. The number of $\sigma_{b,g,n}$ capable of describing this dependence is therefore smaller than the number of subgroup levels used in the quadrature for computing the effective cross section. Thus fewer fixed source calculations are needed. The level dependent fluxes solved from the fixed source problem are converted to background cross section by reversing Equation (3.41), so a table of $\sigma_{b,g}(\sigma_a)$ or $\sigma_{e,g}(\sigma_a)$ is established. By interpolation, one could obtain $\sigma_{e,g,n}$ for all levels of the subgroup quadrature and finally compute the effective cross section by Equation (3.42).

Since the flux can be solved for any region from the fixed source problem, the subgroup method is not limited to a single mesh in the fuel region, which is the basic assumption of the conventional Bondarenko method. Although Equation (3.41) utilizes the equivalence relation, a subtlety is that in the subgroup method the equivalence cross section embedded in the background cross section is no longer a constant, but depends on the subgroup level. Therefore, compared to the Bondarenko-type method, the subgroup method can resolve the distributed self-shielding effect within a fuel rod to a certain extent.

Another approximation for the subgroup method to save computation time is to group the resonance isotopes into several categories. Each category contains a subset of resonance isotopes having overlapping, but not equally strong resonances. The fixed source problem is solved per category rather than per resonance isotope. A detailed description of this simplification can be found in Ref. [36].

The subgroup parameters (levels and weights) are determined by searching for the desired fit from a set of pre-computed RI tables parameterized by background cross sections. Here the RI table is the same as discussed in the previous sections. For example, one could determine the subgroup weights by solving a least squares problem

$$\min f(w) = \sum_{k=1}^{K} \left(\frac{1}{RI_{g,k}} \sum_{n=1}^{N} w_{g,n} \sigma_{g,n} \phi_{g,n} - 1 \right)^2 \tag{3.43}$$

where N is the number of subgroup levels and K is the number of background cross section in the RI table (K>N). The subgroup levels $\sigma_{g,n}$ are usually chosen to be the same for different temperatures. A procedure of trial and error is needed for determination of $\sigma_{g,n}$ to minimize the error of Equation (3.43) for all temperatures. Since the subgroup method is mathematically a quadrature approximation of the RIs over a range of background cross sections, it is characterized as an integral table based method.

In spite of the advantages, the resonance interference effect is still neglected in the above description and is difficult to be accounted for within the framework of the subgroup method. Furthermore, the subgroup method has an issue with treating a non-uniform temperature profile within the fuel region. These issues will be discussed in the next section.

3.4 Limitations of Integral Table Based Methods

Since the application of integral table based methods only involves multigroup calculations, these methods are much more efficient than directly solving the CE slowing-down equation for the specific configuration. However, the derivation of integral table based methods introduces a number of approximations as discussed in previous sections. This section is dedicated to three of the most important issues, resonance interference, distributed self-shielding (multiple fuel regions) and non-uniform temperature profile within the fuel rod.

3.4.1 Resonance Interference

The resonance interference effect is a long-standing problem that arises from the overlapping in energy of cross sections from different resonance isotopes. To illustrate, the energy dependent absorption cross sections of U-235 and U-238 are plotted for two selected energy ranges in Figure 3.4. In Condition A, the task is to evaluate the multigroup effective cross section of U-235 around the 6.67eV resonance of U-238. Due to the presence of U-238, the flux is depressed around the resonance, so the effective cross section of U-235 is increased because the relatively larger cross section is given more weight than the smaller cross section. However, if the same problem is investigated at a different energy range in Condition B where resonances of two isotopes overlap, the effective cross section of U-235 is reduced since less weight is given to the relatively larger cross section. Therefore, the resonance interference effect on effective cross sections could be arbitrary, depending on the specific situation of cross section overlapping.

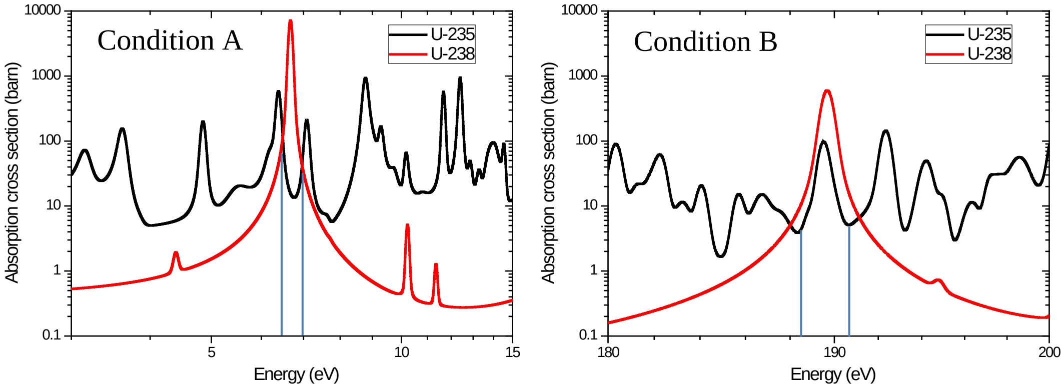

Figure 3.4 Resonance interference effect between U-238 and U-235

As presented, the integral tables (or subgroup parameters) are generally determined for each resonance isotope independently, so resonance interference is neglected at this step. One prescription to address this problem is to perform the Bondarenko iteration at the multigroup level [11], which was first introduced by the WIMS code and then widely used in other lattice codes. According to Equation (3.30), the IR flux considering absorption of other resonance isotopes is written as

$$\phi_F(u) = \frac{\sigma_b}{\sigma_{a,res}(u) + \lambda_{res}\sigma_{RS,res}(u) + \sigma_{a,other}(u) + \sigma_b} \tag{3.44}$$

where $\sigma_{a,other}(u) = \frac{1}{N_{res}} \sum_{iso \neq res} \sigma_{a,iso}(u)$ (summation is over all other resonance isotopes). Instead of using the continuous-energy cross section which is unattainable during the conventional multigroup calculation, the multigroup absorption cross section is used to model the flux depression due to absorption of the other resonance isotopes,

$$\phi_F(u) = \frac{\sigma_b}{\sigma_{a,res}(u) + \lambda_{res}\sigma_{RS,res}(u) + \overline{\sigma_{a,other,g}} + \sigma_b} \tag{3.45}$$

where $\overline{\sigma_{a,other,g}} = \frac{1}{N_{res}} \sum_{iso \neq res} \sigma_{a,iso,g}$. When evaluating the effective cross section, the contribution of other resonance isotopes can be absorbed into the background cross section

$$\begin{aligned}\sigma_{x,res,g} &= \frac{\displaystyle\int_{u_{g-1}}^{u_g} \sigma_x(u) \frac{\sigma_b}{\sigma_{a,res}(u) + \lambda_{res}\sigma_{RS,res}(u) + \overline{\sigma_{a,other,g}} + \sigma_b} du}{\displaystyle\int_{u_{g-1}}^{u_g} \frac{\sigma_b}{\sigma_{a,res}(u) + \lambda_{res}\sigma_{RS,res}(u) + \overline{\sigma_{a,other,g}} + \sigma_b} du} \\ &= \frac{\displaystyle\int_{u_{g-1}}^{u_g} \sigma_x(u) \frac{1}{\sigma_{a,res}(u) + \lambda_{res}\sigma_{RS,res}(u) + \widetilde{\sigma_b}} du}{\displaystyle\int_{u_{g-1}}^{u_g} \frac{1}{\sigma_{a,res}(u) + \lambda_{res}\sigma_{RS,res}(u) + \widetilde{\sigma_b}} du}\end{aligned} \tag{3.46}$$

where $\widetilde{\sigma_b} = \overline{\sigma_{a,other,g}} + \sigma_b$. Equation (3.46) indicates that the original effective cross section table can be used for the case that incorporates resonance interference. The background cross section is increased by the absorption of other resonance isotopes. The same treatment is applicable to the subgroup method as well, so the subgroup level dependent flux is redefined as

$$\phi_{g,n} = \frac{\Delta u_g \sigma_{b,g,n}}{\sigma_{a,g,n} + \overline{\sigma_{a,other,g}} + \sigma_{b,g,n}} \tag{3.47}$$

Since determination of $\overline{\sigma_{a,other,g}}$ requires resonance calculation of other isotopes, iteration is involved.

As only the multigroup cross section is needed, implementation of Bondarenko iteration into a typical lattice code requires trivial work. However, Bondarenko iteration always ends up with an increased background cross section $\widetilde{\sigma_b}$, resulting in a greater effective cross section than the one without interference. This contradicts the fact that the interference effect on effective cross section may be negative or positive. Therefore, Bondarenko iteration could result in a systematic error by overestimating the effective cross section.

In addition, efforts were made to incorporate the interference effect by extending the dimension of the RI table or subgroup parameters using the density ratio of two resonance isotopes [26,41]. The difficulty for these methods occurs when the number of resonance isotopes becomes large, e.g. for MOX fuel or depleted fuel. This is due to the fact that the increased size of the RI table depends on the number and significance of the resonance isotopes in the specific problem, and this can be difficult to and inefficient to carry out. As suggested in Ref. [42], it is necessary to utilize continuous energy cross section data in order to fundamentally solve this problem. The new method proposed in the current work utilizes continuous energy cross sections to address this issue.

3.4.2 Distributed Self-shielding Effect

High-fidelity reactor simulations of today require a resonance self-shielding model which is able to resolve the spatial effects within the fuel rod for multi-region depletion and power density calculation [43]. The Bondarenko method and ESSM primarily rely on equivalence theory, which was originally developed for a single fuel region without subdivision. For distributed self-shielding with multiple fuel regions, the asymptotic behavior of the region-wise fuel escape probability can be studied to show it is not valid to compute $P_{esc}(u)$ using the rational approximation [44]. According to the multi-term rational approximation, which includes the single-term rational approximation as a special case,

$$P_{esc}(u) = \sum_{n=1}^{N} b_n \frac{a_n \Sigma_e}{\Sigma_{t,F}(u) + a_n \Sigma_e} \qquad \left(\sum_{n=1}^{N} b_n = 1 \right) \tag{3.48}$$

$P_{esc}(u)$ behaves like $\frac{1}{\Sigma_{t,F} l}$ when $\Sigma_{t,F} \to \infty$, where $l = 1 / \sum_{n=1}^{N} \frac{b_n}{a_n \Sigma_e} = const$. If the rational approximation is also a good approximation for computing region-wise $P_{esc,i}(u)$, the multiplication of fuel escape probability and total cross section $P_{esc,i}\Sigma_{t,F}$ for every fuel ring should approach a non-zero constant $\frac{1}{l}$ as $\Sigma_{t,F} \to \infty$. Verification of this consequence is performed using the Carlvik method to compute the collision probability (see Appendix A). The fuel rod is subdivided into six equal-volume rings. Figure 3.5 shows $P_{esc,i}\Sigma_{t,F}$ for different $\Sigma_{t,F}$ at different fuel rings. It turns out that only the results for the whole fuel region and the outermost ring approach a constant as $\Sigma_{t,F} \to \infty$, but these two constants are different, indicating that a rational approximation suitable for the whole fuel region might not work for the outermost ring. Moreover, $P_{esc,i}\Sigma_{t,F}$ for the inner rings tend to zero because of the exponential behavior of $P_{esc,i}(u)$ due to neutron attenuation from the outer rings. In conclusion, the conventional rational approximation is not applicable to the distributed self-shielding case. If the equivalence form is still desired, an energy dependent equivalence cross section should be allowed. Since the subgroup method computes the subgroup level dependent equivalence cross section, this occurs to a limited extent and leads to a better representation of the distributed self-shielding effect.

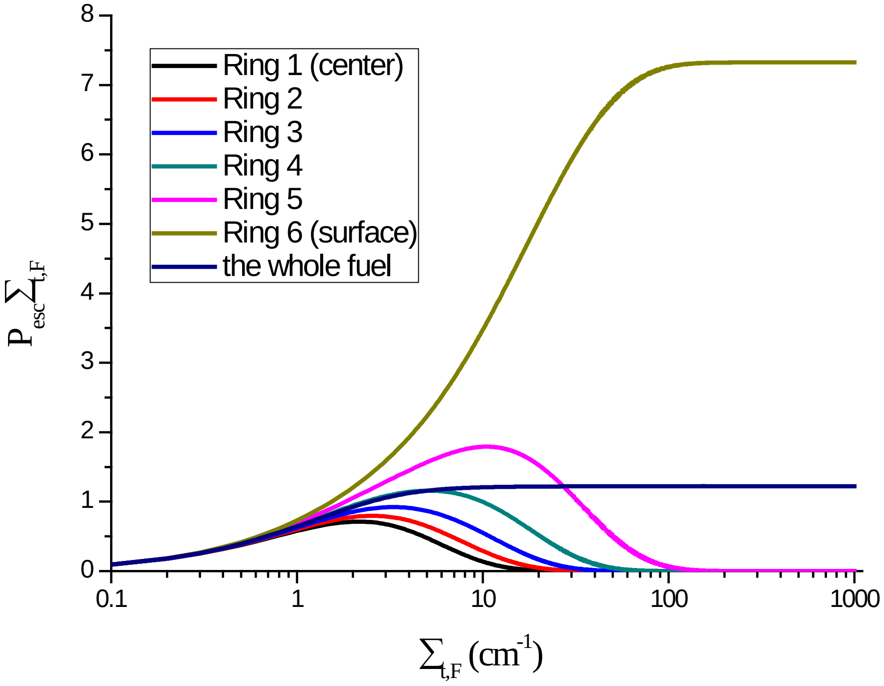

Figure 3.5 $P_{esc}\Sigma_{t,F}$ vs $\Sigma_{t,F}$ at different fuel rings

There have been a few efforts to develop spatially-dependent self-shielding models [44,45,46] within the framework of the Bondarenko method. The multiple fuel region escape probability is calculated by either extending the rational type approximation or rigorous computation from the point-wise cross section data. The shielded cross sections are still represented in terms of RIs, with extra coefficients accounting for the spatial effects. An important limitation of these models is however, the inability to account for the non-uniform temperature distribution within the fuel rod.

3.4.3 Non-uniform Temperature Effect

In a conventional lattice calculation, a so-called ‘effective temperature’ (single value) is chosen to replace the realistic temperature distribution in the fuel rod. Various approaches to obtain the effective temperature are discussed in Ref. [47]. The concept behind these approaches is to preserve the neutron capture within the fuel rod in the resonance range for a uniform effective temperature with the neutron capture corresponding to a specific temperature profile. However, the effective temperature model cannot be used for a non-uniform temperature profile if one wants to obtain accurate self-shielded cross sections in every subregion of the fuel, such as needed for an accurate intra-pin transport calculation with depletion. Although the subgroup method reduces the dependence on equivalence theory, which leads to a better representation of distributed self-shielding, the lack of a firm theoretical foundation in treating non-uniform temperature restricts its applicability, particularly to direct whole core problems with thermal feedback.

The issue is as follows. In the subgroup method, subgroup levels are given to be temperature independent, and subgroup weights are generated to be temperature dependent to account for the Doppler broadening of cross sections. When performing the self-shielding calculation for a non-uniform temperature profile of a fuel rod, for each subgroup of a resonance isotope, the subgroup levels in different fuel annuli are the same in spite of the different temperatures. This imposes an inconsistency between the cross sections used for the subgroup fixed source calculation and the Doppler broadened cross sections at the true temperature. Consequently, the equivalence cross sections may be biased. A prescription to address this deficiency is to adjust the cross section of each region to be temperature dependent, so that the correct self-shielding effect regarding non-uniform temperature can be retrieved. Two approaches were developed according to this concept [48,49].

The first one is subgroup level adjustment by subgroup weights

$$\sigma_{a,g,n}(T_k)=\frac{w_{a,g,n}(T_k)}{w_{a,g,n}(T_{ave})}\sigma_{a,g,n} \tag{3.49}$$

In this equation, the temperature independent absorption level $\sigma_{a,g,n}$ at group g for level n is adjusted by the ratio of subgroup weights at T_k in region k and at T_{ave}, the average temperature of the fuel in the subgroup solving domain. This adjustment preserves the infinite diluted RI if the weights of average temperature are used for all regions,

$$RI_{a,g}(T_k)=\sum_n \sigma_{a,g,n}(T_k)w_{a,g,n}(T_{ave})=\sum_n \sigma_{a,g,n}w_{a,g,n}(T_k) \tag{3.50}$$

The adjusted subgroup levels $\sigma_{a,g,n}(T_k)$ are then used to solve the subgroup FSP to determine the equivalence cross section. Finally, the adjusted subgroup levels $\sigma_{a,g,n}(T_k)$ and subgroup weights at average temperature $w_{a,g,n}(T_{ave})$ are used to compute the effective cross section,

$$\sigma_{a,g}=\frac{\sum_n \sigma_{a,g,n}(T_k)\frac{\sigma_{b,g,n}}{\sigma_{a,g,n}(T_k)+\sigma_{a,other,g}+\sigma_{b,g,n}}w_{a,g,n}(T_{ave})}{\sum_n \frac{\sigma_{b,g,n}}{\sigma_{a,g,n}(T_k)+\sigma_{a,other,g}+\sigma_{b,g,n}}w_{a,g,n}(T_{ave})} \tag{3.51}$$

In this equation, $\sigma_{a,other,g}$ is the interference term accounting for the flux depression due to other resonance isotopes. For the effective cross section of fission and scattering, original subgroup levels and weights can be used with temperature dependent flux term identical to the absorption. If the subgroup weights are physical, which means that the weights are the probability that the energy dependent cross section falls into the given subgroup cross section band, this approach could work properly. However, the subgroup weights are in fact generated by solving a least squares fit problem and thus not physical and negative and small weights may occur. Therefore, some of the adjusted subgroup levels might be negative or extremely large, which is not desired.

The second approach adjusts the subgroup level directly by the effective absorption at the target and average temperatures,

$$\sigma_{a,g,n}(T_k) = \frac{\sigma_{a,g}(T_k)}{\sigma_{a,g}(T_{ave})}\sigma_{a,g,n} = f(T_k)\sigma_{a,g,n} \tag{3.52}$$

The ratio of effective cross section is approximately determined as

$$f(T_k) = \frac{\sigma(T_k)}{\sigma(T_{ave})} = \frac{RI(T_k,\sigma_b)}{RI(T_{ave},\sigma_b)}\frac{\sigma_b - RI(T_{ave},\sigma_b)}{\sigma_b - RI(T_k,\sigma_b)} \tag{3.53}$$

Since we do not have an equivalence cross section before solving the subgroup FSP, σ_b is approximated as $\sigma_b \cong \lambda\sigma_p$. Note the adjustment factor is the ratio of two absorption cross sections at a specified σ_b and thus has no subgroup level dependence. The adjusted subgroup levels are used to solve the equivalence cross section only, so the effective absorption is written as

$$\sigma_{a,g} = \frac{\sum_n \sigma_{a,g,n}\dfrac{\sigma_{b,g,n}}{\sigma_{a,g,n}(T_k)+\sigma_{x,g}+\sigma_{b,g,n}}w_{a,g,n}(T_k)}{\sum_n \dfrac{\sigma_{b,g,n}}{\sigma_{a,g,n}(T_k)+\sigma_{x,g}+\sigma_{b,g,n}}w_{a,g,n}(T_k)} \tag{3.54}$$

This equation also preserves the effective cross section for the infinite dilution case.

As reported in Ref. [48,49], both approaches improved the accuracy of the fuel temperature coefficient by more than 10%. However, no detailed comparisons of the spatially dependent reaction rates with regard to the non-uniform temperature profiles were provided. The numerical results in Chapter 5 will show that even with the extension [48], the subgroup method cannot account for the spatial temperature profile if accurate intra-pin effective cross sections are needed.

3.4.4 Summary

Three limitations of the integral table based methods are discussed in this section. The existing methods to treat those issues either yield biased results, such as the interference treatment using Bondarenko iteration, or restrict the prescription to an individual issue, such as the distributed self-shielding models without considering the non-uniform temperature profile or resonance interference. In next chapter, a comprehensive resonance self-shielding method is developed to account for all three issues, i.e., resonance interference, distributed self-shielding, and non-uniform temperature profile.

Chapter 4

Extended ESSM with Quasi-1D Slowing-down Correction

4.1 Motivation of New Method

The extended ESSM with quasi-1D slowing-down correction method is a fusion of the two types of methods presented in Chapter 2 and Chapter 3. The assumption that underpins this new method is that the global Dancoff effect is treated satisfactorily with ESSM, while the effects of radial fuel regions and resonance interference are local phenomena that can be treated with a continuous energy slowing-down equation for the local geometry. Thus conventional ESSM is still performed for every 2-D plane of the problem as a baseline calculation to capture the global resonance (Dancoff) effects. In the meantime, the new method introduces a 1-D model to explicitly account for the intra-pin (local) effects. To connect the local 1-D fuel pin calculation with the global ESSM calculation, a quasi-1D form of the slowing-down equation is developed that incorporates the equivalence cross section that accounts for the boundary conditions implicitly, rather than using explicit boundary conditions, hence ‘quasi-1D’. In addition, effort has been made to improve the efficiency of the quasi-1D slowing-down solver. Finally, a correction procedure is designed to modify the effective cross section obtained from ESSM by using correction factors calculated from the quasi-1D model to account for radial shielding, non-uniform temperature effect, and resonance interference.

The proposed method is able to address these three issues arising from the use of conventional integral table based methods. Although the distributed self-shielding within the fuel rod is not a requirement for conventional lattice calculations, it plays an important role in direct whole core transport calculation. First, multi-physics analysis requires high-fidelity resonance self-shielding model. On one hand, by properly determining the radially dependent shielded cross sections, one can improve the distribution of heat generation which will benefit the T/H calculation. On the other hand, the temperature distribution obtained from T/H feedback requires the resonance model account for the non-uniform temperature effect. In addition, the radially shielded cross sections affect the determination of the radial burnup distribution in the fuel. In particular, the plutonium build-up at the fuel surface requires careful attention. The so-called plutonium ‘rim effect' occurs at high burnup of UO2 LWR fuel on a thin layer near the fuel surface (on the order of 100 microns). The thermal conductivity of the fuel can be significantly reduced in the rim zone and the power density is raised due to the abundance of Pu-239. This phenomenon could be correctly modeled only if the plutonium build-up at the rim zone is accurately estimated, which in turn depends on the estimation of U-238 absorption rate near the fuel surface, and this is a sensitive function of the self-shielding. In addition to the distributed self-shielding, the explicit model of resonance interference will help improve the energy dependent reaction rates of resonance isotopes, such as Pu-239 in the outer rim of the fuel or for a complex fuel composition such as MOX, Gd bearing fuel or depleted fuel, in order to better estimate the eigenvalue and power distribution.

4.2 Derivation of the Quasi-1D Slowing-down Equation

Consider a fuel rod which is divided into multiple annuli, where different annuli may have different temperatures and material compositions. The neutron flux in region *i* of the fuel rod is given by the collision probability form of the transport equation with the source term only including scattering (same assumptions for resonance energy range as in Chapter 2)

$$V_i \Sigma_{t,i}(u)\phi_i(u) = \sum_{j \in F} V_j P_{j\to i}(u) Q_j(u) + \sum_{k \in M} V_k P_{k\to i}(u) Q_k(u) \tag{4.1}$$

where V_i, $\Sigma_{t,i}(u)$ and $\phi_i(u)$ are the volume, total cross section and scalar flux of region *i*. $P_{j\to i}(u)$ is the first flight collision probability from region *j* to *i* and $Q_j(u)$ is the scattering source of region *j*. Applying the NR approximation for the scattering source of the non-fuel regions yields

$$V_i\Sigma_{t,i}(u)\phi_i(u) = \sum_{j\in F} V_j P_{j\to i}(u) Q_j(u) + \sum_{k\in M} V_k P_{k\to i}(u)\Sigma_{p,k} \tag{4.2}$$

By utilizing the reciprocity relation $V_X P_{X\to Y}(u)\Sigma_{t,X}(u) = V_Y P_{Y\to X}(u)\Sigma_{t,Y}(u)$,

$$\phi_i(u) = \sum_{j\in F} \frac{P_{i\to j}(u)}{\Sigma_{t,j}(u)} Q_j(u) + \sum_{k\in M} P_{i\to k}(u) \tag{4.3}$$

Earlier distributed self-shielding methods also simplified the source term of the fuel regions using the NR approximation. This approximation is problematic because it gives the same scattering source $Q_j(u)$ for different fuel regions. Although the scattering cross section at lethargy *u* could be same for different fuel regions at uniform temperature and fuel composition, the flux is strongly shielded in the fuel center in comparison to the fuel surface near large absorption resonances, resulting in different scattering sources along the fuel radius. Another approximation of the conventional treatment is assuming the total cross section to be spatially independent, i.e., $\Sigma_{t,j}(u) = \Sigma_{t,F}(u)$ for all *j*. This assumption is poor for at least two cases: depleted fuel and a non-uniform temperature profile. In the following derivation, both of these approximations are removed. The region-to-region collision probability $P_{i\to j}(u)$ is evaluated, but an approximation is introduced to save computing time.

Instead of directly calculating $P_{i\to j}(u)$, we calculate

$$\tilde{P}_{i\to j}(u) = P^{T_i,C_i}_{i\to j}(u)\frac{\sum_{j\in F} P_{i\to j}(u)}{\sum_{j\in F} P^{T_i,C_i}_{i\to j}(u)} = P^{T_i,C_i}_{i\to j}(u)\frac{1-P_{esc,i}(u)}{1-P^{T_i,C_i}_{esc,i}(u)} \tag{4.4}$$

As shown in Figure 4.1, $P^{T_i,C_i}_{i\to j}(u)$ is the first flight collision probability from region *i* to *j* assuming a uniform temperature T_i and material composition C_i throughout the whole fuel. In a media of uniform temperature and material composition, $P_{i\to j}$ can be easily tabulated by the total cross section levels. Thus, in the resonance calculation $P_{i\to j}^{T_i,C_i}(u)$ can be interpolated from the table rather than rigorous computation. It is straightforward to show that

$$\sum_{j\in F}\tilde{P}_{i\to j}(u)=\sum_{j\in F}P_{i\to j}(u) \tag{4.5}$$

Therefore, the escape probability $P_{esc,i}(u)$ of the realistic temperature profile and material composition is still conserved through the approximation. In addition, by summing the right hand side of Equation (4.2) over all subregion *i* of the fuel, it can be shown that the set of $\tilde{P}_{i\to j}(u)$ also conserves the total reaction rate R of the whole fuel rod

$$\begin{gathered} R=\sum_{j\in F}V_jQ_j(u)\sum_{i\in F}P_{j\to i}(u)+\sum_{i\in F}\sum_{k\in M}V_kP_{k\to i}(u)\Sigma_{p,k}= \\ \sum_{j\in F}V_jQ_j(u)\sum_{i\in F}\tilde{P}_{j\to i}(u)+\sum_{i\in F}\sum_{k\in M}V_kP_{k\to i}(u)\Sigma_{p,k}=\tilde{R} \end{gathered} \tag{4.6}$$

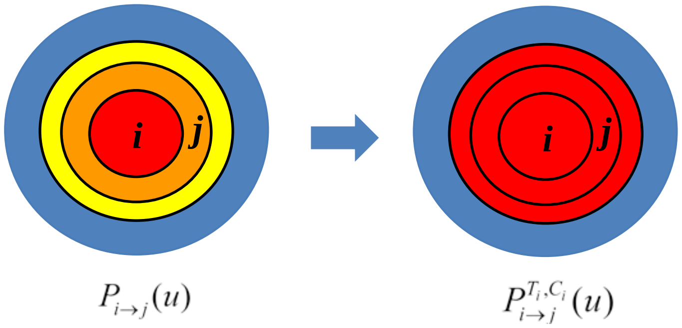

Figure 4.1 Configuration of computing $P_{i\to j}(u)$ and $P_{i\to j}^{T_i,C_i}(u)$
Left: realistic temperature distribution and material composition for evaluating $P_{i\to j}(u)$
Right: uniform temperature and material composition (temperature and material of subregion *i* are filled into the whole fuel) for evaluating $P_{i\to j}^{T_i,C_i}(u)$

Before proceeding, the validity of Equation (4.4) is further verified in a statistical manner. Obviously, Equation (4.4) is exact for the case of uniform temperature and material composition within the fuel rod. A non-uniform material composition comes into play when the fuel is depleted. The fact is that the fuel total cross section is dominated by U-238 so the radial variation of total cross section for a depleted fuel is usually smaller than that with non-uniform temperature where the microscopic cross section differs dramatically. Therefore, it should be sufficient to verify the collision probability approximation through a case of non-uniform fuel temperature. Specifically, given any subregion i, if the ratio $P_{i\to j}(u)\big/P_{i\to j}^{T_i,C_i}(u)$ for different j is almost a constant that equals to the ratio $\left(1-P_{esc,i}(u)\right)\big/\left(1-P_{esc,i}^{T_i,C_i}(u)\right)$, Equation (4.4) would be a good approximation of the true $P_{i\to j}(u)$. To show this, the fuel rod is subdivided into ten equal-volume rings and $P_{i\to j}(u)\big/P_{i\to j}^{T_i,C_i}(u)$ is plotted for all destination rings j with regard to a specified originating ring i in a range of total cross sections. These total cross sections are randomly chosen from a PWR pin cell case with a parabolic fuel temperature distribution (Average: 900K). Figure 4.2, Figure 4.3 and Figure 4.4 show the comparisons of $\left(1-P_{esc,i}(u)\right)\big/\left(1-P_{esc,i}^{T_i,C_i}(u)\right)$ with $P_{i\to j}(u)\big/P_{i\to j}^{T_i,C_i}(u)$ for $i=1$, 6 and 10, respectively. Note that Ring 1 locates in the fuel center while Ring 10 is near fuel surface.

The ring numbers in the legend are the destination ring j. The target ratio is calculated by $\left(1-P_{esc,1}(u)\right)\big/\left(1-P_{esc,1}^{T_1,C_1}(u)\right)$. The probability of $P_{i\to j}(u)$ or $P_{1\to j}^{T_1,C_1}(u)$ less than 2% is neglected in this plot since the low probabilities contribute little to the scattering source.

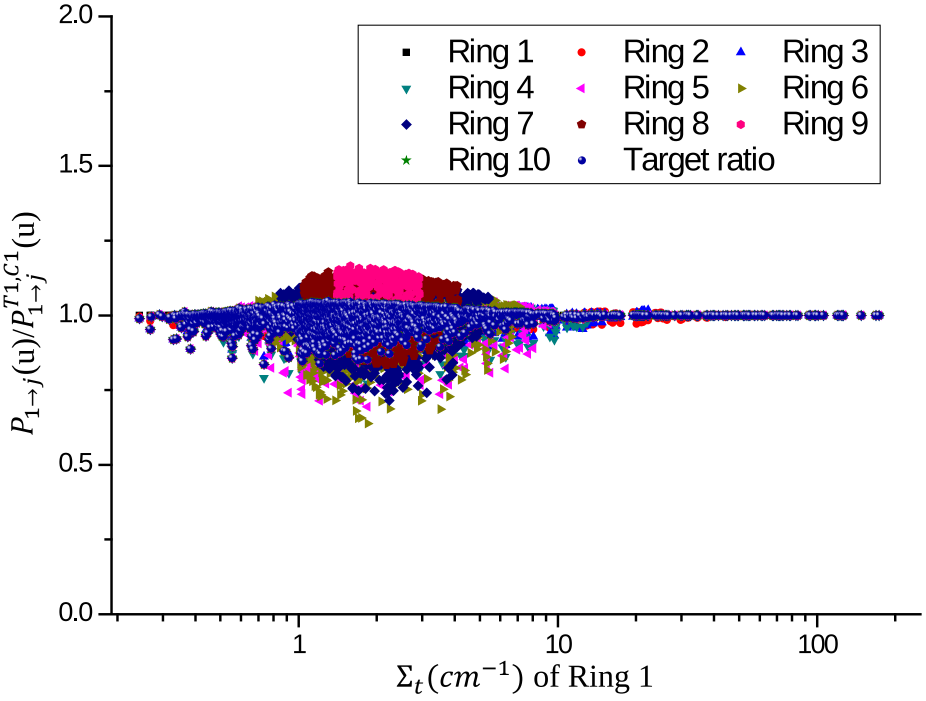

Figure 4.2 Comparison of $P_{1\to j}(u)\big/P_{1\to j}^{T_1,C_1}(u)$ with $\left(1-P_{esc,1}(u)\right)\big/\left(1-P_{esc,1}^{T_1,C_1}(u)\right)$.

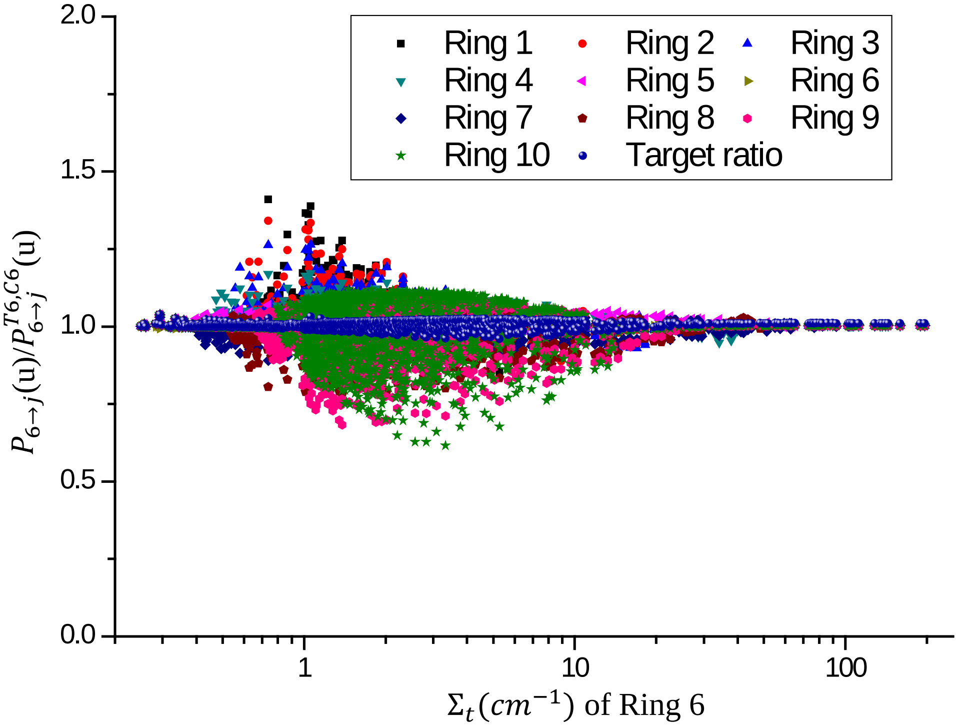

Figure 4.3 Comparison of $P_{6\to j}(u)/P^{T_6,C_6}_{6\to j}(u)$ with $\left(1-P_{esc,6}(u)\right)/\left(1-P^{T_6,C_6}_{esc,6}(u)\right)$

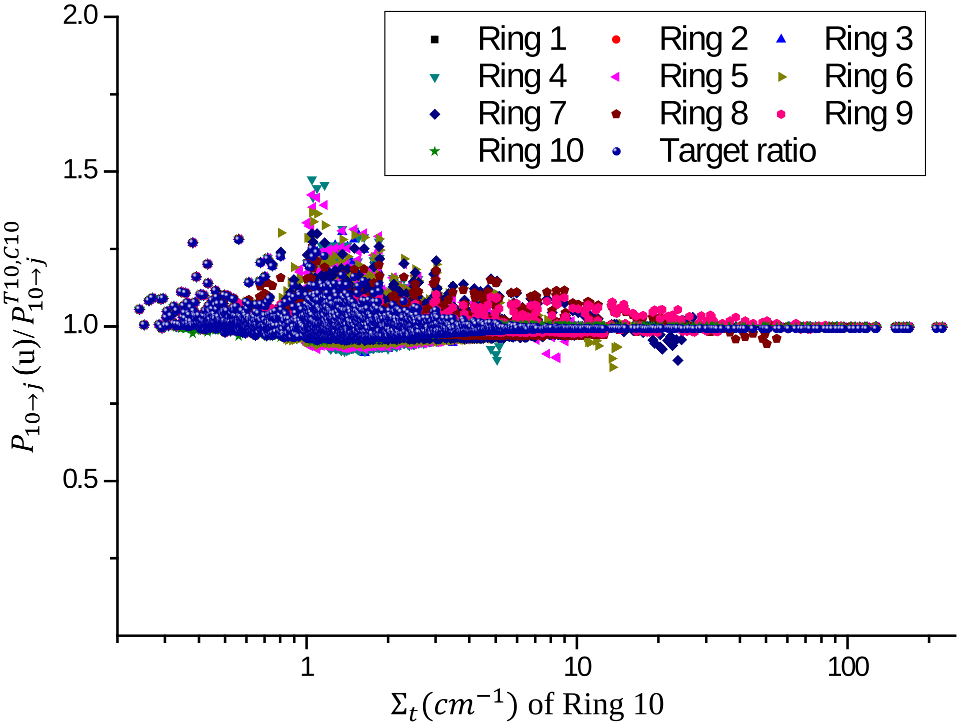

Figure 4.4 Comparison of $P_{10\to j}(u)/P^{T_{10},C_{10}}_{10\to j}(u)$ with $\left(1-P_{esc,10}(u)\right)/\left(1-P^{T_{10},C_{10}}_{esc,10}(u)\right)$

Ideally, $P_{i\to j}(u) \big/ P_{i\to j}^{T_i,C_i}(u)$ of different *j* are expected to be overlapped with the target ratio $\left(1-P_{esc,i}(u)\right)\big/\left(1-P_{esc,i}^{T_i,C_i}(u)\right)$ at every total cross section value. Of our interest, $P_{i\to j}(u)$ in Equation (4.3) are used as weights of $Q_j(u)\big/\Sigma_{t,j}(u)$ to evaluate the flux. These weights are only important when the variation of $Q_j(u)\big/\Sigma_{t,j}(u)$ along the fuel radius is large. Otherwise, Equation (4.5) guarantees the accuracy of the flux evaluation for a nearly flat $Q_j(u)\big/\Sigma_{t,j}(u)$. It is reasonable to assume that large spatial variations of $Q_j(u)\big/\Sigma_{t,j}(u)$ only happen near the resonance, either due to the variation of temperature dependent $\Sigma_{t,j}(u)$, or due to the spatially shielded $Q_j(u)$. Moreover, it is within the resonances that the accuracy of the energy dependent flux is more important. In Figure 4.2-Figure 4.4, $P_{i\to j}(u) \big/ P_{i\to j}^{T_i,C_i}(u)$ are more consistent with $\left(1-P_{esc,i}(u)\right)\big/\left(1-P_{esc,i}^{T_i,C_i}(u)\right)$ when $\Sigma_{t,j}(u)$ is large. Therefore, the approximation in Equation (4.4) favors more accurate results in the energy range of resonances. The neutron spectra of the same PWR fuel pin of parabolic fuel temperature distribution with infinite coolant are computed using $\tilde{P}_{i\to j}(u)$ and the exact $P_{i\to j}(u)$. Figure 4.5 compares the neutron spectra of four typical energy ranges with U-238 resonances. The results calculated by approximate $\tilde{P}_{i\to j}(u)$ and exact $P_{i\to j}(u)$ agree well with each other.

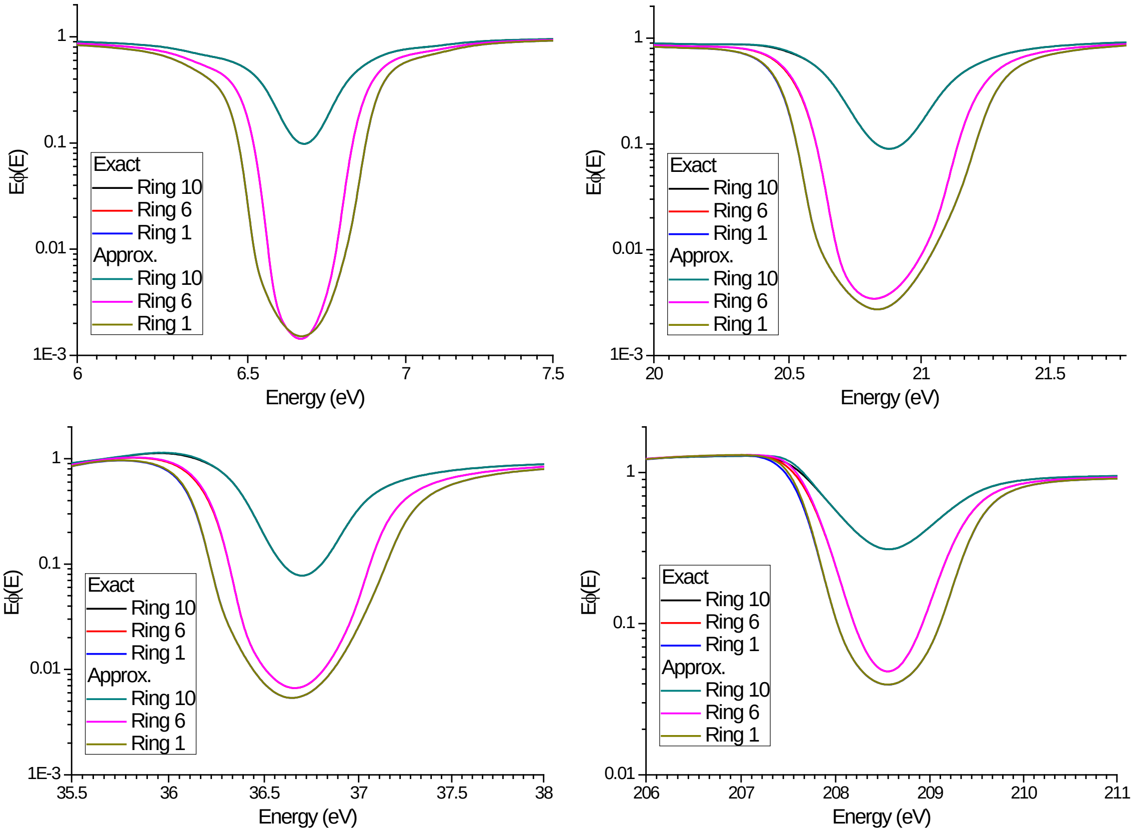

Figure 4.5 Spectra of exact and approximate $P_{i\to j}(u)$ for a non-uniform fuel temperature case

Based on the previous discussion, we are ready to replace $P_{i\to j}(u)$ in Equation (4.3) with $\tilde{\boldsymbol{P}}_{\boldsymbol{i\to j}}(\boldsymbol{u})$, which leads to the following expression for the flux

$$\phi_i(u) \approx \frac{1-P_{esc,i}(u)}{1-P_{esc,i}^{T_i,C_i}(u)} \sum_{j\in F} \frac{P_{i\to j}^{T_i,C_i}(u)}{\Sigma_{t,j}(u)} Q_j(u) + \sum_{k\in M} P_{i\to k}(u) \tag{4.7}$$

By defining $\bar{Q}_i(u) = \dfrac{\Sigma_{t,i}(u)}{1-P_{esc,i}^{T_i,C_i}(u)} \sum_{j\in F} \dfrac{P_{i\to j}^{T_i,C_i}(u)}{\Sigma_{t,j}(u)} Q_j(u)$ and replacing $\sum_{k\in M} P_{i\to k}(u)$ with $P_{esc,i}(u)$,

$$\phi_i(u) = \frac{\bar{Q}_i(u)}{\Sigma_{t,i}(u)}\left[1-P_{esc,i}(u)\right] + P_{esc,i}(u) \tag{4.8}$$

Using the rational form of $P_{esc,i}(u)=\dfrac{\Sigma_{e,i}(u)}{\Sigma_{t,i}(u)+\Sigma_{e,i}(u)}$ where $\Sigma_{e,i}(u)$ should be energy dependent, the equation can be transformed into a form similar to the conventional equivalence theory

$$\phi_i(u)=\frac{\bar{Q}_i(u)+\Sigma_{e,i}(u)}{\Sigma_{t,i}(u)+\Sigma_{e,i}(u)} \tag{4.9}$$

Therefore, the quasi-1D slowing-down equation is defined as

$$\left[\Sigma_{t,i}(u)+\Sigma_{e,i}(u)\right]\phi_i(u)=\bar{Q}_i(u)+\Sigma_{e,i}(u) \tag{4.10}$$

This equation is actually in a 0-D form but 1-D information is embedded in $\bar{Q}_i(u)$ and $\Sigma_{e,i}(u)$. Determination of $\bar{Q}_i(u)$ includes two quantities, $Q_j(u)$ and $P_{i\to j}^{T_i,C_i}(u)$. Evaluation of $Q_j(u)$ is similar to the conventional slowing-down calculation. A detailed description for an efficient evaluation method for $Q_j(u)$ has been described in Chapter 2. A practical energy mesh scheme based on the problem-dependent mesh is described in Appendix B. The first flight collision probability is evaluated using the Carlvik method (see Appendix A) for the 1-D cylindrical geometry. A table of $P_{i\to j}$ versus total cross section is established before the resonance calculation for $P_{i\to j}^{T_i,C_i}(u)$ interpolation. Usually, 1000-2000 cross section points are sufficient to generate an accurate $P_{i\to j}$ table so the additional computing time is negligible.

In addition to $\bar{Q}_i(u)$, $\Sigma_{e,i}(u)$ is determined by rigorously evaluating $P_{esc,i}(u)$ using the realistic fuel temperature profile and material compositions in the 1-D cylindrical geometry (see Appendix A). To incorporate the inter-pin shielding effect into $\Sigma_{e,i}(u)$, a straightforward approach could be to evaluate the equivalence cross section with a 1-D cylindrical pin in an infinite coolant and then modify it using the realistic Dancoff effect from an ESSM calculation. Specifically, the CE equivalence cross section for an infinite coolant is modified as

$$\Sigma_{e,i}(u) \approx \Sigma_{e,i}^{\inf}(u)\frac{\Sigma_{e,F,g}^{ESSM}}{\Sigma_{e,F,g}^{\inf}} \qquad (u_{g-1} < u < u_g) \tag{4.11}$$

In this equation, $\Sigma_{e,i}^{\inf}(u)$ is the equivalence cross section of subregion *i* evaluated using Carlvik method in 1-D cylindrical geometry with infinite coolant. $\Sigma_{e,F,g}^{ESSM}$ is the realistic equivalence cross section of the single fuel region obtained from ESSM. $\Sigma_{e,F,g}^{\inf}$ is the equivalence cross section of the single fuel region in 1-D cylindrical geometry with infinite coolant, calculated by the group-wise total cross section. To compute $\Sigma_{e,F,g}^{\inf}$, a few iterations are required between calculation of Carlvik equivalence cross section and interpolation from the RI tables. An alternative approach of using Equation (4.11) could be to compute the ratio of the fuel escape probability in the realistic lattice to the one in the infinite coolant, i.e.,

$$R_{F,g} = \frac{P_{e,F,g}^{ESSM}}{P_{e,F,g}^{\inf}} = \frac{\Sigma_{e,F,g}^{ESSM} \Big/ \left(\Sigma_{t,F,g}^{ESSM} + \Sigma_{e,F,g}^{ESSM}\right)}{\Sigma_{e,F,g}^{\inf} \Big/ \left(\Sigma_{t,F,g}^{\inf} + \Sigma_{e,F,g}^{\inf}\right)} \tag{4.12}$$

This ratio is in turn used to modify $P_{esc,i}^{\inf}(u)$ to obtain $P_{esc,i}(u)$ and thus $\Sigma_{e,i}(u)$. Both approaches assume that the Dancoff effect is not dependent on energy so that the group-averaged factors are used for every point within each energy group. Although the second approach is conventionally used in Ref. [44,45], numerical experiments give slightly better results when the equivalence cross section is directly modified as in Equation (4.11). Therefore, the first approach is chosen for the quasi-1D model.

4.3 Description of the Method

The basic idea of the correction based self-shielding method for annular fuel regions is to compute the shielded cross sections by ESSM iteration with single mesh fuel region, and correct for the multi-region effects by using factors obtained from the quasi-1D slowing-down calculation.. The resonance interference and non-uniform temperature effects are also modeled in a similar way. The method is summarized as follows:

Step 1. Perform ESSM using a volume-averaged fuel temperature $\overline{T}$ and volume-averaged material composition $\overline{C}$ for a single fuel region neglecting resonance interference. This step generates a set of shielded cross sections $\sigma_{iso,x,g,F}^{non-\mathrm{intf}}(\overline{T},\overline{C})$ for isotope *iso*, energy group *g* and reaction channel *x*. These baseline cross sections incorporate the inter-pin shielding effect (Dancoff effect) but not intra-pin effects or resonance interference.

Step 2. Resolve the intra-pin and resonance interference effects by solving the quasi-1D slowing-down equation, Equation (4.10) for two sets of problems:

a. For the fuel mixture for each subregion *i* of the fuel and realistic temperature distribution T_i and material composition C_i, compute shielded cross sections $\tilde{\sigma}_{iso,x,g,i}^{\mathrm{intf}}(T_i,C_i)$;

b. For each isolated isotope with single fuel region using uniform temperature $\overline{T}$ and material composition $\overline{C}$ (conditions similar to Step 1), compute shielded cross sections $\tilde{\sigma}_{iso,x,g,F}^{non-\mathrm{intf}}(\overline{T},\overline{C})$.

In Step 2, substep **a** accounts for the intra-pin effects and resonance interference, while substep **b** performs a baseline calculation. The global Dancoff effect has been incorporated into these quasi-1D slowing-down calculations via the approximation of Equation (4.11). To minimize the approximation error, instead of using the effective cross sections from substep **a** as the final results, correction factors are computed by comparing the effective cross sections of substeps **a** and **b**, and are used to correct the baseline results from Step 1. Therefore, the resultant shielded cross section is given as

$$\sigma_{iso,x,g,i}^{final}(T_i,C_i)=\sigma_{iso,x,g,F}^{non-\mathrm{intf}}(\overline{T},\overline{C})\frac{\tilde{\sigma}_{iso,x,g,i}^{\mathrm{intf}}(T_i,C_i)}{\tilde{\sigma}_{iso,x,g,F}^{non-\mathrm{intf}}(\overline{T},\overline{C})} \tag{4.13}$$

Applying Equation (4.13) to the 1-D cross section such as absorption, fission, total scattering etc., is straightforward. Since the 2-D multigroup scattering cross sections are processed with an infinitely dilute flux spectrum, those data also require shielding calculation. Assuming that the original secondary energy distribution of scattering is preserved in spite of the self-shielding effect, the scattering matrices can be normalized by the shielded 1-D scattering cross section,

$$\sigma_{iso,s,l,g->g'}^{shielded} = \frac{\sigma_{iso,s,0,g}^{shielded}}{\sigma_{iso,s,0,g}^{unshielded}} \sigma_{iso,s,l,g->g'}^{unshielded} \tag{4.14}$$

where $\sigma_{iso,s,l,g->g'}$ is the l_{th}-order Legendre moment of scattering cross section from group *g* to *g'* and $\sigma_{iso,s,0,g}$ is the zero-order scattering cross section of group *g*. We note that the matrix elements for the higher order ($\geq P_1$) moments are multiplied by the same factors as the zero-order terms, so that changes to the angular distribution due to self-shielding are treated approximately.

The additional computation cost of the correction method compared to the conventional ESSM is due to solving the quasi-1D slowing-down equation. Substep **a** in Step 2 requires a single slowing-down sweep for all the subregions of the fuel, while substep **b** requires independent slowing-down sweeps for every resonance isotope of the fuel to exclude the interference effect. The computing condition of substep **b** is similar to Step 1, except that the quasi-1D slowing-down model is used rather than the ESSM model. Therefore, by analogy with the heterogeneous RI tables for ESSM, a second set of heterogeneous RI tables is pre-computed using the quasi-1D slowing-down model and also parameterized by the background cross section. With the second set of RI tables, the slowing-down calculation of substep **b** in Step 2 can be substituted by table interpolation.

Surprisingly, another benefit is automatically gained when the second set of heterogeneous RI tables is used in the calculation of substep **b**. As discussed earlier, the ESSM calculation in Step 1 introduces a bias on $\Sigma_{e,F,g}^{ESSM}$ and hence a bias on the shielded cross section $\sigma_{iso,x,g,F}^{non-\text{intf}}(\overline{T},\overline{C})$ because of combining all the resonance isotopes as a whole absorber. However, since the biased $\Sigma_{e,F,g}^{ESSM}$ is also used in substep **b** for interpolation of $\tilde{\sigma}_{iso,x,g,F}^{non-\text{intf}}(\overline{T},\overline{C})$, the error introduced by this simplification is cancelled out to some extent because $\sigma_{iso,x,g,F}^{non-\text{intf}}(\overline{T},\overline{C})$ and $\tilde{\sigma}_{iso,x,g,F}^{non-\text{intf}}(\overline{T},\overline{C})$ are both monotonically increasing functions of the background cross section.

Chapter 5

Numerical Verifications

In order to test the proposed resonance method, a set of benchmarking problems is created. The verification code and cross section data are briefly discussed. The results of several resonance self-shielding methods are compared against Monte Carlo reference solutions. Azimuthal dependent self-shielding is also investigated based on a straightforward extension of these resonance methods.

5.1 Benchmarking Problem Set for Resonance Self-shielding

This benchmarking problem set consists of three groups of problems. The first group includes ten 2-D uniform infinite lattice problems of pin cell configurations, which are chosen to test the capability of the resonance method for treating distributed self-shielding, resonance interference and non-uniform temperature effect. The second group of problems has five 2-D non-uniform lattice problems with 5 by 5 pin cell configurations. The pin cells are chosen to be non-uniform in order to test the heterogeneous effect on resonance calculation. UO2 with mixed abundances, MOX, control rod, water hole and gadolinium bearing fuels are introduced into this group of problems. In the third group, two assembly problems are performed to confirm the accuracy of the new method for realistic reactor core applications. Table 5-1 summarizes the basic information of the problem set.

Table 5-1 Information of the benchmarking problem set

Group 1 Uniform lattice of pin cell		
#	Case ID	Description
1	UO2_600K	5% UO2 pin cell with uniform fuel Temp. of 600K
2	UO2_900K	5% UO2 pin cell with uniform fuel Temp. of 900K
3	UO2_1200K	5% UO2 pin cell with uniform fuel Temp. of 1200K

4	UO2_para900K	5% UO2 pin cell with parabolic fuel Temp. of Ave. 900K
5	UO2_para1200K	5% UO2 pin cell with parabolic fuel Temp. of Ave. 1200K
6	UO2_3%	3% UO2 pin cell
7	UO2_4%	4% UO2 pin cell
8	UO2_Gd	Gadolinium integrated UO2 fuel
9	MOX_16%	MOX fuel with 16% Plutonium
10	UO2_Burn	Deplete UO2 to 30GWd/tU
Group 2 Non-uniform lattice problems (5×5 pin cells)		
#	Case ID	Description
11	UO2_water	UO2 pin cells with water hole in center
12	UO2_AIC	UO2 pin cells with AgInCd control rod in center
13	UO2_UO2+Gd	UO2 pin cells with center pin of Gadolinium integrated
14	UO2_3%+5%	Mixed pin cells of 3% and 5% UO2
15	UO2_MOX	Mixed pin cells of UO2 and MOX (16%) fuels
Group 3 Fuel assembly problems		
#	Case ID	Description
16	UO2_Assembly	Typical 17×17 type UO2 assembly with water gap
17	MOX_Assembly	17×17 zoned MOX assembly (4.5%/3.0%/2.5%) with water gap

The geometry parameters of the fuel pin are identical for different fuel types, which are adapted from the CASL AMA benchmark problem [50]. Basic geometry information is summarized in Table 5-2. The material compositions are given in Table 5-3. If not specified, all the temperatures of materials are 600K.

Table 5-2 Geometry description

Fuel Pin	
Pellet Radius	0.4096 cm
Inner Clad Radius	0.418 cm
Outer Clad Radius	0.475 cm
Pitch	1.26 cm
Control Rod	
Poison Radius	0.382 cm
Inner Clad Radius	0.386 cm
Outer Clad Radius	0.484 cm
Assembly water gap	0.04cm

Table 5-3 Material compositions

Material	**Isotope**	**Atomic number density (/barn/cm)**
UO2 (5%)	92235	1.23756E-03
	92238	2.32172E-02
	8016	4.89096E-02
UO2 (4%)	92235	0.97819E-03
	92238	2.34765E-02
	8016	4.89096E-02
UO2 (3%)	92235	0.73364E-03
	92238	2.37211E-02
	8016	4.89096E-02
Gap	8016	2.68714E-05
Cladding	40090	2.18865E-02
	40091	4.77292E-03
	40092	7.29551E-03
	40094	7.39335E-03
	40096	1.19110E-03
Moderator (600K)	8016	2.20729E-02
	1001	4.41459E-02
Gadolinia UO2 fuel (5% Gd)	92234	3.18096E-06
	92235	3.90500E-04
	92236	1.79300E-06
	92238	2.10299E-02
	64152	3.35960E-06
	64154	3.66190E-05
	64155	2.48606E-04
	64156	3.43849E-04
	64157	2.62884E-04
	64158	4.17255E-04
	64160	3.67198E-04
	8016	4.53705E-02
MOX (16% Pu)	92235	3.88790E-05
	92238	1.91591E-02
	8016	4.63302E-02
	94238	8.39859E-05
	94239	2.17061E-03
	94240	9.91540E-04
	94241	3.67320E-04
	94242	2.51738E-04
	95241	1.06640E-04
AIC control rod	47107	2.36159E-02
	47109	2.19403E-02

	48110	3.41250E-04
	48111	3.49720E-04
	48112	6.59276E-04
	48113	3.33873E-04
	48114	7.84957E-04
	49113	3.44262E-04
	49115	7.68050E-03
Cladding of control rod	6000	3.20895E-04
	14028	1.58197E-03
	14029	8.03653E-05
	14030	5.30394E-05
	15031	6.99938E-05
	24050	7.64915E-04
	24052	1.47506E-02
	24053	1.67260E-03
	24054	4.16346E-04
	25055	1.75387E-03
	26054	3.44776E-03
	26056	5.41225E-02
	26057	1.24992E-03
	26058	1.66342E-04
	28058	5.30854E-03
	28060	2.04484E-03
	28061	8.88879E-05
	28062	2.83413E-04
	28064	7.21770E-05
MOX (2.5%)	92235	4.58000E-05
	92238	2.25591E-02
	94238	1.22581E-05
	94239	3.16760E-04
	94240	1.44698E-04
	94241	5.35982E-05
	94242	3.67355E-05
	95241	1.55637E-05
	8016	4.63690E-02
MOX (3.0%)	92235	4.55651E-05
	92238	2.24434E-02
	94238	1.47097E-05
	94239	3.80112E-04
	94240	1.73637E-04
	94241	6.43178E-05
	94242	4.40826E-05
	95241	1.86765E-05

	8016	4.63690E-02
MOX (4.5%)	92235	4.48605E-05
	92238	2.20964E-02
	94238	2.20646E-05
	94239	5.70168E-04
	94240	2.60456E-04
	94241	9.64768E-05
	94242	6.61238E-05
	95241	2.80147E-05
	8016	4.63690E-02

The fuel rod is subdivided into 10 equal-volume rings for all the cases. The pin cell problems in Group 1 are computed with reflective boundaries to form an infinite uniform lattice. The geometrical configurations of problems in Group 2 are shown in Figure 5.1 and Figure 5.2. For Cases 11-13, the center pin materials are varied. Cases 14 and 15 are checkerboard layouts with mixed fuel types. In Group 3, two assembly problems are tested as shown in Figure 5.3: (1) a typical Westinghouse 17×17 type fuel assembly with fresh 5% UO_2 and (2) the same assembly with zoned MOX fuel.

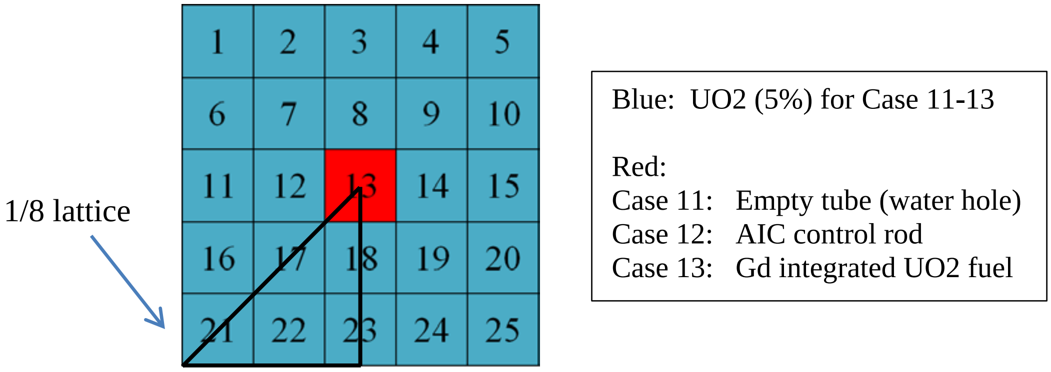

Figure 5.1 Pin layout of Case 11, 12 and 13

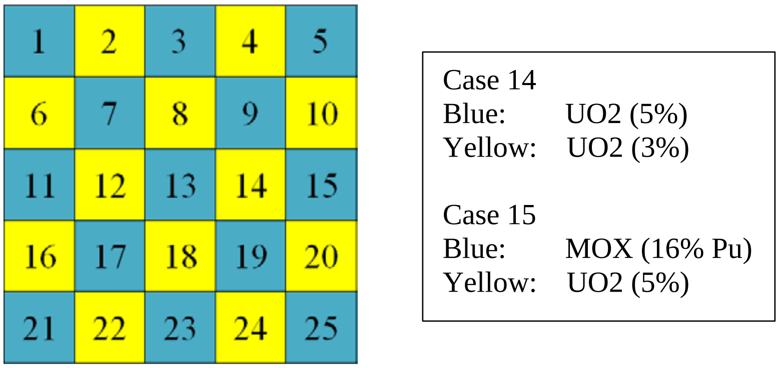

Case 14
Blue: UO2 (5%)
Yellow: UO2 (3%)

Case 15
Blue: MOX (16% Pu)
Yellow: UO2 (5%)

Figure 5.2 Pin layout of Case 14 and 15

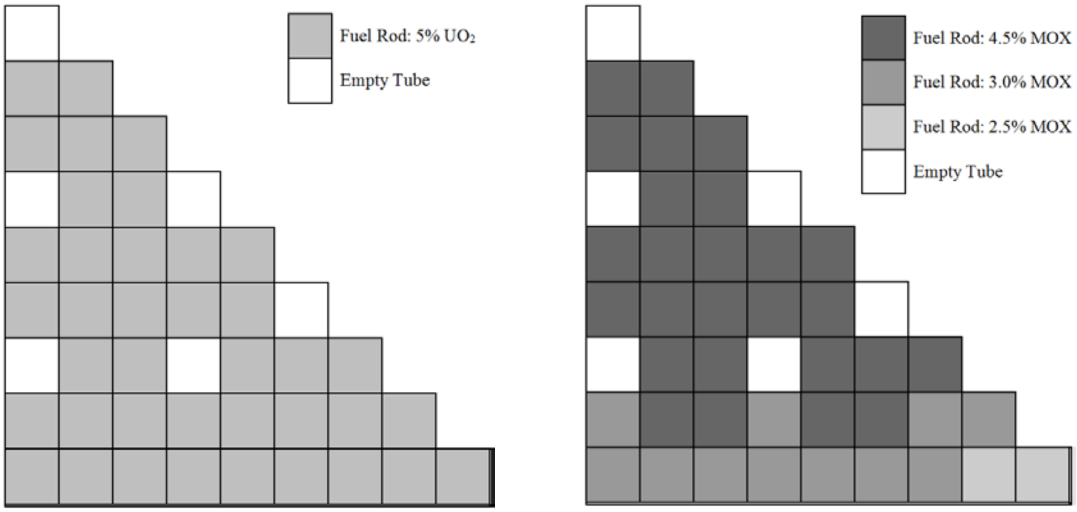

Figure 5.3 Configurations of UO_2 and MOX Assembly (1/8 assembly)

5.2 Computing Codes and Cross Section Libraries

The proposed resonance self-shielding method has been implemented and tested in the direct whole core neutron transport code DeCART [51]. In comparison to the conventional 2-step (transport/diffusion) methodology where the first step is the generation of homogenized few group cross sections with a transport method and the second step is a global calculation with a diffusion method, DeCART performs a direct transport calculation (2-D planar transport plus 1-D axial diffusion) using the realistic geometry, material composition and temperature profile of the reactor configuration and the number of energy groups may be as large as the number used for the lattice calculation in the 2-step transport/diffusion method. The resonance self-shielding calculations are performed for every 2-D plane and the multigroup self-shielded cross sections are directly used in the whole core transport calculation without homogenization. Both the whole core transport calculation and the fixed source resonance calculations are performed with MOC.

In the original version, DeCART utilized the subgroup method for resonance calculation. In order to incorporate the new self-shielding method, two modules are added to the DeCART code system, i.e., ESSM and the correction factor generator. The ESSM is implemented in addition to the subgroup method to resolve the inter-pin shielding effect (Step 1 in Section 4.3). The correction factor generator incorporates the quasi-1D slowing-down solver to produce the correction factors accounting for the intra-pin self-shielding details and resonance interference (Step 2 in Section 4.3). The collision probability kernel is embedded in the slowing-down solver to provide the CE dependent equivalence cross sections. Once the ESSM iteration is converged, the module passes the group-wise equivalence cross sections to the correction factor generator for Dancoff adjustment. The correction factors are then fed to the ESSM module to correct the self-shielded cross sections. In addition, the ESSM module is able to work in standalone mode identical to conventional ESSM.

Figure 5.4 depicts the data flow of the verification code system. The CE library is taken from SCALE 6.0 package [52] and the multigroup library is provided by Oak Ridge National Laboratory for use in the CASL project. They are both processed by AMPX [53] from the raw nuclear data of ENDF/B-VII.0 [54]. The CE data are employed when solving the slowing-down equations for the calculation of correction factors. The multigroup library structure consists of a total of 56 energy groups, in which 25 groups are defined as resonance groups (0.6eV-25keV). It has been mentioned that two sets of heterogeneous RI tables are generated. RI table Set 1 is processed by SCALE-CENTRM and AMPX-IRFfactor modules by performing the 2-D heterogeneous slowing-down calculation for the resonance isotopes. This RI table set is loaded into the multigroup library for ESSM iteration. RI table Set 2 is generated by performing the quasi-1D slowing-down calculation and is used for efficient interpolation of the shielded cross section in Step 2-b of Section 4.3. The subgroup parameters are also provided in the 56-

group library, which are generated by the physical probability table approach and are consistent with RI table Set 1.

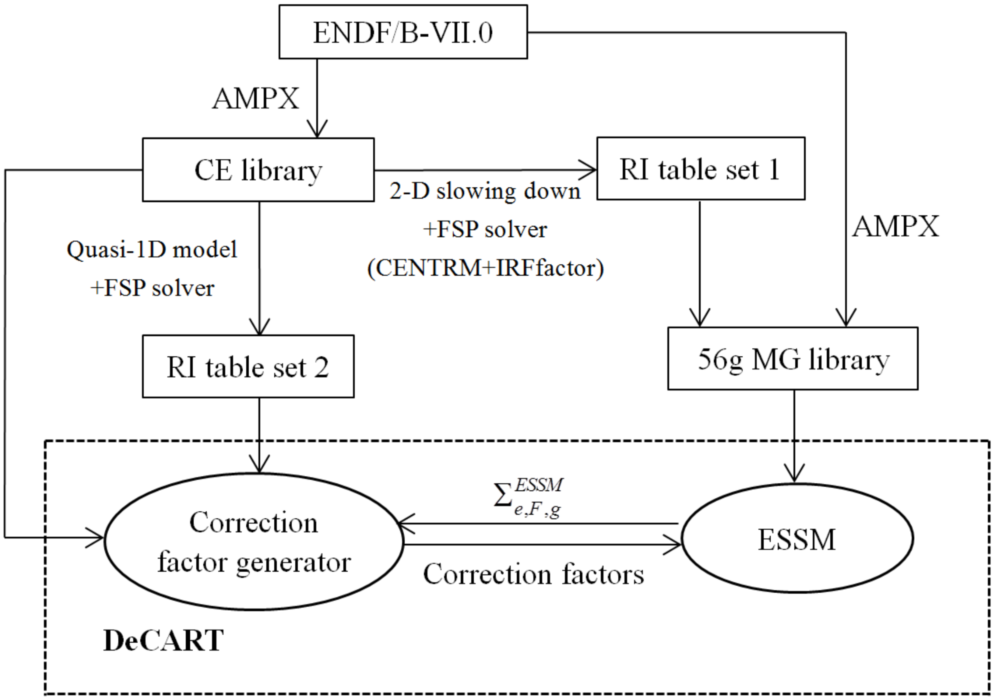

Figure 5.4 Data flow of the resonance self-shielding model

The MCNP5 code [55] is used to generate reference shielded cross sections for comparison with the new method. In order to produce CE libraries for MCNP use, a series of NJOY [56] modules are run to generate the ACE format data for every specific temperature appearing in the test problems. All the ACE data are prepared from ENDF/B-VII.0, which is the same source as the verification code system.

5.3 Results and Discussions

The benchmarking problems presented in Section 5.1 are run by the subgroup method, ESSM and ESSM-X of DeCART. Here the term ‘ESSM’ refers to the conventional embedded self-shielding method and ESSM-X refers to the proposed new method. The same spatial discretization and MOC ray options (4 polar angles, 24 azimuthal angles in 90^{o} and .01cm ray spacing) are applied to all the test problems. The ESSM and the subgroup method use Bondarenko iteration (see Section 3.4.1) for treatment of resonance interference. The weight adjustment for non-uniform temperature distribution has also been implemented in the subgroup method (see Section 3.4.3). The MCNP reference solution is calculated with 600 active cycles and 50,000 histories/(cycle·pin cell) to make a total of 30 million neutron histories per pin cell. As a result, the standard deviation of reaction rates for every reaction channel and every resonance energy group is below 1%, and the standard deviations of reaction rates over the resonance energy range (0.625eV-25keV) for important resonance isotopes (U-235, U-238, Pu-239 and Pu-240) are on the order of 0.02%. The results of the three groups of benchmarking problems are discussed in the following subsections, respectively.

5.3.1 Uniform Infinite Lattice

Of the ten pin cell problems (see Section 5.1), the first nine are steady state eigenvalue problems developed to verify the accuracy of the resonance self-shielding method for infinite fuel lattice. Case 10 investigates a depletion case to demonstrate how the distributed self-shielding model could affect the radially dependent isotopic concentrations during fuel burnup. First we verify the effective cross section, which is the direct product from the resonance calculation. Table 5-4 compares the radially dependent shielded cross sections for U-238 in Group 34 (6.5eV-6.88eV) for the three methods with MCNP. Since this is the major resonance of U-238, strong spatial self-shielding is seen from the reference solution, e.g., the shielded cross section for the outermost ring is almost three times that for the innermost ring for Case 1. It is important to note that the shielded cross section of Group 34 is not monotonically increasing from the fuel center to the surface for the uniform temperature cases. The values become a bit larger towards the center for the innermost four or five rings. This can be explained by comparing the CE fluxes of every fuel ring, in which the fluxes of the inner rings are relatively flatter about energy than those of the middle rings due to the strong spatial shielding. The relative errors show that ESSM is unable to correctly produce the spatially shielded cross sections. For all the five cases, it underestimates the cross sections of the surface ring and overestimates those of the inner rings. Compared to ESSM, the subgroup method performs better for the surface ring, but still, has large discrepancies for the inner rings. The shielded cross sections generated by ESSM-X compare favorably with MCNP results, showing an order of magnitude smaller relative error compared to the ESSM and subgroup method. The agreement of non-uniform temperature cases is on the same order as the agreement with the uniform temperature cases, indicating the effectiveness of the collision probability approximation in Equation (4.4). The agreement of other resonance groups is similar to Group 34 and thus the results are not repeated.

Table 5-4 Comparison of spatially shielded U-238 absorption cross sections for Group 34 (6.5eV-6.88eV) with MCNP showing effect of radial fuel regions

Case		Ring number									
		1	2	3	4	5	6	7	8	9	10
1 (UO2_600K)	Ref. XS	415.1	407.3	390.2	380.5	376.0	374.0	386.0	423.0	541.3	1206.9
	Subgroup	28.4	30.2	34.9	37.0	36.9	35.1	27.9	14.9	-4.5	-16.4
	ESSM	46.7	50.9	57.7	61.7	64.8	69.8	67.7	57.3	29.2	-34.0
	ESSM-X	-2.9	-4.1	-2.6	-2.2	-2.0	-0.9	-0.4	-0.2	0.2	-1.9
2 (UO2_900K)	Ref. XS	688.9	662.8	634.0	606.2	578.1	565.9	566.8	610.9	769.4	1453.5
	Subgroup	22.6	27.0	32.0	36.6	40.7	39.7	34.2	20.2	-0.4	-10.2
	ESSM	30.2	35.6	42.3	49.5	56.5	60.7	64.8	56.4	27.8	-25.0
	ESSM-X	-3.0	-3.8	-4.0	-3.9	-2.8	-2.6	-1.4	-0.9	-0.1	-1.7
3 (UO2_1200K)	Ref. XS	1011.1	980.3	933.2	877.8	827.9	785.9	770.0	808.1	986.4	1616.6
	Subgroup	15.3	18.7	24.2	30.7	35.8	38.2	34.2	21.6	1.9	-6.0
	ESSM	15.4	19.0	25.2	33.5	41.6	49.0	53.9	49.9	25.1	-17.9
	ESSM-X	-3.3	-4.5	-4.8	-4.3	-3.9	-3.0	-2.1	-0.9	0.2	-1.4
4 (UO2_para900K)	Ref. XS	892.2	791.8	712.2	632.5	577.6	538.0	513.8	519.9	612.4	1250.8
	Subgroup	-19.3	-5.9	9.2	28.2	43.0	49.0	48.7	37.1	13.9	-10.6
	ESSM	27.4	36.3	44.3	54.1	61.0	64.9	62.6	53.1	27.0	-34.3
	ESSM-X	-2.9	-2.3	-2.9	-1.5	-1.6	-1.3	0.0	0.7	0.7	-2.5
5 (UO2_para1200K)	Ref. XS	1200.9	1092.8	987.6	882.8	804.6	740.4	701.6	706.8	833.5	1481.8
	Subgroup	-8.4	2.1	14.0	27.7	38.5	46.4	46.7	37.3	17.3	-4.8
	ESSM	5.1	13.5	23.7	36.4	46.8	54.4	58.2	52.3	26.5	-24.9
	ESSM-X	-5.9	-4.9	-4.3	-3.0	-3.0	-2.5	-1.8	-0.8	-0.1	-2.1
6 (UO2_3%)	Ref. XS	421.5	401.9	391.7	381.4	375.7	376.1	386.1	421.7	538.0	1202.5
	Subgroup	26.3	31.7	34.2	36.5	36.8	34.2	27.7	15.0	-4.6	-16.6
	ESSM	42.2	50.4	56.8	61.2	64.3	67.4	67.0	57.3	29.3	-34.0
	ESSM-X	-3.9	-2.5	-2.7	-2.3	-1.9	-1.6	-0.9	-0.6	-0.2	-2.0
7 (UO2_4%)	Ref. XS	415.0	405.2	391.5	382.9	377.8	373.2	386.7	423.3	538.5	1209.0
	Subgroup	28.4	30.8	34.4	36.1	36.1	35.3	27.6	14.7	-4.4	-16.9
	ESSM	45.5	50.4	57.3	60.6	63.6	69.4	67.0	56.9	29.5	-34.2
	ESSM-X	-2.7	-3.4	-2.8	-2.7	-2.5	-0.7	-0.8	-0.6	0.2	-2.3
8 (UO2_Gd)	Ref. XS	402.5	389.5	379.7	371.4	375.6	375.4	393.4	434.8	567.3	1237.1
	Subgroup	31.2	34.8	37.2	38.7	35.3	32.9	24.3	11.7	-6.6	-16.4
	ESSM	52.9	57.9	62.1	66.6	67.3	70.9	67.4	55.0	24.5	-34.8
	ESSM-X	-3.6	-2.9	-2.4	-1.5	-2.7	-1.0	-1.0	-0.2	0.0	-2.3
9 (MOX_16%)	Ref. XS	389.5	388.8	377.9	375.1	375.1	379.9	403.5	450.8	600.1	1272.3
	Subgroup	37.6	37.0	39.7	39.1	37.1	32.9	23.0	10.1	-8.1	-16.2
	ESSM	62.4	63.6	69.7	71.2	72.7	74.2	65.4	51.7	20.0	-35.1
	ESSM-X	-3.5	-5.3	-3.9	-3.6	-2.8	-1.5	-1.5	-0.3	-0.4	-2.4

The MCNP reference cross sections are shown in barns and the entries for the other methods are the relative errors in %.

Table 5-5 shows the spatially dependent absorption cross sections of U-235 for Group 22 (116.0eV-117.5eV) where the resonance interference due to U-238 is significant.

Because the spectra are dominated by U-238 absorption resonances, the usual shielding behavior where the effective cross section tends to the peak at the fuel surface is not seen in this group for U-235. ESSM and the subgroup method using Bondarenko iteration fail to model the resonance interference, so large discrepancies are observed across all the rings of the fuel rod. It is clear from Table 5-5 that errors of shielded cross sections are reduced to less than 1% for most subregions with ESSM-X, indicating the success of employing CE cross sections explicitly for interference correction.

Table 5-5 Comparison of spatially dependent U-235 absorption cross sections for Group 22 (116.0eV-117.5eV) with MCNP showing effect of resonance interference

Case		Ring number									
		1	2	3	4	5	6	7	8	9	10
1 (UO2_600K)	Ref. XS	42.3	42.0	41.6	41.2	40.7	40.0	39.2	37.9	36.1	32.6
	Subgroup	-49.3	-49.0	-48.5	-48.0	-47.3	-46.5	-45.3	-43.5	-40.6	-34.0
	ESSM	-49.3	-49.0	-48.5	-48.0	-47.3	-46.4	-45.3	-43.4	-40.5	-34.2
	ESSM-X	-0.1	-0.2	-0.1	0.0	0.0	0.0	-0.2	-0.3	-0.9	-2.1
2 (UO2_900K)	Ref. XS	41.5	41.3	40.9	40.4	39.8	39.2	38.2	36.7	34.5	30.9
	Subgroup	-46.8	-46.5	-46.0	-45.4	-44.7	-43.9	-42.4	-40.0	-36.3	-28.5
	ESSM	-46.9	-46.6	-46.1	-45.4	-44.7	-43.8	-42.2	-39.9	-36.1	-28.6
	ESSM-X	-0.5	-0.5	-0.3	-0.1	-0.1	-0.4	-0.4	-0.5	-0.7	-1.5
3 (UO2_1200K)	Ref. XS	38.5	38.4	38.3	37.9	37.4	36.7	35.8	34.3	32.3	29.1
	Subgroup	-41.1	-41.1	-41.0	-40.4	-39.6	-38.6	-37.0	-34.4	-30.2	-22.4
	ESSM	-41.3	-41.2	-41.1	-40.5	-39.6	-38.5	-36.8	-34.1	-29.9	-22.3
	ESSM-X	0.5	0.3	-0.1	0.1	0.2	0.0	0.0	0.0	-0.1	-0.7
4 (UO2_para900K)	Ref. XS	39.4	39.5	39.6	39.6	39.4	39.0	38.1	36.9	35.0	31.4
	Subgroup	-42.6	-43.1	-43.5	-43.9	-43.9	-43.6	-42.7	-41.1	-38.1	-31.1
	ESSM	-42.8	-43.2	-43.6	-43.9	-43.8	-43.5	-42.5	-41.0	-38.1	-31.4
	ESSM-X	0.5	0.5	0.4	0.2	0.2	0.1	0.3	0.2	0.1	-0.4
5 (UO2_para1200K)	Ref. XS	36.8	37.1	37.2	37.3	37.1	36.9	36.2	35.1	33.1	29.7
	Subgroup	-36.9	-37.8	-38.5	-39.0	-39.0	-39.0	-38.2	-36.5	-33.0	-25.4
	ESSM	-37.3	-38.1	-38.6	-39.1	-39.0	-38.8	-38.0	-36.3	-32.9	-25.6
	ESSM-X	0.8	0.6	0.7	0.5	0.8	0.5	0.4	0.4	0.5	0.0
6 (UO2_3%)	Ref. XS	42.5	42.1	41.8	41.5	41.0	40.4	39.6	38.3	36.4	32.8
	Subgroup	-49.6	-49.2	-48.8	-48.4	-47.8	-46.9	-45.9	-44.1	-41.0	-34.3
	ESSM	-49.5	-49.0	-48.7	-48.3	-47.7	-46.8	-45.7	-44.0	-41.0	-34.5
	ESSM-X	-0.1	0.1	0.0	-0.2	-0.3	-0.3	-0.6	-0.8	-1.2	-1.9
7 (UO2_4%)	Ref. XS	42.6	42.2	41.9	41.5	41.0	40.4	39.5	38.2	36.3	32.7
	Subgroup	-49.6	-49.2	-48.9	-48.4	-47.8	-46.9	-45.8	-43.9	-40.8	-34.1
	ESSM	-49.6	-49.1	-48.8	-48.3	-47.7	-46.8	-45.6	-43.8	-40.8	-34.3
	ESSM-X	-0.5	-0.3	-0.4	-0.4	-0.5	-0.6	-0.7	-0.7	-1.1	-2.0
8 (UO2_Gd)	Ref. XS	41.7	41.6	41.2	40.9	40.3	39.7	38.8	37.6	35.7	32.4
	Subgroup	-48.7	-48.6	-48.1	-47.6	-46.9	-46.0	-44.7	-42.9	-39.8	-33.6
	ESSM	-48.5	-48.4	-47.8	-47.4	-46.7	-45.8	-44.6	-42.8	-39.8	-33.7
	ESSM-X	0.1	-0.5	-0.3	-0.4	-0.4	-0.5	-0.6	-0.9	-1.1	-2.2
9 (MOX_16%)	Ref. XS	41.1	40.7	40.3	39.9	39.3	38.6	37.6	36.4	34.5	31.3
	Subgroup	-48.4	-48.0	-47.4	-46.9	-46.2	-45.2	-43.9	-42.1	-39.2	-33.3
	ESSM	-47.6	-47.1	-46.5	-46.0	-45.2	-44.2	-42.7	-40.8	-37.6	-31.3
	ESSM-X	-0.4	-0.4	-0.1	-0.3	-0.2	-0.3	-0.3	-0.6	-1.0	-1.9

The MCNP reference cross sections are shown in barns and the entries for the other methods are the relative errors in %.

Multiplying the effective cross sections by group-wise fluxes gives the reaction rate per atom in different rings of the fuel. In order to rule out the flux discrepancies between MCNP and DeCART due to the sources other than resonance calculation, instead of directly using the MCNP reaction rates as reference solution, the effective cross sections tallied from MCNP are fed to DeCART to calculate the reference reaction rates. To discuss the distributed self-shielding and resonance interference effect separately, two types of figures are created. The first type of figure depicts the radially dependent reaction rates for a specific energy group or integrated over the entire resonance energy range (e.g., 0.625eV to 25keV). This type of figure is best for the dominant isotopes such as U-238. The other type plots the energy dependent reaction rates that are spatially integrated over all fuel annuli. This type of figure best illustrates the resonance interference effect among resonance isotopes, especially for the non-dominant resonance isotopes whose spectra are strongly disturbed by the dominant isotopes.

Figure 5.5-Figure 5.8 show the radially dependent absorption rates of U-238 for a few representative cases, namely, Cases 2, 4, 8 and 9. In these figures, two resonance groups are considered, Group 34 (6.5eV-6.88eV) and Group 22 (116.0eV-117.5eV), as well as a single group over the entire resonance energy range (0.625eV-25keV). The reference reaction rates are plotted on the upper-left graph of each figure and the rest graphs show the relative errors (%) of the three methods with respect to the reference results for Group 34, 22 and the single group over entire resonance energy range. For ESSM, a 15%-25% underestimation of the total resonance absorption rate in the outermost ring is observed for all four cases. As plutonium buildup tends to peak at the fuel surface, this bias could significantly undermine the accuracy of a multi-region depletion calculation. The errors in the reaction rates with the subgroup method are still significant for an individual group, say Group 34, but tend to be smeared out for the single group over the entire resonance range. It is also seen that the discrepancies of Case 4 with the non-uniform temperature profile are somewhat larger than Case 2 with the uniform temperature, indicative of the lack of a theoretical foundation for treating a non-uniform temperature profile with the subgroup method. Of the three methods, ESSM-X produces the best spatial distribution of the reaction rates, with the largest difference of the entire energy range for any of the cases less than 1.3%.

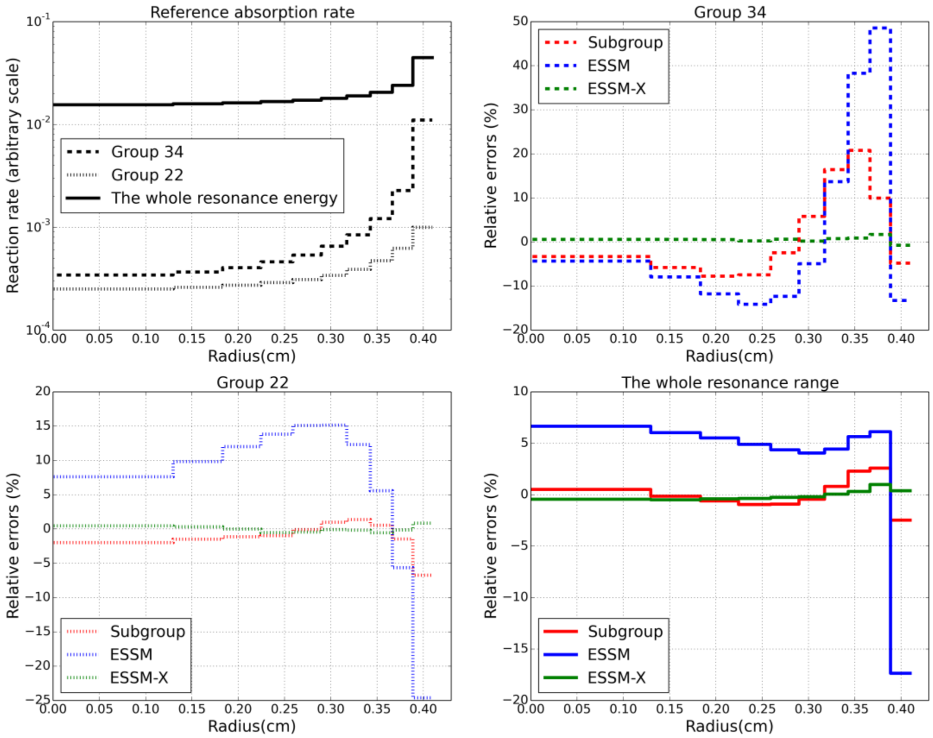

Figure 5.5 Comparison of radially dependent U-238 absorption rate for Case 2 (UO2_900K).

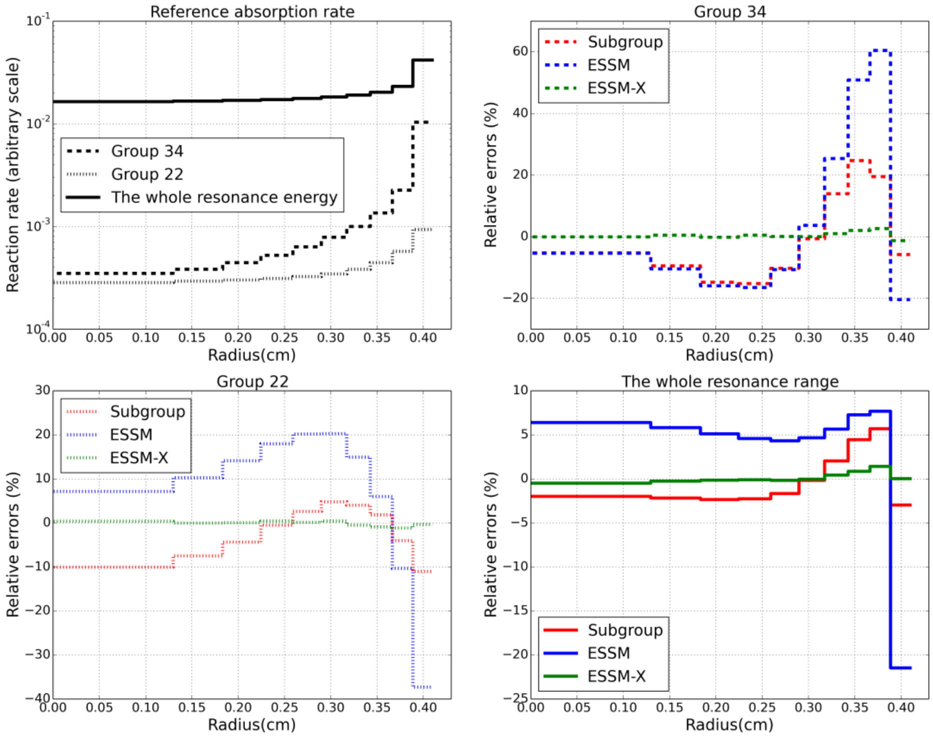

Figure 5.6 Comparison of radially dependent U-238 absorption rate for Case 4 (UO2_para900K)

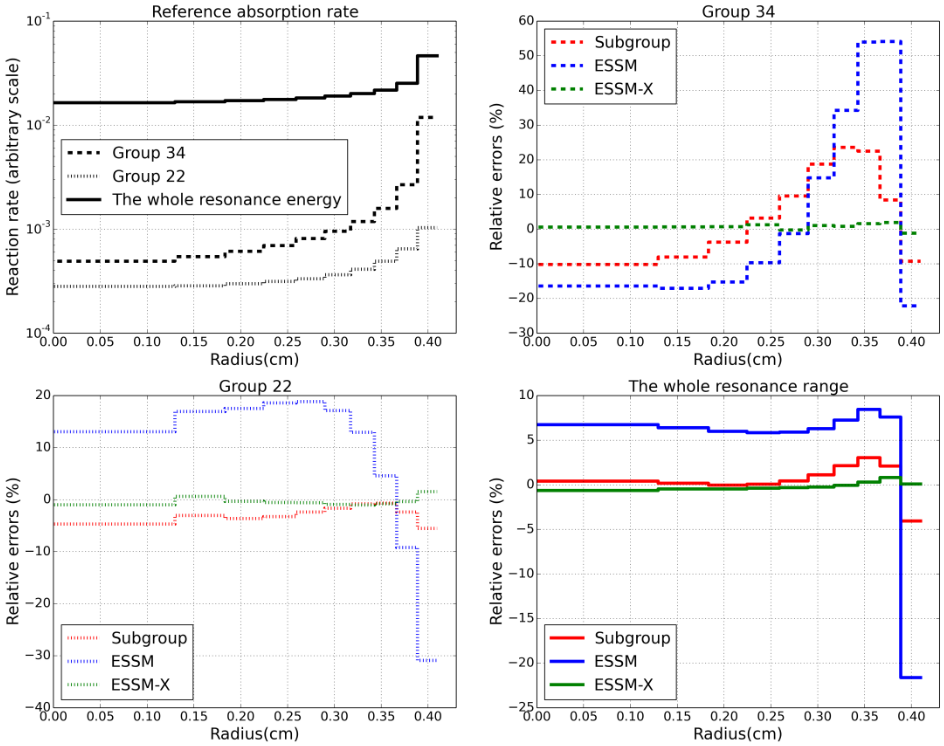

Figure 5.7 Comparison of radially dependent U-238 absorption rate for Case 8 (UO2_Gd)

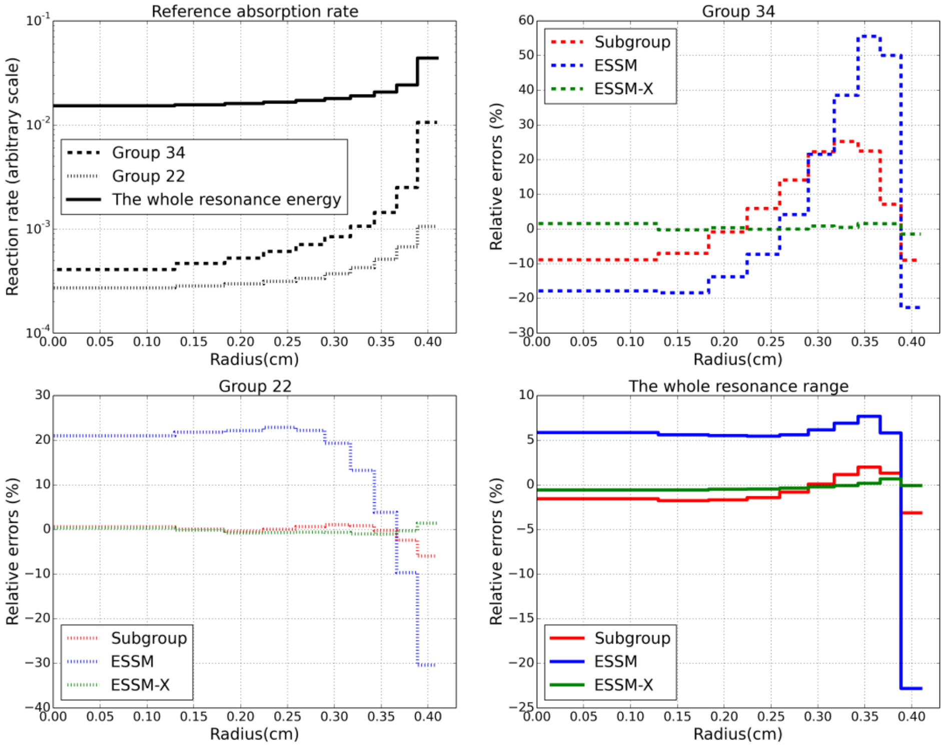

Figure 5.8 Comparison of radially dependent U-238 absorption rate for Case 9 (MOX_16%)

Next, the resonance interference effect is investigated by comparing the energy dependent reaction rates of the three resonance methods with the reference solution. In Figure 5.9-Figure 5.13, the reaction rates of major resonance isotopes for Cases 1, 8 and 9 are compared. On the upper side of each figure shows the reference effective cross section from MCNP to indicate the importance of energy groups where large reaction rate errors occur. On the lower side shows the relative errors of corresponding reaction rates using three resonance methods with respect to the reference results from DeCART (MCNP XS). Take Figure 5.9 for example. Both ESSM and the subgroup method treat resonance interference by Bondarenko iteration, which is unable to produce the correct reaction rates for U-235 at the energy ranges where there are large resonances of U-238 (e.g., 6.67eV, 21eV and so on). Since the overlap of the resonances between U-235 and U-238 varies in different energy ranges, the errors of ESSM and the subgroup method can be positive or negative. For all the test cases, ESSM-X significantly improves the energy dependent reaction rates of major resonance isotopes. The resonances of different resonance isotopes interact with each other, resulting in greater relative errors on the isotopes with small densities. In addition to U-235, the absorption rates of Gadolinium isotopes in Case 8 and Plutonium isotopes in Case 9 are all improved by rigorously treating the resonance interference by ESSM-X.

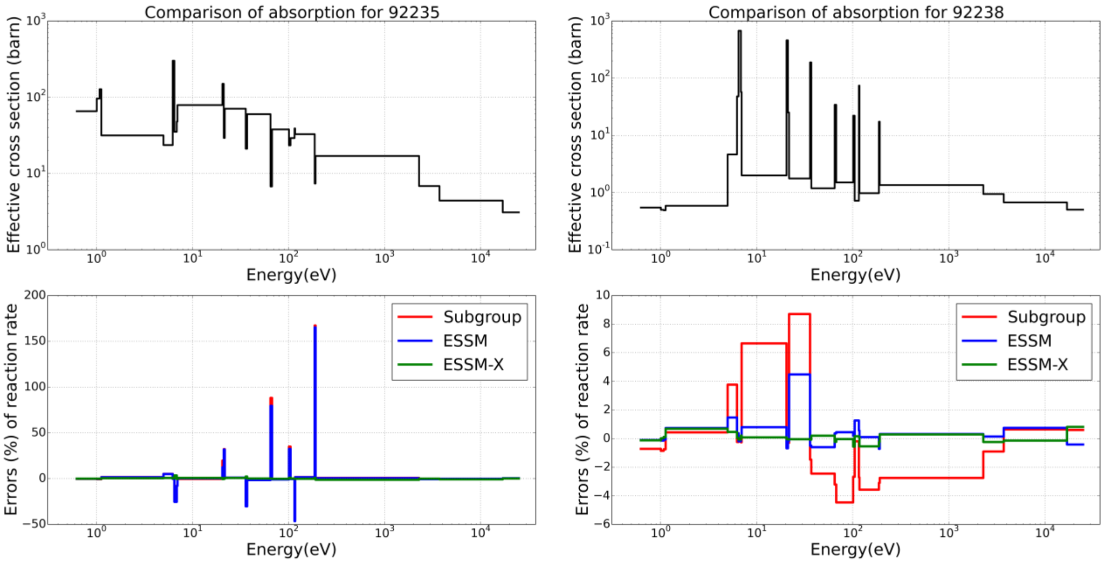

Figure 5.9 Comparison of energy dependent absorption rate of U-235 and U-238 for Case 1 (UO2-600K)

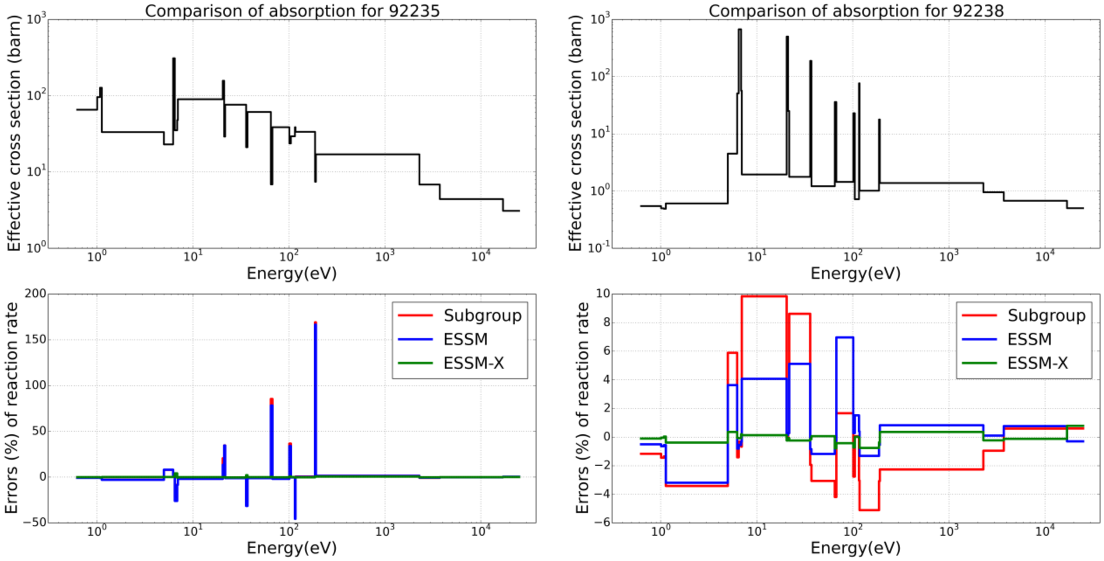

Figure 5.10 Comparison of energy dependent absorption rate of U-235 and U-238 for Case 8 (UO2-Gd)

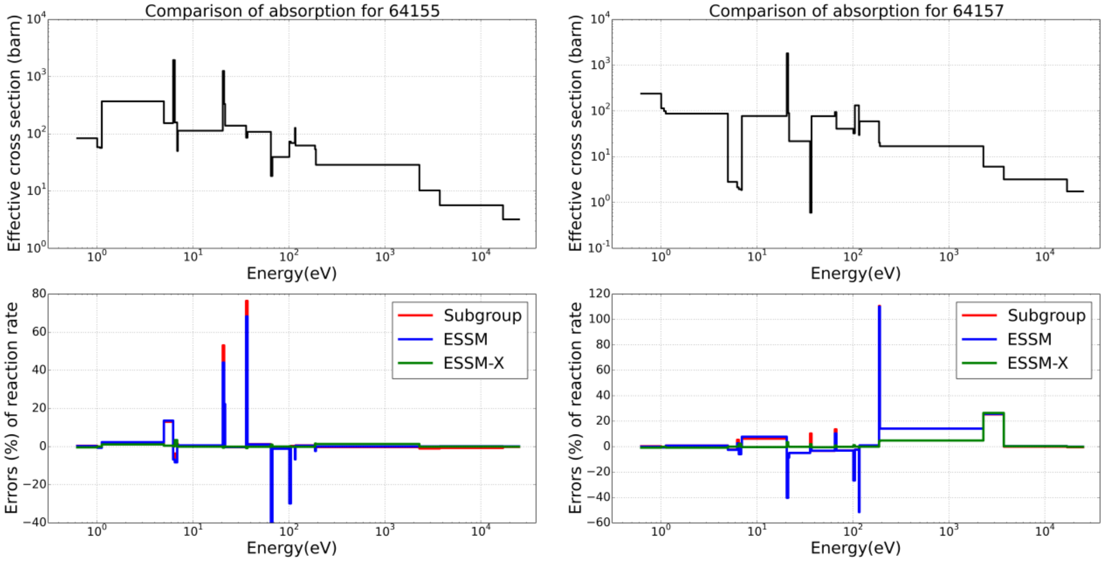

Figure 5.11 Comparison of energy dependent absorption rate of Gd-155 and Gd-157 for Case 8 (UO2-Gd)

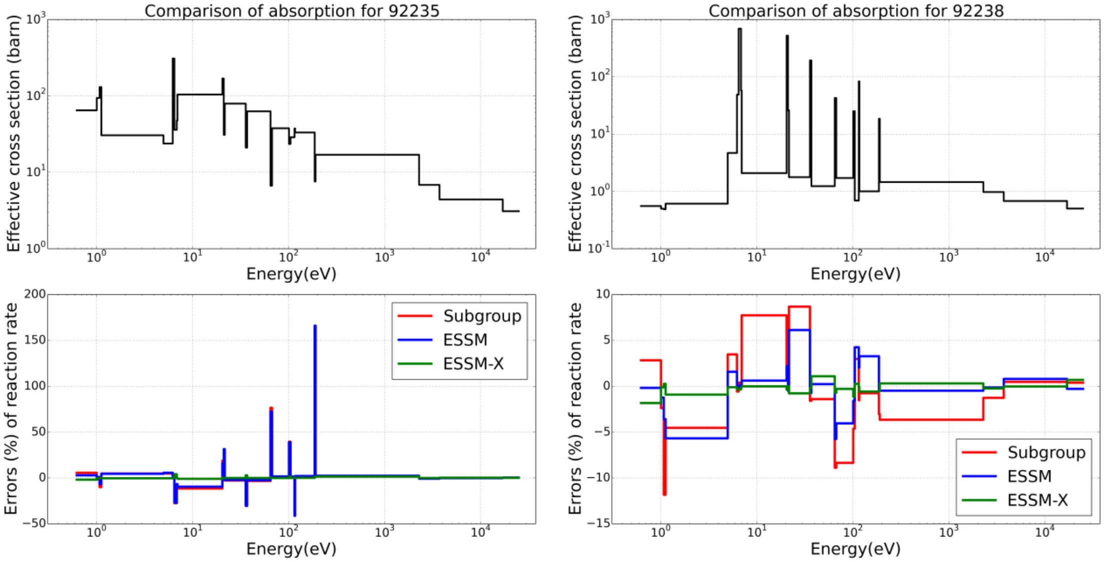

Figure 5.12 Comparison of energy dependent absorption rate of U-235 and U-238 for Case 9 (MOX-16%)

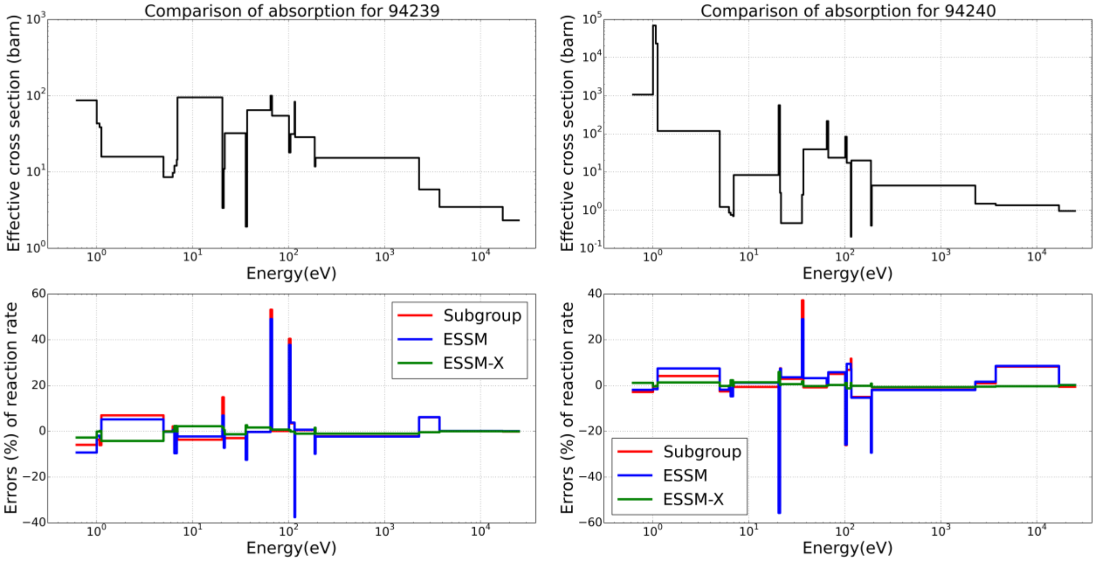

Figure 5.13 Comparison of energy dependent absorption rate of Pu-239 and Pu-240 for Case 9 (MOX-16%)

Table 5-6 compares the effective multiplication factors and the reaction rates of resonance isotopes over the entire resonance energy range (0.625eV-25keV). The reference results are still obtained by running DeCART with MCNP tallied cross sections. It is not surprising that for most cases ESSM and the subgroup method show larger discrepancies for the U-238 absorption rates, consistent with earlier results with spatial shielding. Although very large differences were seen in the analysis of U-235 group-wise reaction rates, the total absorption and fission rates over the entire resonance energy range are reasonable for ESSM and subgroup method, probably a consequence of error cancellation. In Cases 8 and 9 where the resonance interference effect becomes complicated due to the increased number of resonance isotopes, ESSM-X substantially reduces the error of integrated reaction rates, as compared to ESSM and the subgroup method. Overall, ESSM-X gives good agreement of eigenvalues for all the cases.

Table 5-6 Comparison of effective multiplication factors and reaction rates

Case	Item	Reference[a]	Relative Errors[b]		
			Subgroup	ESSM	ESSM-X
1	k_{eff}	1.39274	-65	-137	-19
	U-238 abs. rate	0.20074	-0.20	0.39	0.06
	U-235 abs. rate	3.17911	0.57	0.53	0.16
	U-235 fis. rate	2.11842	0.09	0.08	-0.03
2	k_{eff}	1.37980	-68	-147	-22
	U-238 abs. rate	0.20815	-0.14	0.44	0.07
	U-235 abs. rate	3.17343	0.55	0.49	0.18
	U-235 fis. rate	2.11370	0.09	0.06	-0.02
3	k_{eff}	1.36873	-69	-157	-23
	U-238 abs. rate	0.21452	-0.07	0.50	0.08
	U-235 abs. rate	3.16832	0.47	0.40	0.13
	U-235 fis. rate	2.11006	0.04	0.06	-0.05
4	k_{eff}	1.38067	-44	-122	-44
	U-238 abs. rate	0.20760	-0.20	0.32	0.20
	U-235 abs. rate	3.17499	0.57	0.50	0.16
	U-235 fis. rate	2.11436	0.20	0.09	-0.03
5	k_{eff}	1.36956	-88	-148	-54
	U-238 abs. rate	0.21400	-0.22	0.46	0.23
	U-235 abs. rate	3.16876	0.53	0.42	0.10
	U-235 fis. rate	2.10998	0.02	0.04	-0.07
6	k_{eff}	1.30346	-25	-98	9
	U-238 abs. rate	0.19609	-0.18	0.33	0.03
	U-235 abs. rate	3.26510	0.59	0.55	0.20
	U-235 fis. rate	2.17085	0.26	0.21	0.09
7	k_{eff}	1.35644	-49	-121	-9
	U-238 abs. rate	0.19918	-0.15	0.39	0.08
	U-235 abs. rate	3.23523	0.59	0.56	0.20
	U-235 fis. rate	2.15345	0.19	0.17	0.06
8	k_{eff}	0.22695	-1637	-2303	116

	U-238 abs. rate	0.21917	0.07	0.79	-0.05
	U-235 abs. rate	3.50205	-0.43	-0.62	0.13
	U-235 fis. rate	2.31432	-0.60	-0.81	0.13
	Gd-155 abs. rate	9.40270	1.38	1.68	0.68
	Gd-157 abs. rate	4.73023	2.18	2.29	0.43
9	k_{eff}	1.21058	32	-413	-36
	U-238 abs. rate	0.20710	-0.75	-0.03	-0.13
	U-235 abs. rate	2.85008	-2.11	-1.50	0.06
	U-235 fis. rate	1.83015	-1.64	-1.10	0.18
	Pu-239 abs. rate	2.40428	-0.86	-0.58	0.29
	Pu-239 fis. rate	1.46516	-1.35	-1.28	0.36
	Pu-240 abs. rate	3.48122	-0.26	1.01	0.78

[a] Reference reaction rate is per nuclide in an arbitrary scale.

[b] Relative error for k_{eff} is $\Delta\rho$ in pcm. Relative error for reaction rate is in %.

In order to account for the non-uniform temperature distributions in ESSM-X, Step 1 and Step 2-b (Section 4.3) need an average temperature over the fuel rod to compute the base case. The volume-averaged temperature was used for the previous results reported for Cases 4 and 5. As mentioned in Section 3.4.3, other approaches have been developed to determine the average temperature such as a chord averaged temperature. In order to show the adequacy of using the volume-averaged temperature in the correction model, Cases 4 and 5 were rerun with the volume-averaged temperature manually varied by ±50K and ±100K. This temperature variation can be viewed as the range of possible effective temperatures calculated by other methods given in Ref. [47]. Table 5-7 shows that the eigenvalues calculated by ESSM-X have almost no change with variation of the average temperature. The bias introduced by the deviation of the average temperature from the true effective temperature that preserves the neutron capture of the fuel rod is canceled out during the correction of shielded cross sections in Equation (4.13). The volume-averaged scheme is therefore sufficient for the new resonance model.

Table 5-7 Sensitivity of eigenvalue on the average temperature selection

Ave. Temp. variation	**Case 4 (Ave. 900K)**	**Case 5 (Ave. 1200K)**
-100K	1.37979	1.36787
-50K	1.37982	1.36790
+0K	1.37984	1.36792
+50K	1.37987	1.36793
+100K	1.37988	1.36793

It has been verified that the spatial distribution of absorption rates of U-238 are biased when calculated by conventional ESSM or the subgroup method. The underestimation of absorption rates near the fuel surface could result in less plutonium build-up in the rim zone. In Case 10, the depletion calculation is performed with a fine time step using three resonance methods in DeCART. The results are compared with those from an MCNP6 burnup calculation. Figure 5.14 and Figure 5.15 compare the content of Pu-239 and Pu-240 versus burnup in the outermost ring for different methods. At 31.2GWd/tU, the plutonium is underestimated by 20% with ESSM and 5% with the subgroup method. The results of ESSM-X agrees to within 1% with the MCNP results, showing the importance of obtaining correct radial reaction rates for the burnup calculation. In the meantime, we verify the power distribution of the fresh fuel and depleted fuel at 31.2 GWd/tU. In Figure 5.16, the agreements of the three resonance methods with MCNP are equally good for the fresh fuel. However, as shown in Figure 5.17, due to the plutonium underestimation near the fuel surface, ESSM gives significant errors of power density for the fuel depleted to 31.2 GWD/tU. The results with the subgroup method are somewhat better than ESSM, while ESSM-X gives the best power density agreement with the MCNP reference, which is consistent with the distributed self-shielding results.

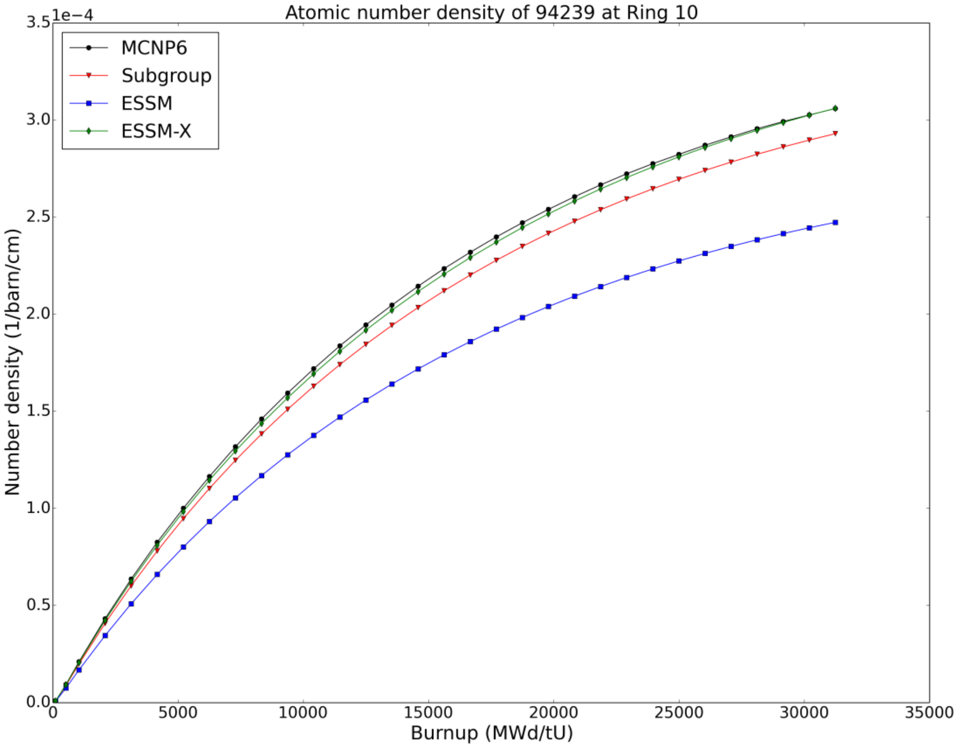

Figure 5.14 Comparison of Pu-239 content in the rim zone for Case 10

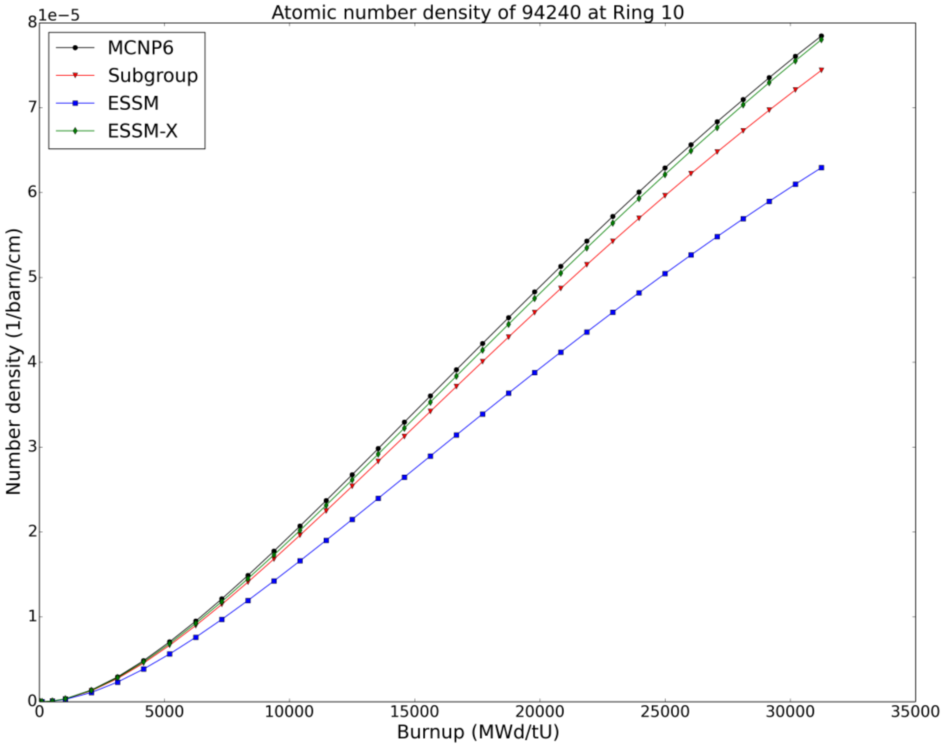

Figure 5.15 Comparison of Pu-240 content in the rim zone for Case 10

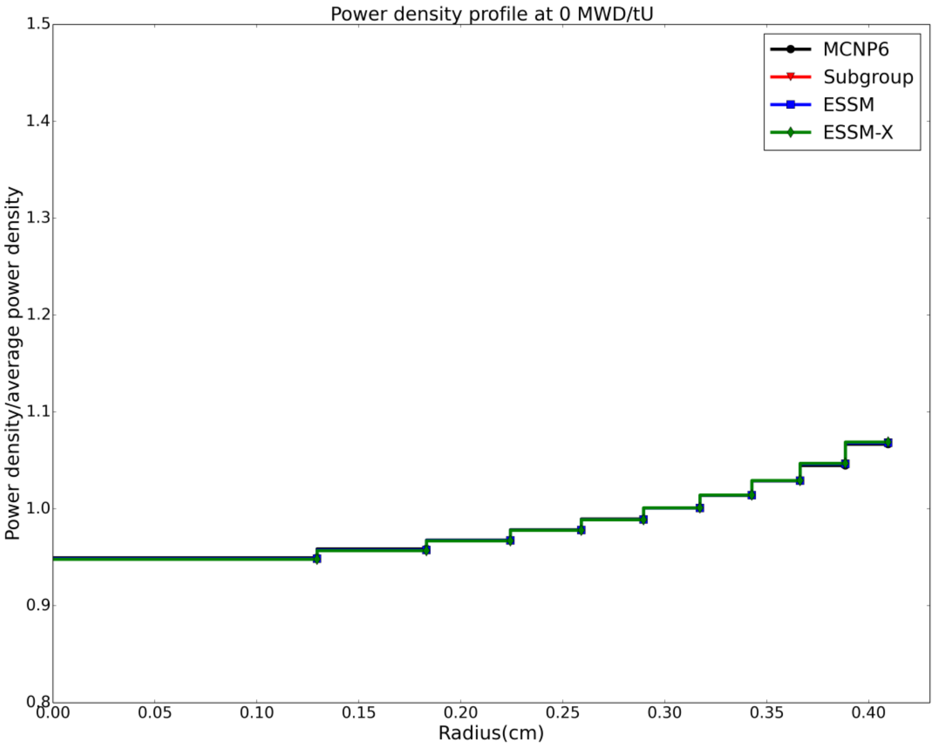

Figure 5.16 Comparison of power distribution for a fresh fuel

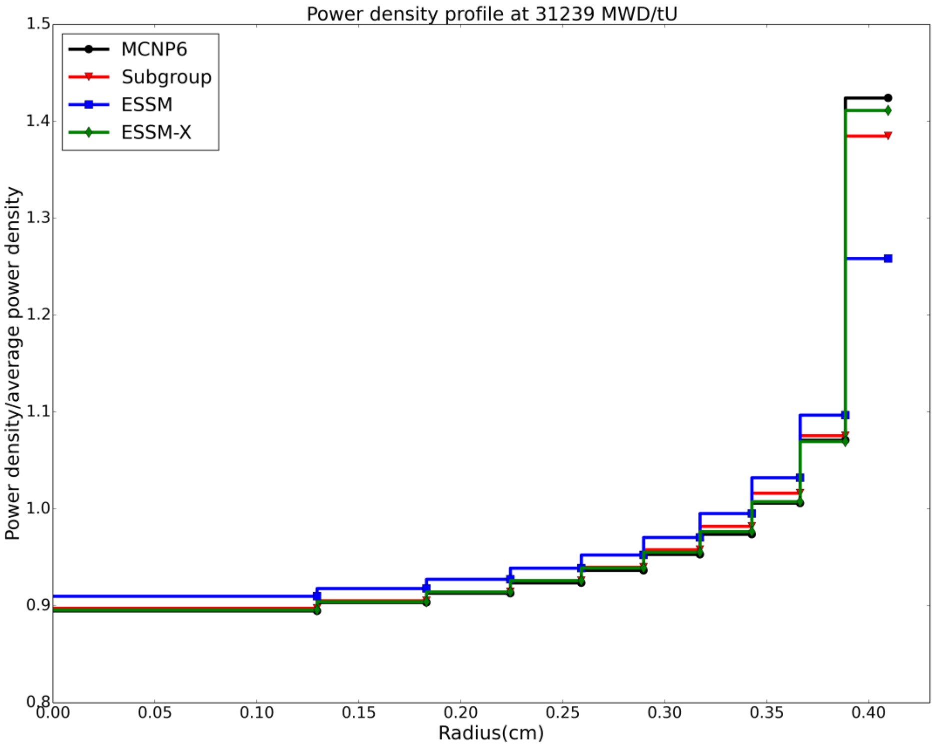

Figure 5.17 Comparison of power distribution at 31.2 GWD/tU

5.3.2 Non-uniform Lattice

The cases of Group 2 (see Section 5.1) verify the capability of resonance methods for inter-pin shielding and this inter-pin effect on the quasi-1D model. For Case 11 (UO2_water), Figure 5.18 and Figure 5.19 show the energy dependent absorption rates of U-235 and U-238 for every fuel pin of the 1/8 lattice (see Figure 5.1). The typical effective cross sections of the resonance isotope are plotted at the upper-left corner to indicate the importance of energy groups where large reaction rate errors occur. The rest of the graphs show the relative errors of the absorption rate for the three resonance methods at different pin locations. Similar to the uniform lattice case, the interference effect is far better modeled with ESSM-X compared to the subgroup method or ESSM, in spite of the presence of the central water rod which increases the equivalence cross section of its peripheral pins. The group-wise reaction rate error with ESSM-X is well within 3% for U-235 and 1% for U-238, compared to that for the subgroup method and ESSM with a typical error of 50%~150% for U-235 and 5%~10% for U-238. In addition, the radially dependent absorption rates of U-238 for different pin locations are also well predicted by ESSM-X, as shown in Figure 5.20.

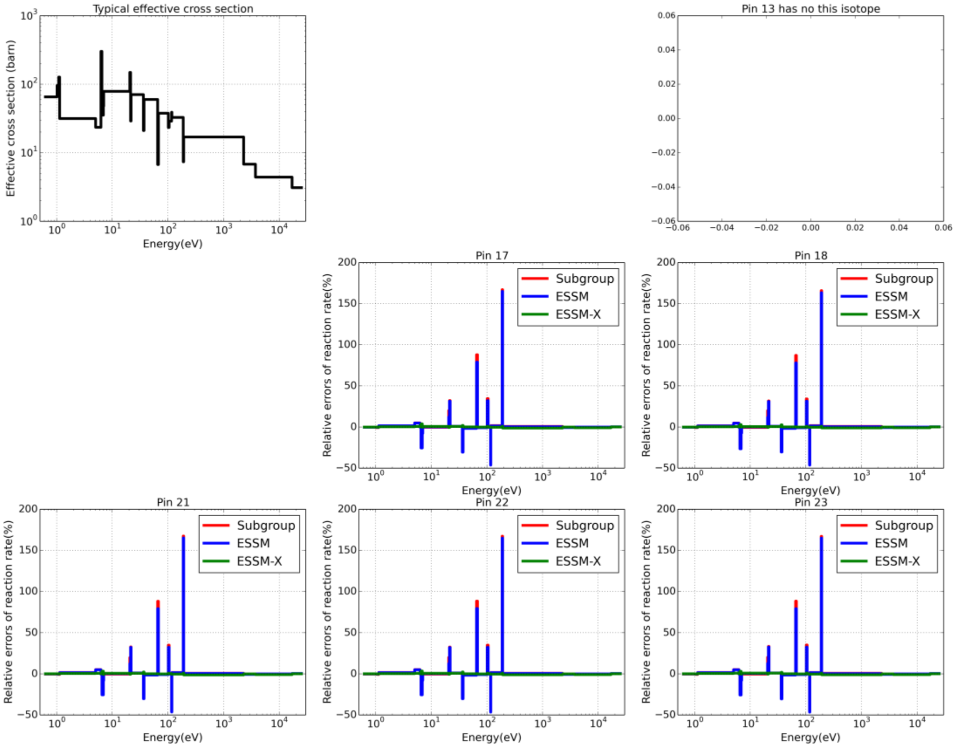

Figure 5.18 Comparison of energy dependent U-235 absorption for Case 11 (UO2_water)

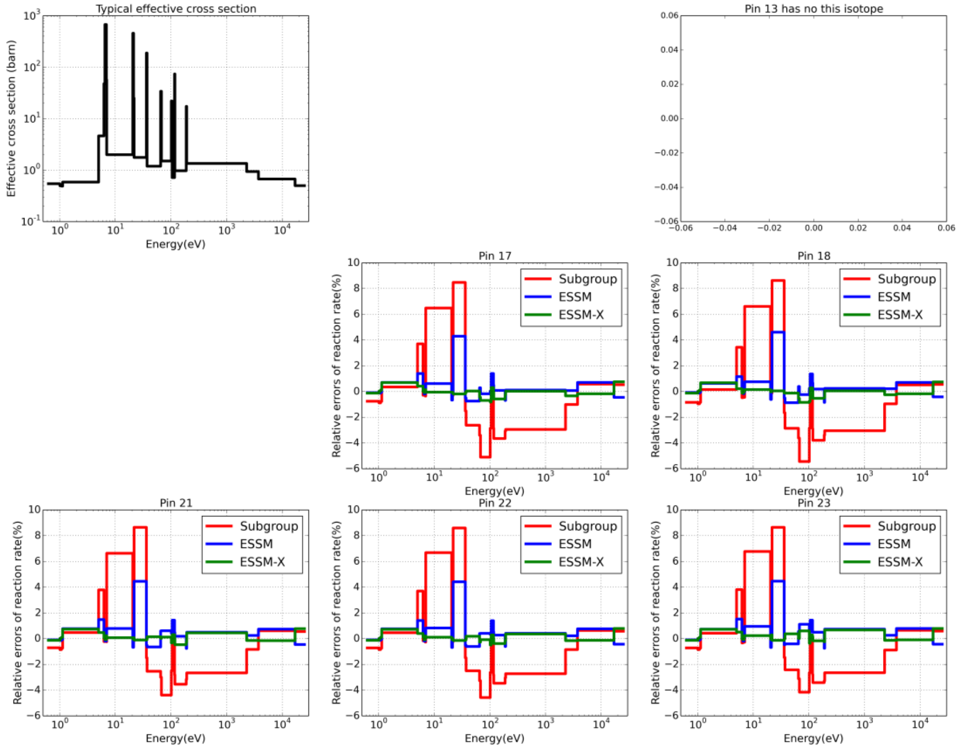

Figure 5.19 Comparison of energy dependent U-238 absorption for Case 11 (UO2_water)

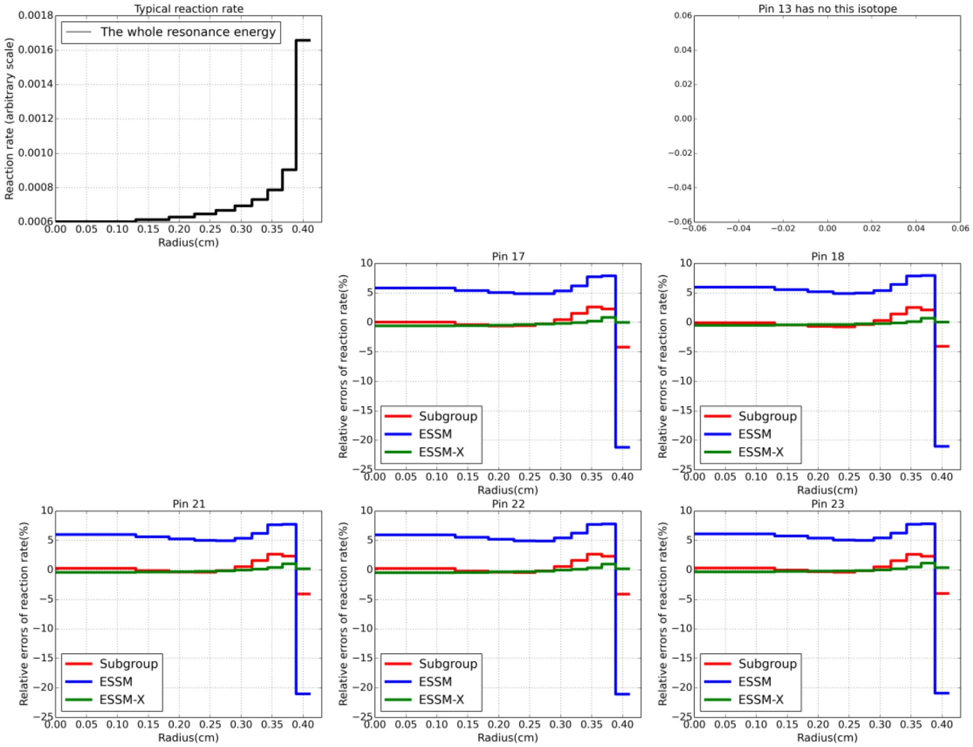

Figure 5.20 Comparison of radially dependent U-238 absorption for Case 11 (UO2_water)

A control rod and a Gd fuel pin are included in Case 12 (UO2_AIC) and Case 13 (UO2_UO2+Gd), respectively. Figure 5.21 shows the energy dependent absorption rates of U-238 for Case 12. The fuel pin right below the control rod (Pin 18) has relatively larger errors with ESSM and ESSM-X than those away from the control rod. The energy groups with large errors are basically away from the major U-238 resonance peaks, and are mostly of negative errors. Since the absorption cross sections in these groups are not large enough to dominate the spectra, the contribution from control rod to the spectra of fuel becomes non-negligible. Noting that the resonance interference effect is modeled for each fuel rod independently, the interference among different pins is, in fact, approximately treated by computing the equivalence cross section (Dancoff correction). This treatment assumes a constant absorption cross section for each group, thus reduces the equivalence cross section of the fuel pin due to absorption of control rod, and finally underestimates the effective cross sections of U-238. Figure 5.22 plots the radially dependent absorption rates of U-238, which is another way to show this bias for Pin 18. The errors of radially dependent reaction rates with ESSM-X are shifted downward but the shape of the error is still flat. Therefore, the negative errors do not originate from the 1-D slowing-down model, but from the methodology of ESSM which requires the lattice consisting of similar pins. Since the subgroup method utilizes isotope category for resonance calculation, U-238 cannot 'see' control rod materials when the FSP of U-238 category is performed. Thus, the error of subgroup method for Pin 18 is almost the same as for the other pins. It is seen from Figure 5.23 and Figure 5.24 that on the other hand, the results of Case 13 using ESSM-X do not suffer from the underestimation issue. The content of gadolinium is relatively small in the fuel, which maintains the similarity of pins.

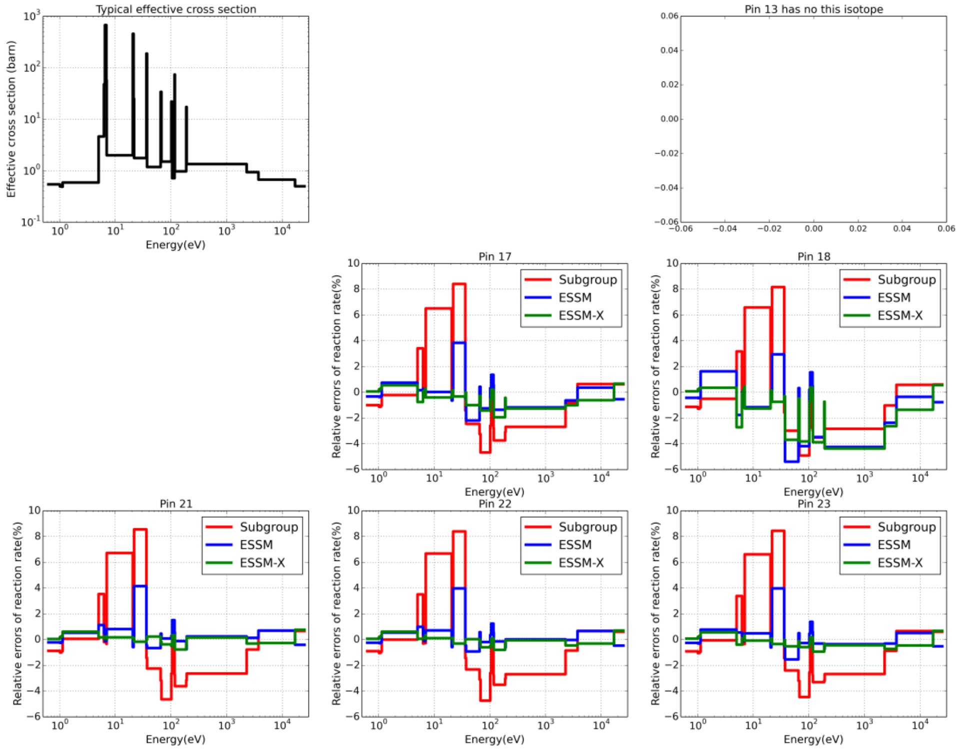

Figure 5.21 Comparison of energy dependent U-238 absorption for Case 12 (UO2_AIC)

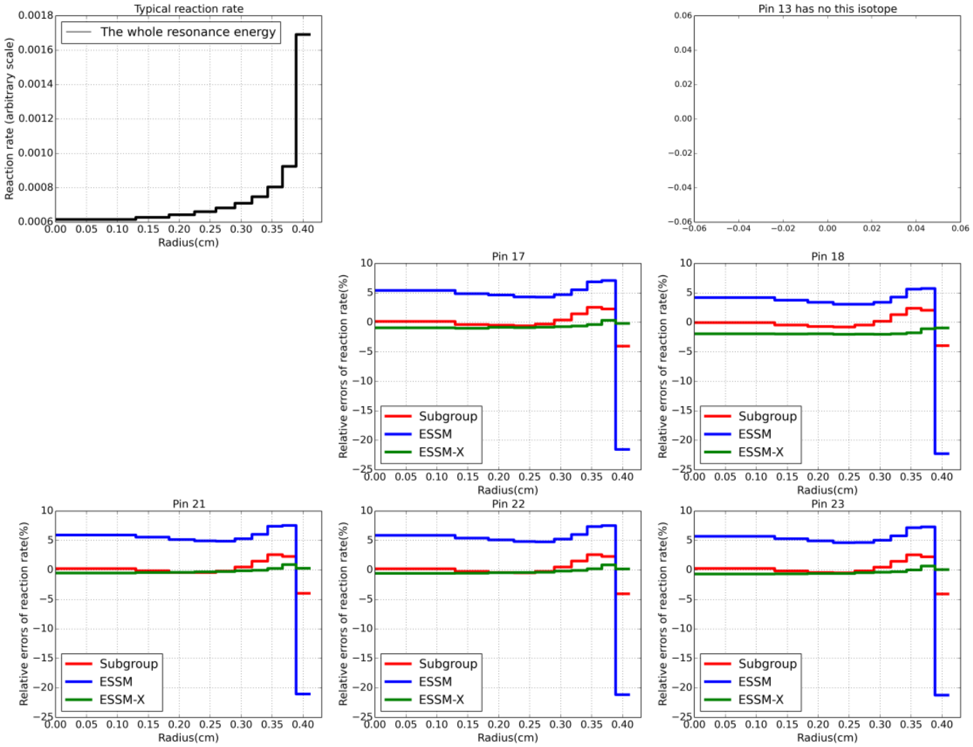

Figure 5.22 Comparison of radially dependent U-238 absorption for Case 12 (UO2_AIC)

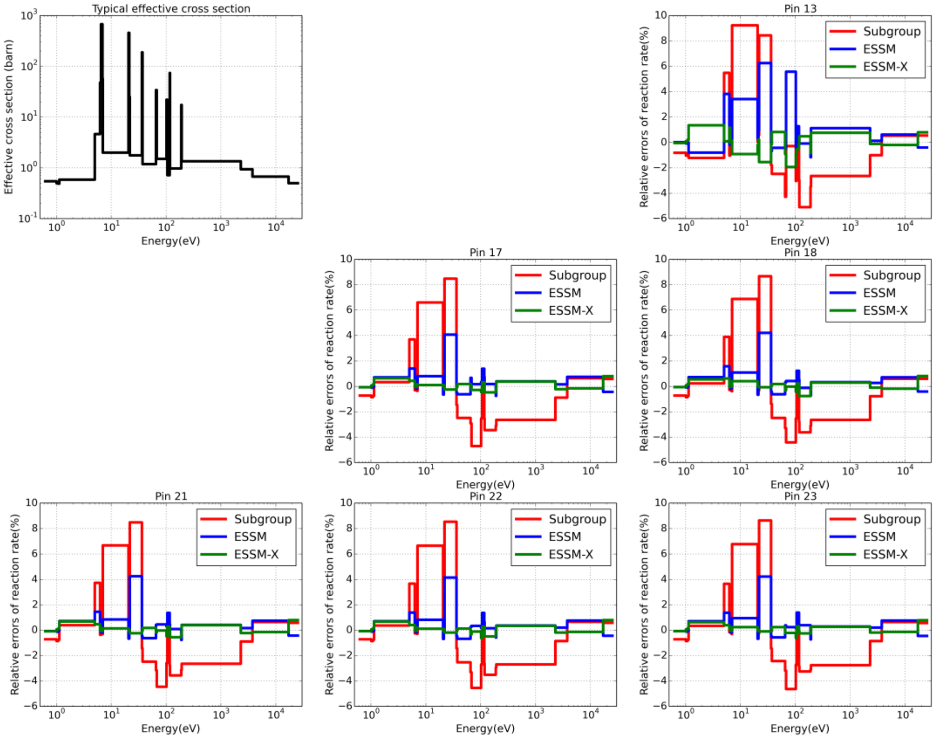

Figure 5.23 Comparison of energy dependent U-238 absorption for Case 13 (UO2_UO2+Gd)

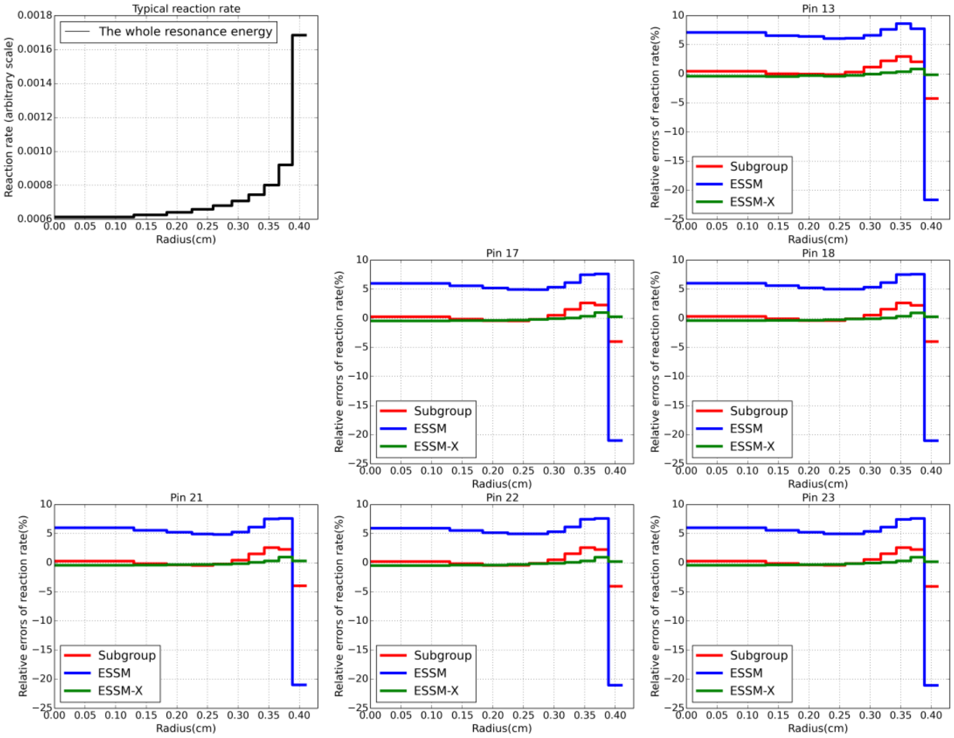

Figure 5.24 Comparison of radially dependent U-238 absorption for Case 13 (UO2_UO2+Gd)

Case 14 (UO2_3%+5%) and 15 (UO2_MOX) incorporate the mixed fuel types of a checkerboard layout. Figure 5.25-Figure 5.28 compare the energy dependent absorption rates of important resonance isotopes of the two cases. Because of the difference of fuel pins, greater errors are expected for ESSM and ESSM-X, especially for the UO2_MOX case. For Case 15, Figure 5.28 shows that the absorption rate errors of U-238 for the subgroup method is similar to those seen in the uniform lattice (see Figure 5.9 and Figure 5.12). These errors come from the quadrature approximation and inaccurate interference treatment of Bondarenko iteration. However, unlike the good agreements of the uniform lattice cases, ESSM-X underestimate the absorption rates of U-238 in a number of groups in the UO2 fuels (e.g., Pin 18), but overestimate them in the MOX fuels (e.g., Pin 17). It is also seen that ESSM has the same trend of errors and these errors occur in the groups with a relatively small U-238 absorption. The reason of the systematical errors for ESSM and ESSM-X is the same as Case 12, i.e., the approximate treatment of inter-pin resonance interference. To make it clear, we look at Group 25 (67.5eV~101.2eV) where significant errors (~10%) occur in Figure 5.28. We compare the effective absorption and equivalence cross sections of Group 25 for U-238 between the uniform lattice and mixed fuel lattice in Table 5-8. The first column shows the reference effective cross section computed from MCNP. The slight differences of effective cross sections in the UO2 fuel between the uniform lattice and mixed lattice, and in the MOX fuel between the uniform lattice and mixed lattice are caused by the inter-pin interaction. ESSM and ESSM-X model this effect correctly for the uniform lattices, but yields biased results for the mixed lattice. As the equivalence cross section is evaluated by solving FSP with group-wise absorption, in Group 25, the UO2 pin sees stronger absorption from neighboring pins in the mixed lattice compared to the uniform lattice, and thus results in a smaller equivalence cross section. In the meantime, the MOX pin sees weaker absorption from neighboring pins in the mixed lattice compared to the uniform lattice, and thus results in a larger equivalence cross section. Unfortunately, this is not valid if the realistic physics is taken into account, as indicated in the reference solution. The issue is the constant group-wise absorption being applied to affect the spectrum, which in reality depends on the detailed point-wise cross sections. The subgroup method is free from the systematical errors because the resonance category treatment leads to uranium ignoring the presence of plutonium and vice versa, when performing the fixed source calculation, although the errors from quadrature approximation and within-pin interference are still significant.

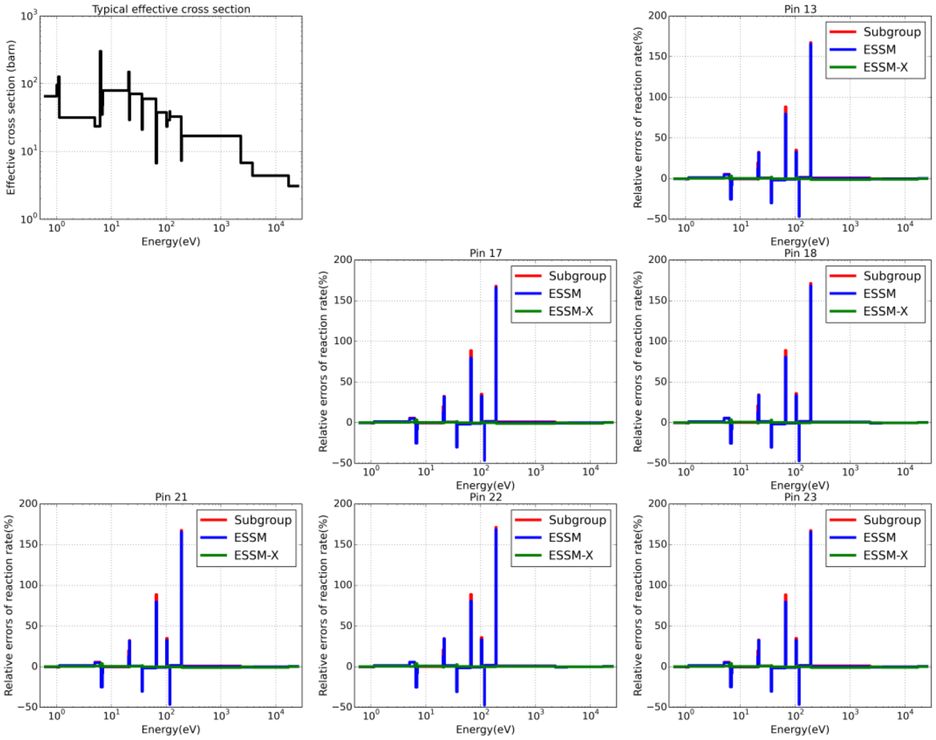

Figure 5.25 Comparison of energy dependent U-235 absorption for Case 14 (UO2_3%+5%)

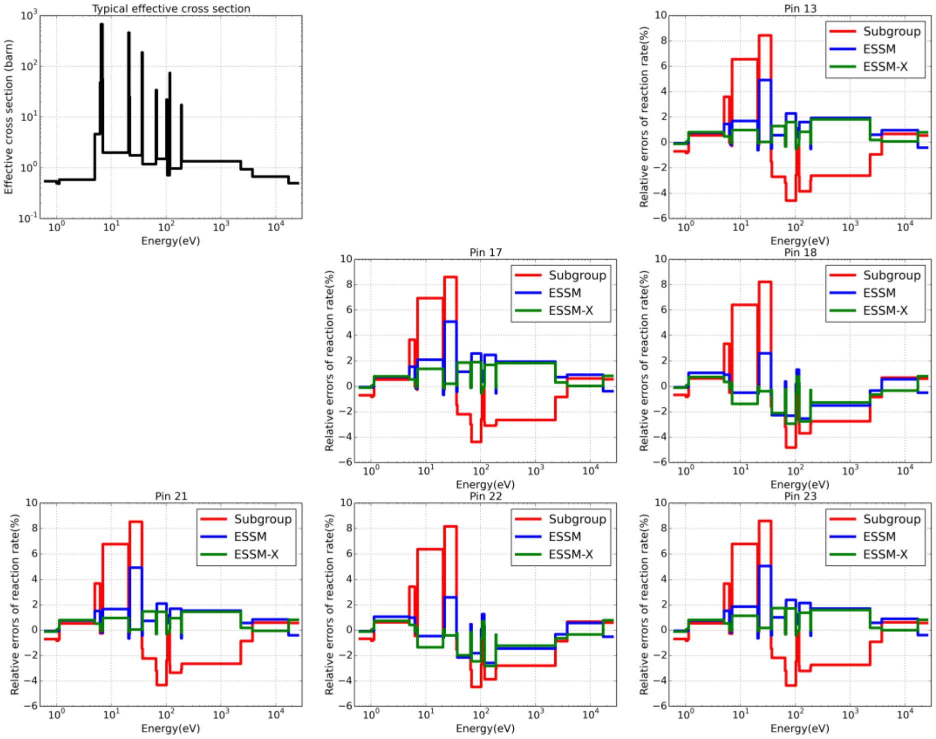

Figure 5.26 Comparison of energy dependent U-238 absorption for Case 14 (UO2_3%+5%)

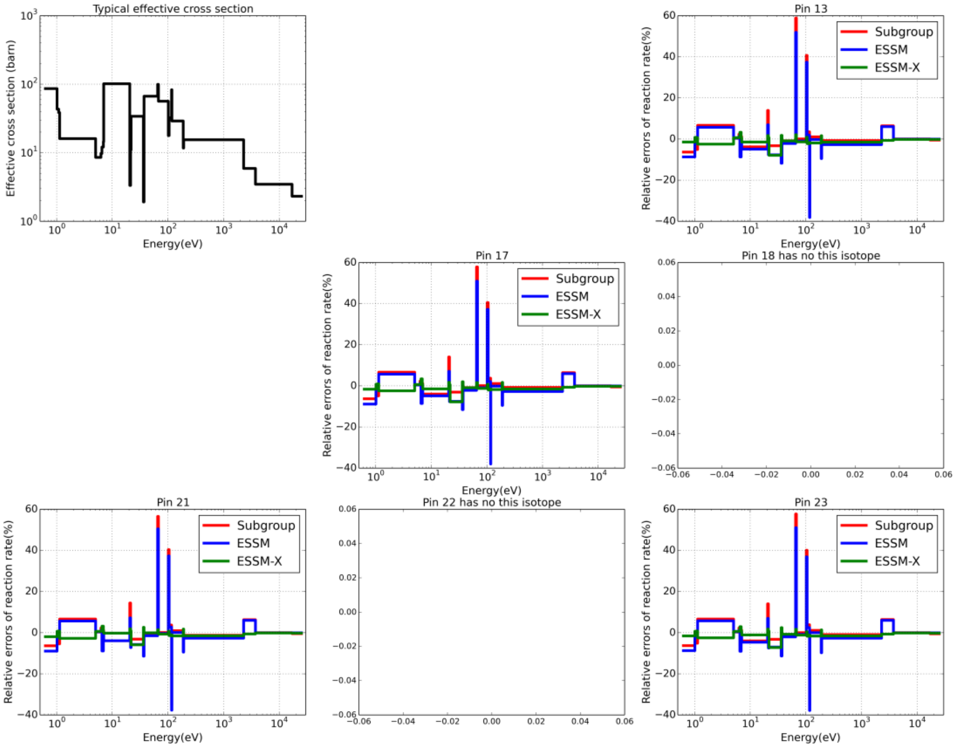

Figure 5.27 Comparison of energy dependent Pu-239 absorption for Case 15 (UO2_MOX)

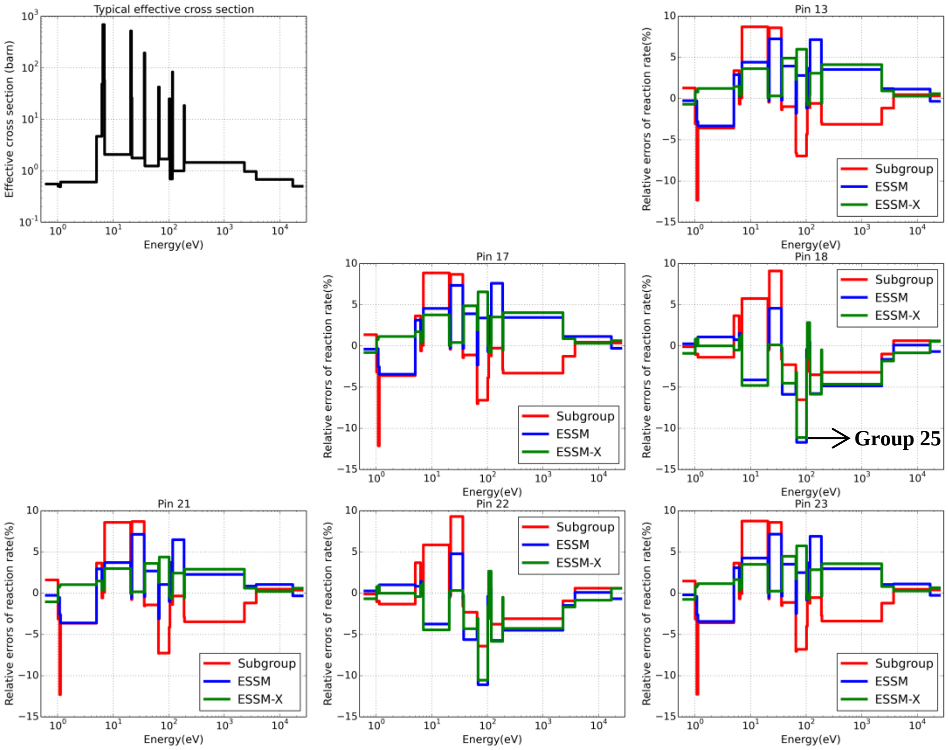

Figure 5.28 Comparison of energy dependent U-238 absorption for Case 15 (UO2_MOX)

Table 5-8 Effective absorption and equivalence cross sections of Group 25 for U-238 for different fuel lattices

Case	Reference absorption XS (barn)	ESSM-X absorption XS (barn)	ESSM-X equivalence XS (barn)
UO2 in uniform lattice[a]	1.510	1.509	43.07
MOX in uniform lattice[b]	1.715	1.710	52.07
UO2 in mixed lattice[c]	1.548	1.371	25.90
MOX in mixed lattice	1.683	1.789	65.70

[a] Uniform lattice for UO2: Case 1 (UO2_600K)
[b] Uniform lattice for MOX: Case 9 (MOX_16%)
[c] Mixed lattice: Case 15 (UO2_MOX)

To summarize, ESSM-X performs very well when the irregularity of lattice consists of moderator or similar fuel rod (Gd fuel). However, the reaction rate errors become larger when the lattice contains absorbers of pins significantly different from each other. Since the formulation of ESSM rests on equivalence theory, treatment of high-order inter-pin interference effects is beyond the scope of the new resonance methodology. Fortunately, such pin layouts (e.g., a mixture of UO2 and MOX in an assembly) are not usually seen in current reactor design. Moreover, the errors in the U-238 absorption rate are in the opposite direction for UO2 and MOX fuel pins, indicating possible error cancellation for the effective multiplication factors, as can be seen in Table 5-9.

Table 5-9 Comparison of multiplication factor for cases of Group 2

Case	Reference k_{eff}	$\Delta\rho$ of subgroup (pcm)	$\Delta\rho$ of ESSM (pcm)	$\Delta\rho$ of ESSM-X (pcm)
11 (UO2_water)	1.40910	-51	-128	-15
12 (UO2_AIC)	1.20539	-196	-284	111
13 (UO2_UO2+Gd)	1.28407	-75	-133	4
14 (UO2_3%+5%)	1.35791	-47	-110	2
15 (UO2_MOX)	1.22387	29	-299	59

5.3.3 Assembly Calculation

To confirm the capability of the resonance methods for realistic reactor core applications, a few representative pins (numbered from 1 to 6) are selected from the two fuel assembly cases (see Section 5.1) for reaction rate analysis as shown in Figure 5.29. Of the UO2 assembly, Pin 1 is next to the water gap while Pin 3 is next to the empty tube (water hole). Pin 2 is away from any extra coolant so it is similar to the fuel pin of infinite lattice. Pins 4, 5 and 6 are MOX fuel pins that have different weight percent of plutonium isotopes. Pins 4 and 5 are located at the boundaries of two different fuels, so that the resonance treatment with assembly heterogeneity can be verified through comparing the results for those pins.

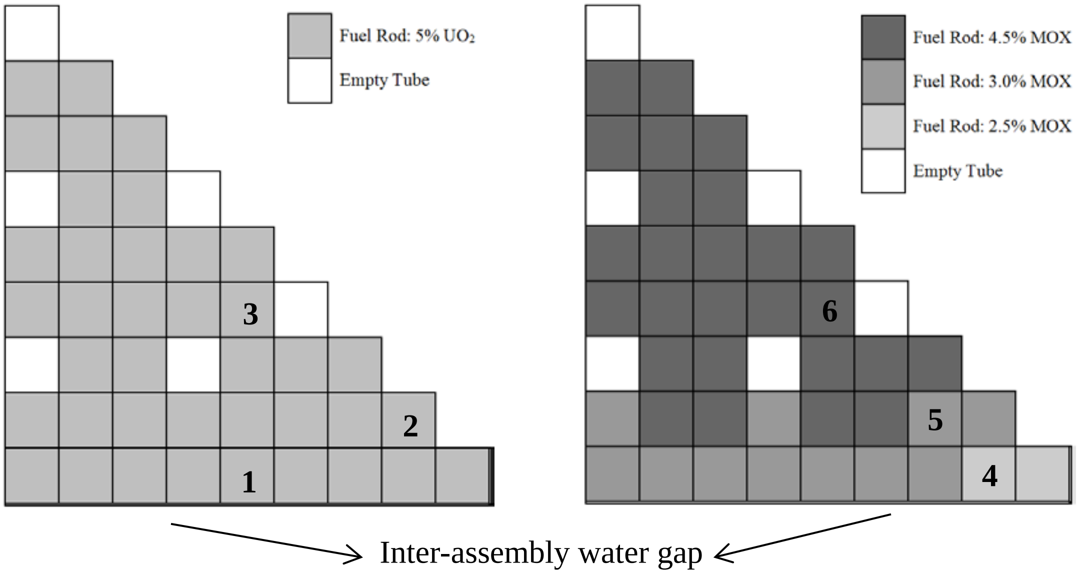

Figure 5.29 Representative pins of assembly cases

In Figure 5.30, the spatially dependent U-238 absorption rate per atom computed by the three resonance methods are compared with the reference results of DeCART (MCNP XS) for the UO2 case. The reference reaction rates are plotted on the upper-left graph and the rest graphs show the relative errors (%) of the three methods with respect to the reference results for Pin 1, 2 and 3, respectively. Because of the larger equivalence cross section introduced by proximity to the water hole/gap, the effective absorption rates of Pin 1 for all fuel annuli is slightly larger than those of Pin 2, and Pin 3 has the largest absorption rates of the three pins. As long as ESSM is able to model the Dancoff effect correctly using single meshes for the fuel regions, the intra-fuel details are accurately retrieved by the ESSM-X, as shown in the graphs of relative errors. These results are as good as the ones for the infinite fuel pin. A similar comparison for the MOX fuel is given in Figure 5.31, which proves again the accuracy of the quasi-1D model for treating the heterogeneity of zoned MOX assembly.

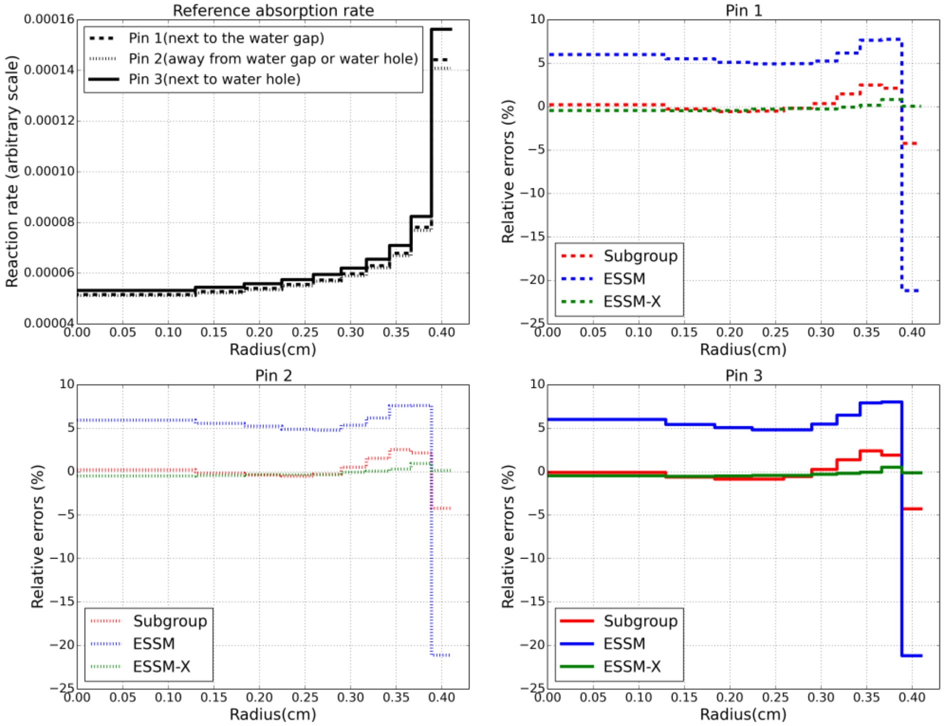

Figure 5.30 Comparison of radially dependent absorption rates of U-238 for Pin 1, 2 and 3 of UO$_2$ assembly.

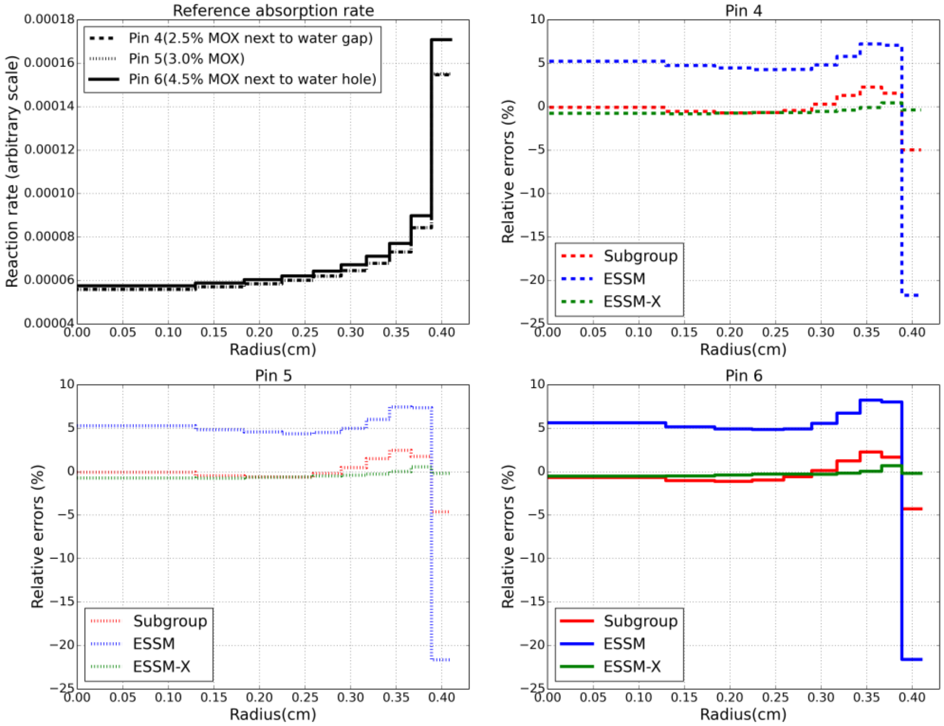

Figure 5.31 Comparison of radially dependent absorption rates of U-238 for Pin 4, 5 and 6 of MOX assembly

The resonance interference treatment for complex fuel material has been analyzed in the infinite MOX pin cell. Consistent results are expected for the MOX assembly problem. Figure 5.32-Figure 5.35 show the energy dependent reaction rate comparison of uranium and plutonium isotopes for the selected pins of MOX assembly. As done previously, the reference effective cross sections are plotted on the upper graphs and the relative errors (%) of reaction rates for the three methods with respect to the reference results are plotted on the lower graphs. Although U-238 is still the dominant resonance isotope, the presence of plutonium isotopes affects the accuracy of the U-238 absorption rates as a result of resonance interference. For example, the ESSM and subgroup method yield large errors in the U-238 absorption rate around the 1eV resonance of Pu-240, and these errors are essentially eliminated by ESSM-X. As shown in Figure 5.33-Figure 5.35, the absorption and fission rates of other non-dominant isotopes such as U-235, Pu-239 and Pu-240 are more accurately predicted by ESSM-X, as compared to ESSM and the subgroup method.

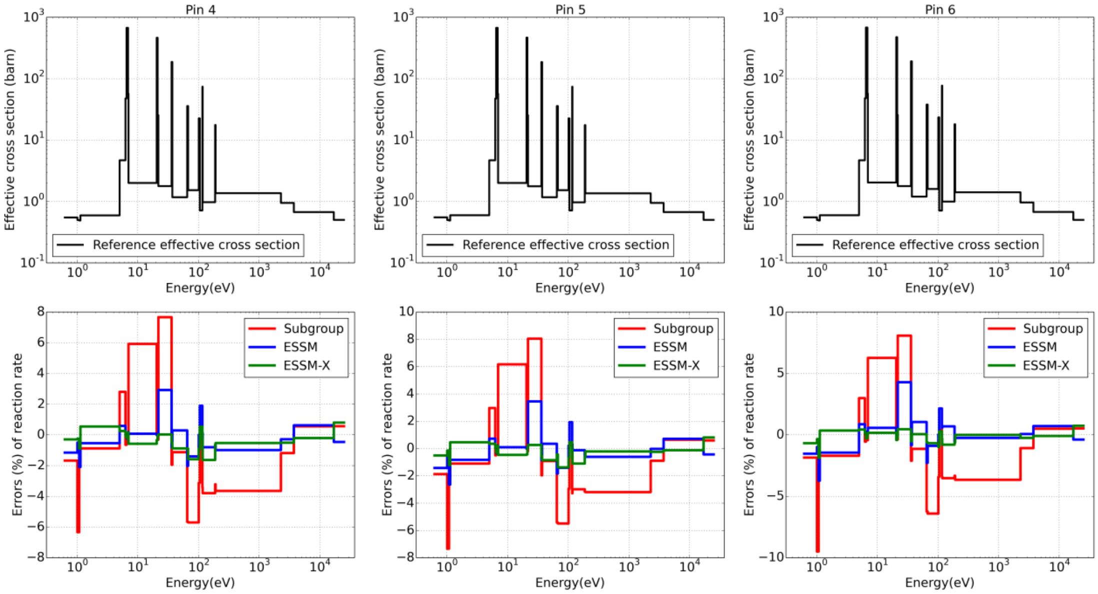

Figure 5.32 Comparison of energy dependent absorption rates of U-238 for Pin 4, 5 and 6 of MOX assembly.

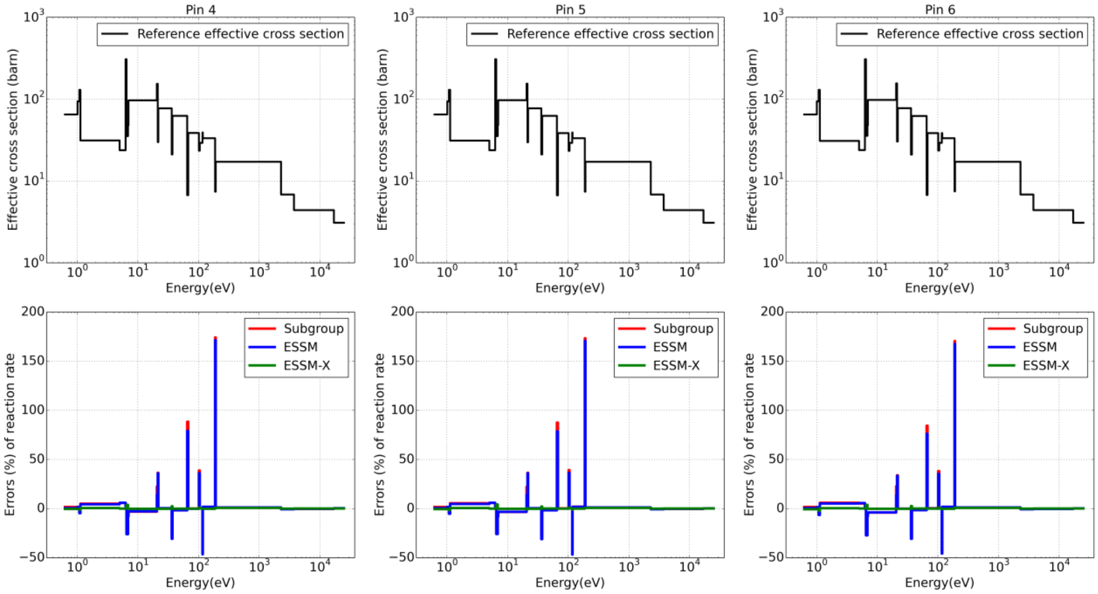

Figure 5.33 Comparison of energy dependent absorption rates of U-235 for Pin 4, 5 and 6 of MOX assembly

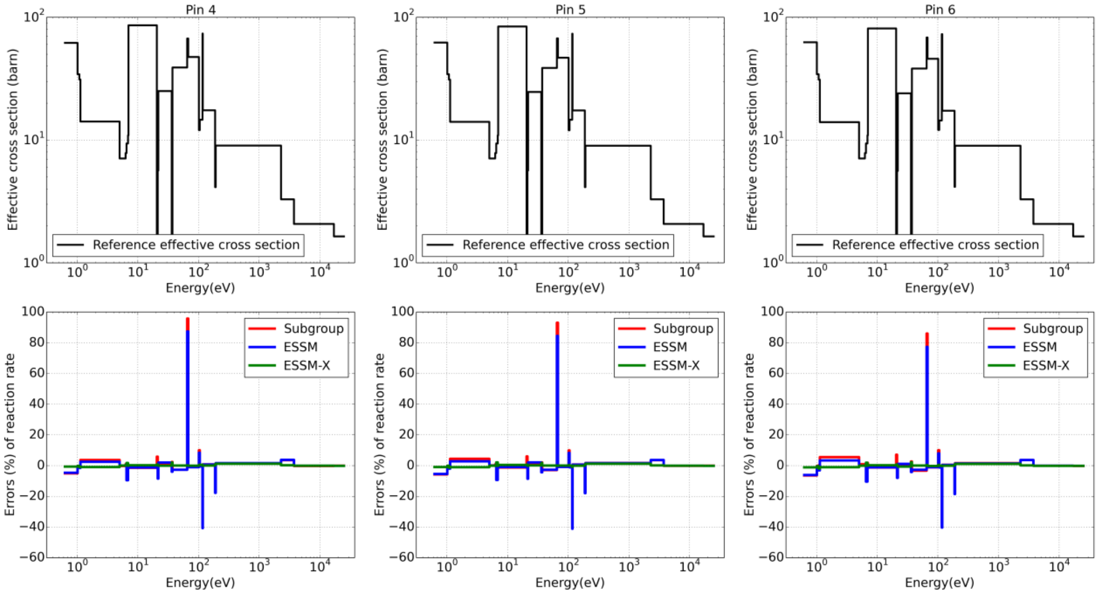

Figure 5.34 Comparison of energy dependent fission rates of Pu-239 for Pin 4, 5 and 6 of MOX assembly

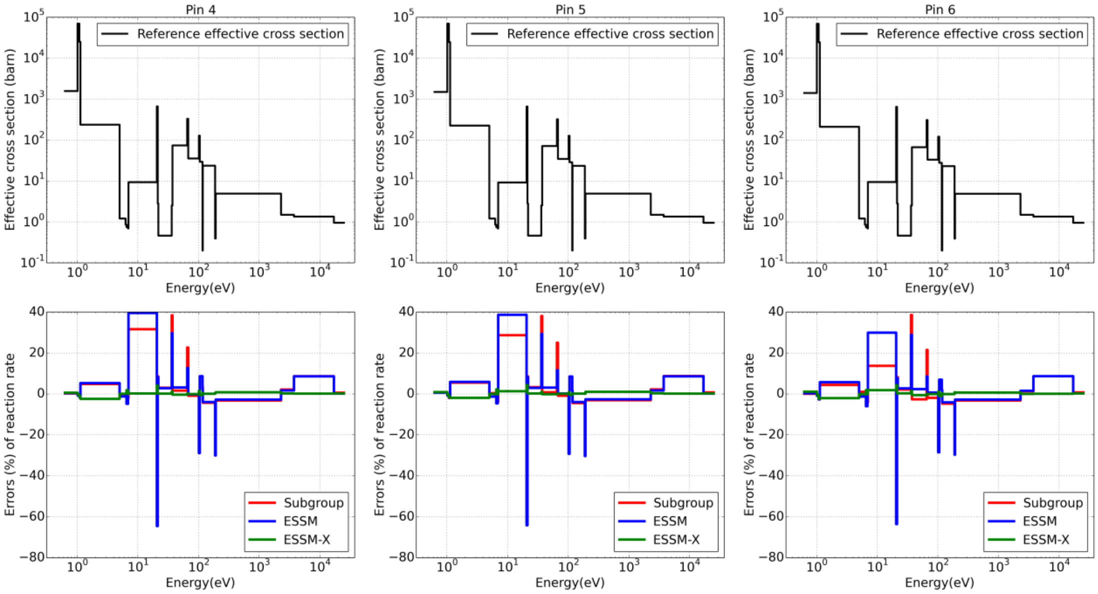

Figure 5.35 Comparison of energy dependent absorption rates of Pu-240 for Pin 4, 5 and 6 of MOX assembly

5.3.4 Computing Resources

As the CE slowing-down calculation is involved in the ESSM-X correction model, it is important to consider the computing resources required for the method. Table 5-10 compares the computing time and memory usage for the subgroup method, ESSM and ESSM-X, leading to the following observations.

(1) The computing times for ESSM and the subgroup method are primarily determined by the number of fixed source problems to be solved. The average number of iterations to converge equivalence cross sections for each group in ESSM is in the range three to five, which is about the same as the number of subgroup levels. However, the subgroup method distributes the resonance isotopes into resonance categories for the fixed source calculations, which leads to additional computing time for the subgroup method.

(2) For most cases, ESSM-X costs an additional 30%~100% of T_{res}, the resonance calculation time, compared to ESSM. Basically, T_{res} is the summation of computing time spent on ESSM iterations and the quasi-1D slowing-down calculation. For a pin cell, longer times for the quasi-1D slowing-down calculation (the values in the brackets) are observed for the cases of non-uniform temperature and complex

material compositions. This is mainly due to the increased size of the energy mesh for the slowing-down calculation to treat either a large number of nuclides or nuclides with a number of temperatures involved in the problem. For the cases with complex materials, the number of resonance isotopes is 3~4 times that of fresh UO_2 fuel, so looping over isotopes to determine the scattering source also becomes more time-consuming. By comparing the problems of different geometrical size, the computing time of quasi-1D slowing-down calculation is roughly increased in a linear manner with the number of pins, which is expected since those slowing-down calculations are independent for different pins. In addition, Cases 16 and 17 even have a shorter T_{res} for ESSM-X than ESSM, because ESSM-X converges the equivalence cross section for each single mesh of the fuel, which could be faster than ESSM that converges the equivalence cross section for the fuel subregions. In all, compared to ESSM, ESSM-X increases the total computing time by about 5%~20% for most cases, which is a modest increase. However, for some cases such as the assembly cases, the total computing time of ESSM-X may be shorter than ESSM.

(3) The memory demand of the slowing-down calculation depends primarily on the number of isotopes and the range of temperatures in the problem. Although the total memory increases with the problem size, the memory used for the slowing-down calculation does not increase since the slowing-down calculations for the fuel pins are independent. This also makes the model easy to be implemented in parallel.

Table 5-10 Computing resources of the resonance methods

Case	Subgroup			ESSM			ESSM-X		
	T_{tot}[1]	T_{res}[2]	Mem.[3]	T_{tot}	T_{res}	Mem.	T_{tot}	T_{res}[4]	Mem.
1	25.83	9.41	103	18.69	2.36	103	20.39	3.24(1.19)	149
2	25.12	9.02	103	18.56	2.20	103	19.72	3.26(1.02)	143
3	25.20	8.80	103	19.43	2.22	103	20.05	3.37(0.99)	142
4	26.85	9.44	103	19.96	2.45	103	22.25	5.05(3.01)	169
5	25.02	8.81	103	18.08	2.34	103	20.54	4.93(2.68)	166
6	26.25	9.45	103	19.95	2.46	103	21.17	3.35(1.17)	145
7	27.49	10.00	103	19.41	2.22	103	20.71	3.24(1.19)	145
8	49.81	22.59	103	31.34	2.42	103	34.96	4.54(2.43)	182
9	47.90	22.46	103	26.96	2.89	103	28.65	4.90(2.29)	188
11	296.0	132.2	238	173.3	33.62	238	192.0	52.29(23.6)	287
12	435.1	291.0	239	219.6	69.72	239	224.2	73.87(26.8)	290
13	391.1	296.2	239	130.0	35.47	239	160.7	63.87(32.1)	314

14	291.1	143.5	239	179.1	34.40	239	204.5	59.83(28.7)	291
15	460.0	311.8	240	193.3	42.70	240	237.8	89.45(51.8)	321
16	2659.9	1195.6	1221	2262.8	808.2	1222	1957.3	494.8(235.8)	1274
17	4513.5	2656.5	1229	3059.2	1176.5	1231	2758.4	913.2(617.8)	1312

[1] T_{tot} is the total computation time (s) of the eigenvalue problem including everything.
[2] T_{res} is the time (s) spent on resonance calculation.
[3] Mem. is the memory usage (MB) of the method.
[4] The value in the bracket is the computing time spent on quasi-1D slowing-down calculation.

5.4 Investigation of Azimuthally Dependent Self-shielding

So far, our method is subject to radial subdivision of the fuel rod. In some circumstance, the azimuthal dependence of the effective cross section becomes important, say a fuel pin close to a water hole or reflector. The azimuthal distribution of the self-shielded cross section in a typical PWR fuel rod is examined by setting up a heterogeneous lattice case of 5×5 pin cell as shown in Figure 5.36. All the yellow pins are fresh UO_2 fuel with 5% enrichment. The central red pin is a water hole. The purpose of the following calculation is to quantitatively show the azimuthal dependence of shielded cross sections within a fuel pin (# 8) adjacent to the water hole.

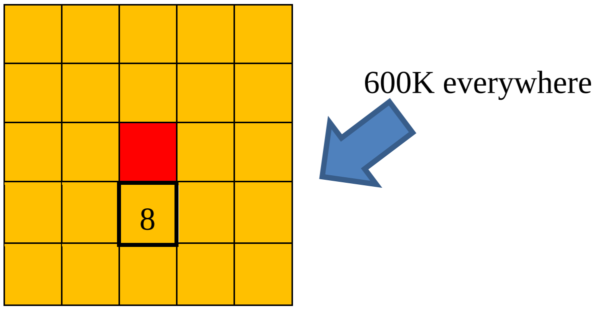

Figure 5.36 Pin layout of the test lattice problem

The MCNP eigenvalue calculation is performed with multigroup flux and reaction rate tally under a specific geometrical mesh of Pin # 8 shown in Figure 5.37. The fuel region is subdivided into three rings, each with eight symmetric azimuthal zones. Sufficient neutrons are simulated (1.6 million per cycle, 700 active cycles) to guarantee that the statistical error of reaction rate in every energy group and every subregion is below 0.5%. Particularly, the shielded cross sections of subregions 1 and 2, which are relatively closer to the water hole, are compared with those of subregions 3 and 4 which are relatively further away. Also, the shielded cross sections of the whole sectors A and B are compared.

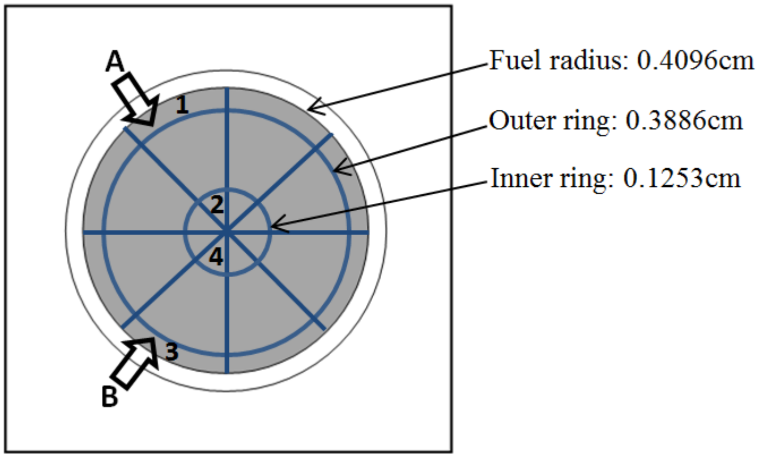

Figure 5.37 Geometrical discretization of Pin 8 for MCNP tally

Figure 5.38 shows the ratio of U-238 effective absorption cross section of Subregion 1 to 3, Subregion 2 to 4 and Sector A to B. Figure 5.39 shows the same comparison for reaction rate. 4%~15% differences for the effective cross sections in major resonance groups are observed by comparing Subregion 1 with 3, which are near the fuel surface, while 10%~35% differences are observed for the reaction rates in these groups (Subregion 1 with 3). Interestingly, for large resonances such as the U-238 6.67eV resonance, the azimuthal difference of the effective cross section is small, but the azimuthal difference of the reaction rate is large, which means that the reaction rate difference is mostly due to the difference in the calculated flux. For small resonances, the azimuthal difference in reaction rate is primarily due to the difference in the effective cross section.

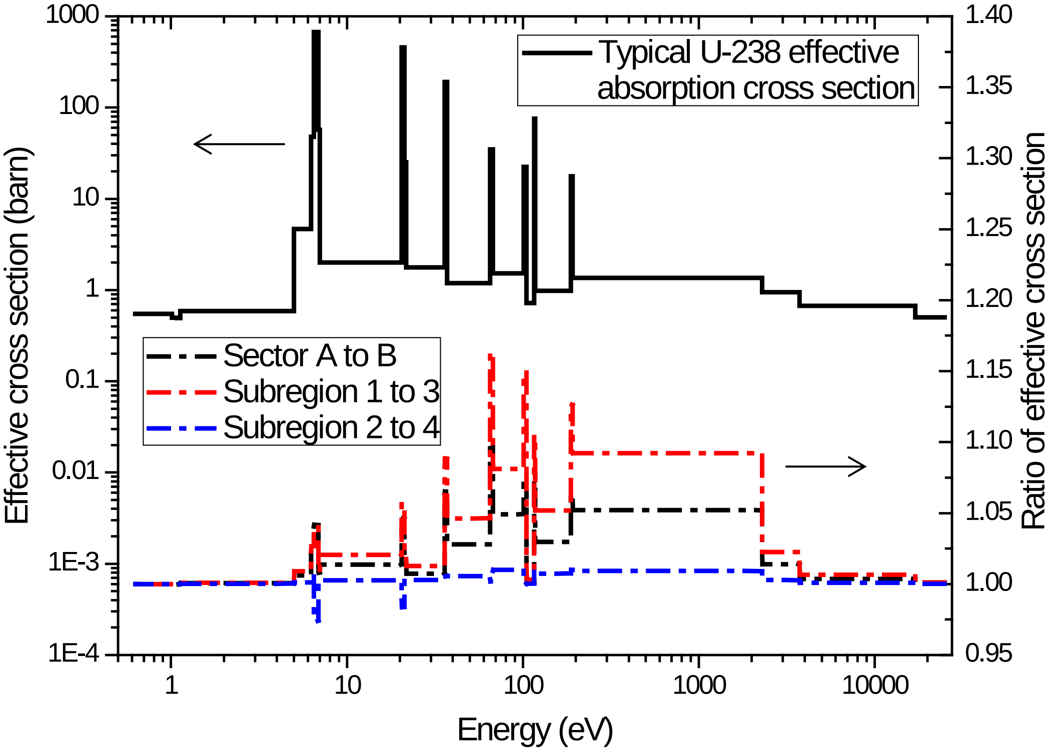

Figure 5.38 Comparison of azimuthally dependent cross sections of MCNP results

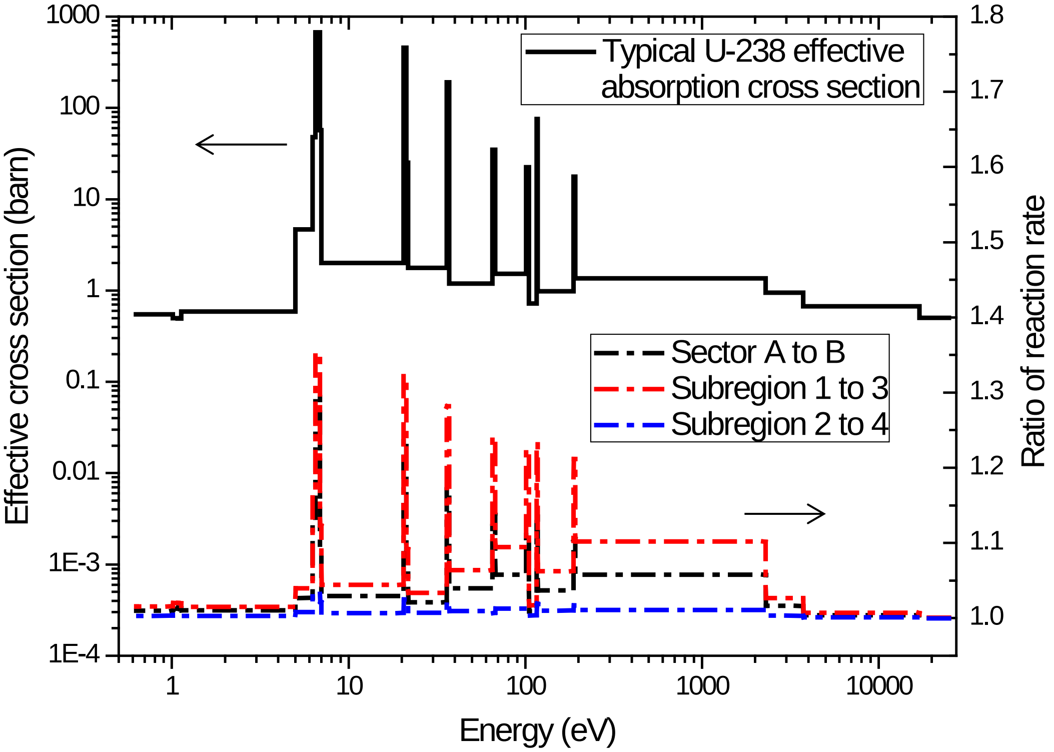

Figure 5.39 Comparison of azimuthally dependent reaction rates of MCNP results

Next, the same case is computed by DeCART using the subgroup method, ESSM and ESSM-X. Although the effective cross sections of the subgroup method and ESSM are biased in the radial direction, the azimuthal variation of the cross sections is still examined by comparing the ratio of effective cross sections for different subregions. The option of azimuthally dependent cross section mesh is turned on in DeCART so that each azimuthal zone of the fuel ring has its own equivalence cross section computed from the flux of that zone. The quasi-1D slowing-down equation is solved for each sector of the fuel instead of the whole fuel so that the computing time is a factor of *m* larger than the azimuthally independent calculation, where *m* is the number of azimuthal zones. Figure 5.40 compares the cross section ratios of Sector A to Sector B for the three methods with those from MCNP. For most resonance groups, ESSM and ESSM-X partially resolve the azimuthal variation of effective cross section, but the ratio is underestimated. The subgroup method gives better agreement with the MCNP results. Figure 5.41 shows the same comparison for reaction rates. It is worth pointing out that relatively good ratios of reaction rates are obtained by ESSM and ESSM-X in spite of the biased ratios of the effective cross section, especially for the large resonances. The flux difference of the azimuthal zones appears to be more important than the difference of effective cross sections in accounting for the reaction rate difference, so the results of ESSM and ESSM-X are acceptable with regard to the reaction rate calculation.

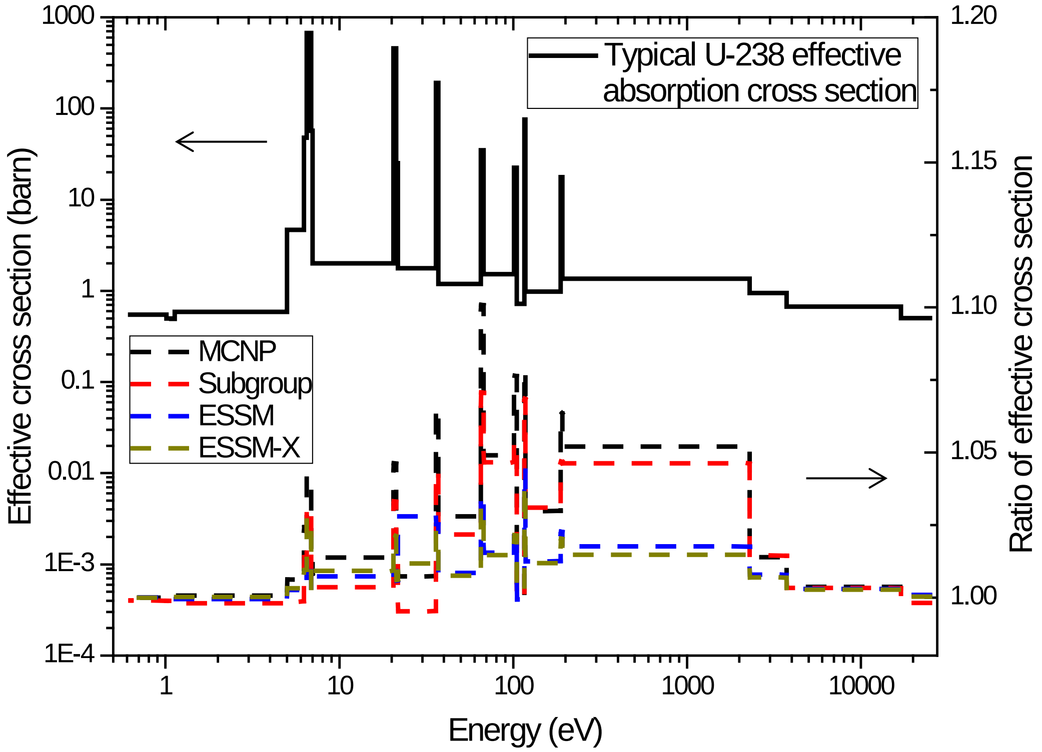

Figure 5.40 Comparison of azimuthally dependent cross sections (Sector A/Sector B)

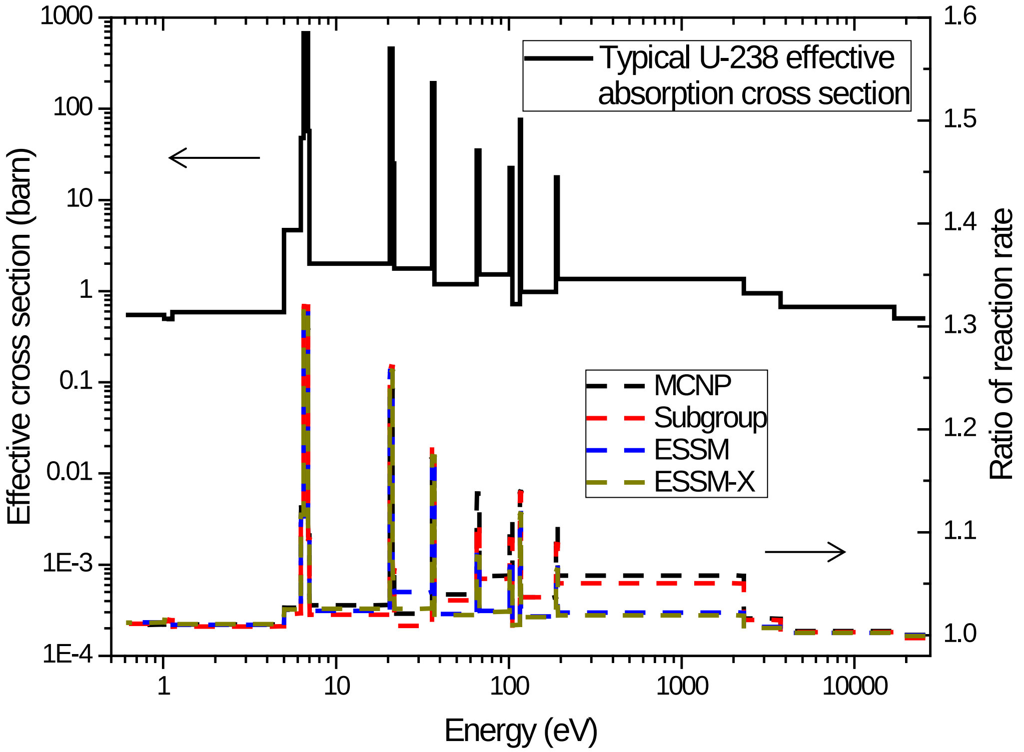

Figure 5.41 Comparison of azimuthally dependent reaction rates (Sector A/Sector B)

A similar comparison regarding the ratio of Subregion 1 to Subregion 3 is presented in Figure 5.42 and Figure 5.43. Still, ESSM and ESSM-X underestimate the azimuthal effect with regard to the effective cross section, but predict acceptable ratios for the absorption rates.

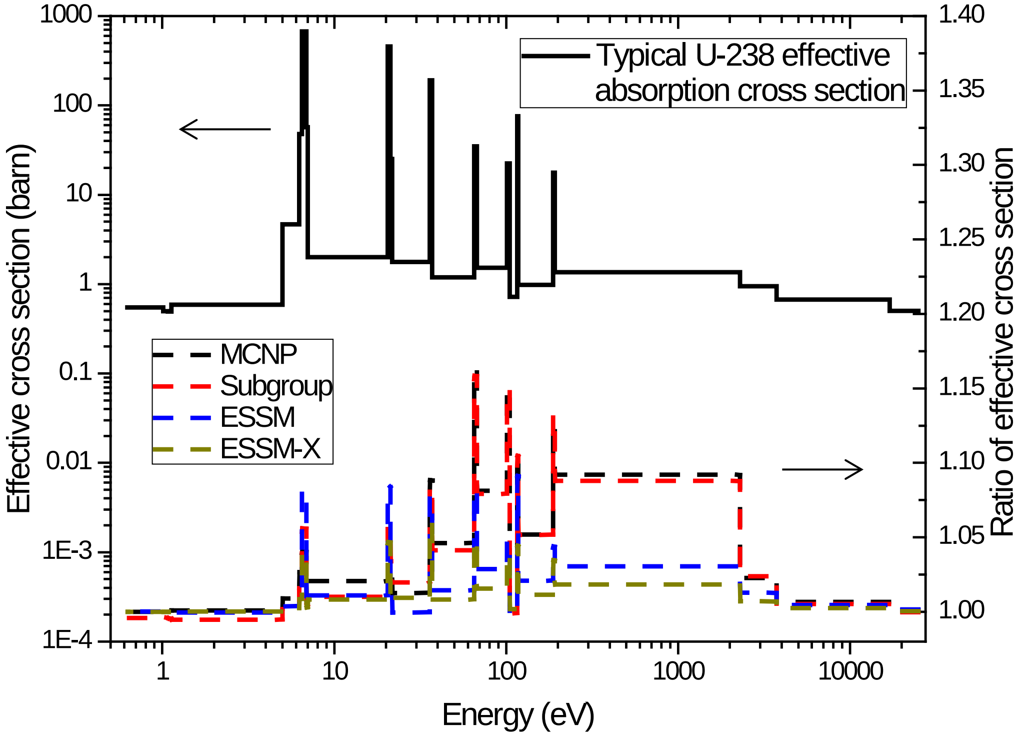

Figure 5.42 Comparison of azimuthally dependent cross sections (Subregion 1/Subregion 3)

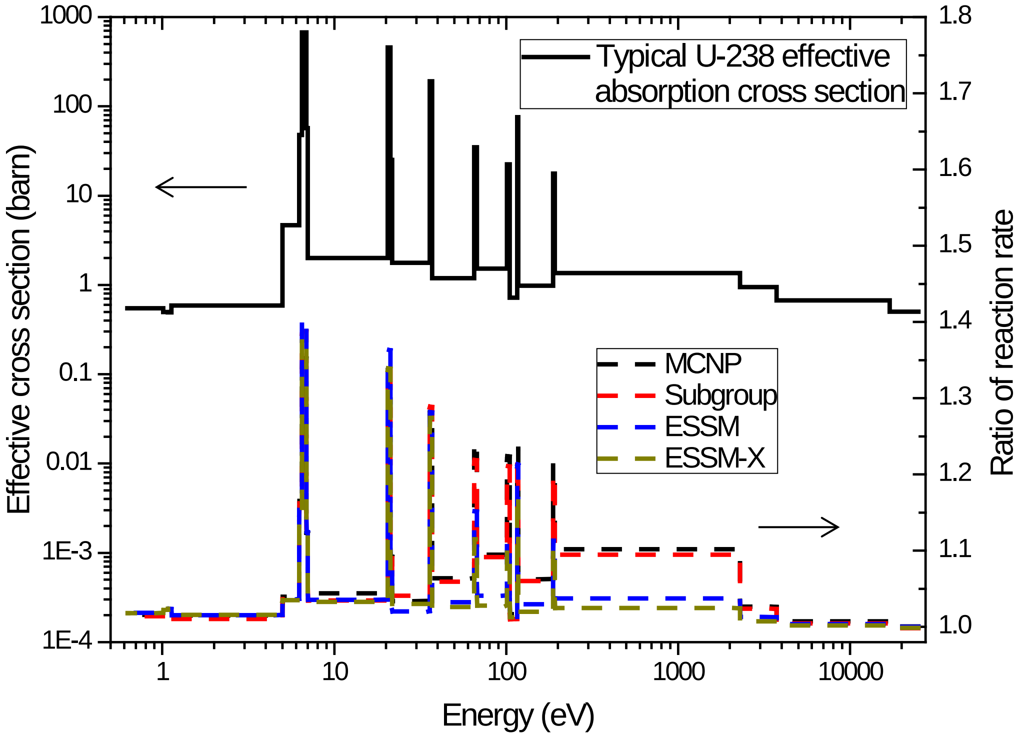

Figure 5.43 Comparison of azimuthally dependent reaction rates (Subregion 1/Subregion 3)

Since the subgroup method properly predicts the reaction rates of azimuthal subregions, the subgroup method is used to investigate the azimuthal dependence of depletion. Starting with the same case in Figure 5.36, the depletion calculation is performed by DeCART and the plutonium concentrations during depletion are plotted in Figure 5.44-Figure 5.47. For the azimuthal subregions near the fuel surface, Figure 5.44 and Figure 5.45 show that both Pu-239 and Pu-240 concentrations are predicted >10% more in Subregion 1 than Subregion 3 at a burnup of 31.2GWd/tU. This effect is more or less smeared out over each sector of the fuel, so the azimuthal difference of the whole sector is not that large, as shown in Figure 5.46 and Figure 5.47. Therefore, the results suggest turning on the azimuthally dependent calculation for fuel pins near a water hole or reflector, especially when the radial variation of reaction rates is also taken into account.

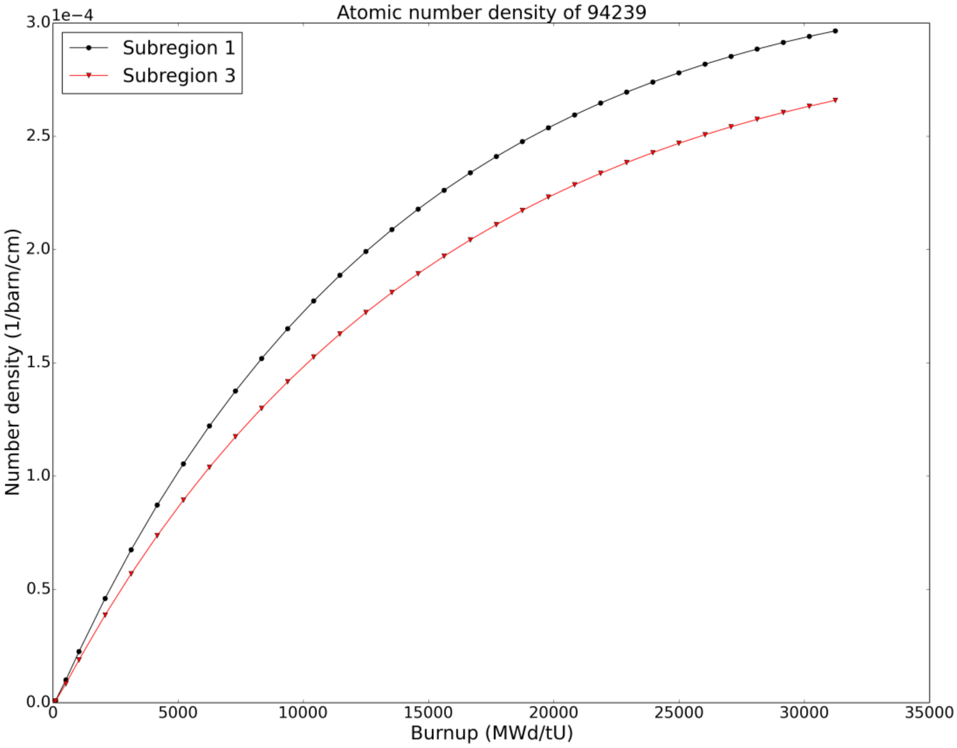

Figure 5.44 Pu-239 content of the azimuthal subregions

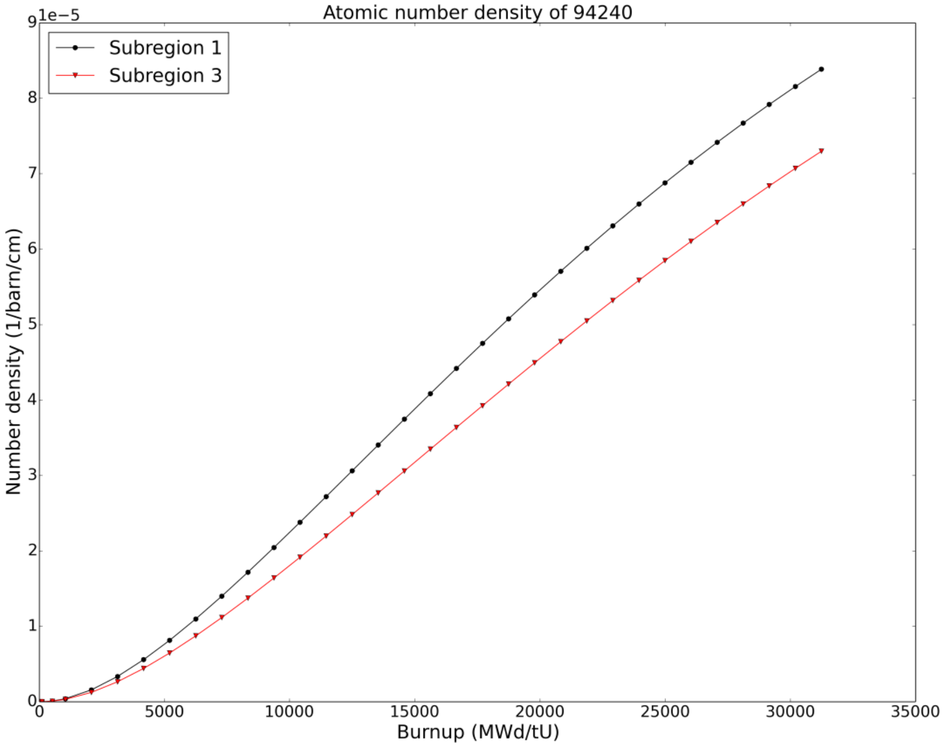

Figure 5.45 Pu-240 content of the azimuthal subregions

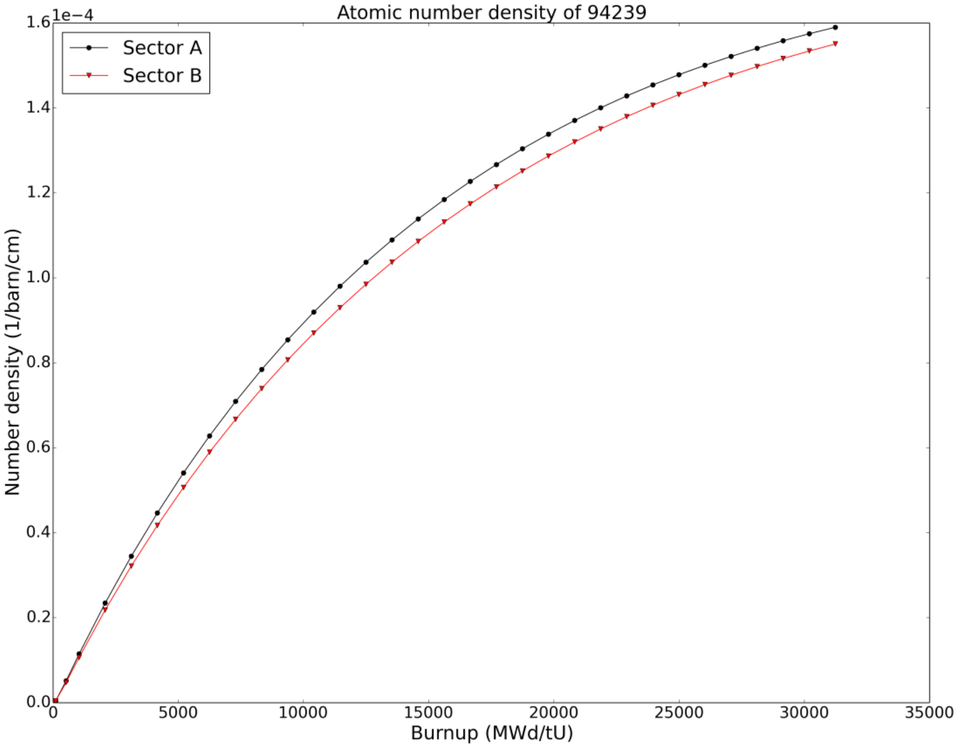

Figure 5.46 Pu-239 content of the azimuthal sectors

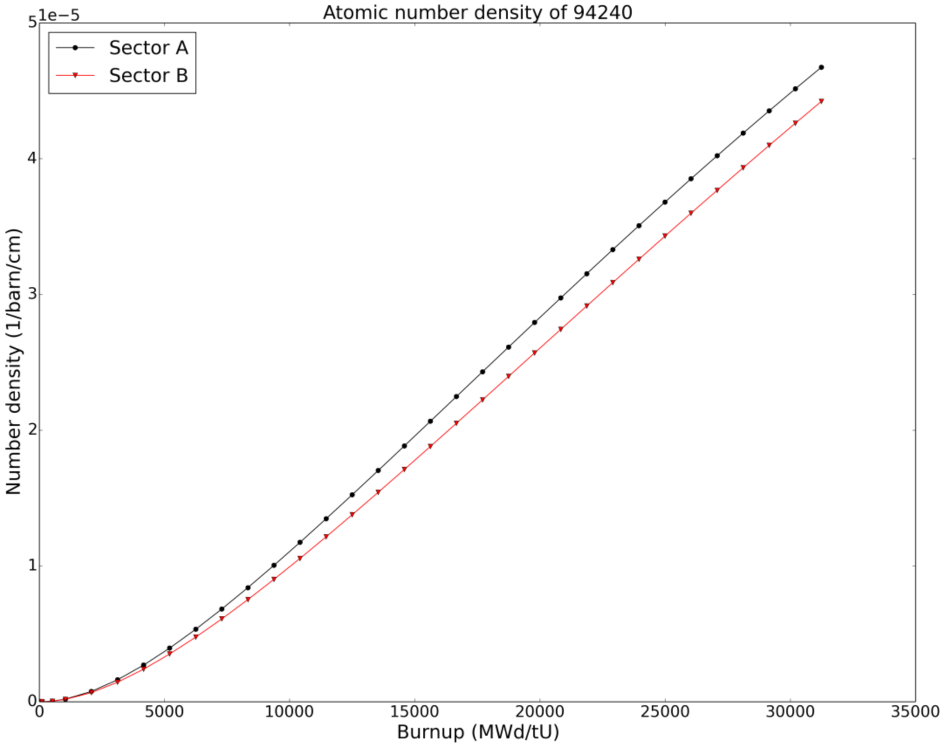

Figure 5.47 Pu-240 content of the azimuthal sectors

5.5 Summary

A comparison of the three resonance methods on the performance of modeling the important resonance physics is summarized in Table 5-11. #1 is the base case of an infinite fresh UO2 lattice without fuel subdivision. The subgroup method and ESSM cannot accurately model the resonance interference, which is however, not very significant for fresh fuel material, thus ‘acceptable’ results are expected. For #2, we have shown that ESSM has large error in the radially dependent reaction rates (15%-25% off at surface ring), while the results of the subgroup method are acceptable (5% off at surface ring). Since #3 is associated with #2, ESSM is not able to model the non-uniform temperature effect correctly. The subgroup method lacks a theoretical foundation to account for non-uniform fuel temperature, so larger errors are shown compared to the uniform temperature case. When the material composition becomes complicated, say MOX fuel or Gd fuel, the subgroup method and ESSM fail to model the interference effect, which is more important in those cases than the case of fresh fuel. Therefore, the results of the subgroup method and ESSM turn out to be problematic for #4. Based on the numerical results, the performance of resonance methods in treating lattice heterogeneity is summarized in #5 and #6. All the three methods have good performance with moderate heterogeneity, where (1) extra coolant is included, or (2) the difference in pins is not significant. Only the subgroup method has acceptable results for the problems with strong heterogeneities, because the subgroup method ignores the absorption of isotopes in other categories when the FSP is performed for the category in question. This indicates that the high order interference effect between different pins is better to be ignored than improperly modeled using the average effective absorption. Finally, the subgroup method is able to compute azimuthally-dependent effective cross sections correctly while ESSM and ESSM-X can partially resolve it although the reaction rates are good for all three methods.

Table 5-11 Comparison of resonance methods on modeling the important physics

#	**Important Physics**	**Subgroup**	**ESSM**	**ESSM-X**
1	Uniform infinite lattice, simple fuel comp., single fuel reg.	O	O	√
2	Radially dependent self-shielding	O	×	√
3	Non-uniform fuel temperature	×	×	√
4	Complex material composition	×	×	√
5	Moderate heterogeneities (water gap/hole, Gd fuel, zoned fuel)	√	√	√
6	Strong heterogeneities (AIC rod, mixed MOX and UO2 Assembly)	O	×	×
7	Azimuthal dependent self-shielding	√	O	O

√ good O acceptable × problematic

Chapter 6

Summary and Conclusion

6.1 Summary of Work

This thesis begun with the introduction of multigroup theory, which had been proven an effective way for solving neutron transport equation and been widely used in reactor core analysis. However, due to the complicated energy dependence of the cross sections in the resonance energy range, the energy and spatial resonance self-shielding phenomena complicate the procedure of preparing multigroup cross sections which are expected to be sufficiently consistent with the continuous-energy solution. Two types of approaches had been developed to perform the resonance self-shielding calculation, i.e., direct slowing-down calculation and integral table based methods which were discussed in Chapter 2 and Chapter 3, respectively. The direct slowing-down method attempts to fully resolve the resonance behavior by using the point-wise or ultrafine group cross section data. Because of the computational burden, the application of the direct slowing-down method is limited to local geometries such as a pin cell or a single assembly. The integral table based methods, on the other hand, performs self-shielding calculation using pre-computed multigroup integral tables, which indicates a significant computing time savings compared to the direct slowing-down method. However, to derive those integral tables, a number of approximations have to be applied, leading to a few limitations of the integral table based methods on treating distributed self-shielding within the fuel rod, non-uniform temperature effect and resonance interference.

The current work developed a fusion method utilizing the advantages of both approaches in Chapter 4. The method performs the conventional ESSM without subdivision of the fuel region to capture the inter-pin shielding effect. The resultant self-shielded cross sections are modified by correction factors incorporating the intra-pin effects of radial variation of the shielded cross section, radial temperature distribution and resonance interference. A quasi-1D slowing-down equation is developed to calculate such correction factors. Instead of using explicit boundary conditions, boundary conditions are incorporated implicitly in the local quasi-1D calculation by modifying the equivalence cross section. Other efforts are made to improve the efficiency of quasi-1D slowing-down solver so that it computes the neutron spectra much faster than the standard 1-D slowing-down calculation.

The resonance calculation was performed for a set of benchmark problems developed in Chapter 5. Three resonance self-shielding methods, i.e., subgroup method, ESSM and ESSM-X are compared with MCNP reference solutions. Numerical results show that ESSM-X is capable of resolving the spatially dependent self-shielding of fuel annuli. The error in the U-238 absorption rate over the resonance energy range for the outermost ring is reduced from 15%-25% (ESSM) and 5% (subgroup) to less than 1% by ESSM-X. In addition, the energy dependent reaction rates of non-dominant isotopes such as U-235, Pu-239, Pu-240 are greatly improved by explicitly accounting for the resonance interference. The accuracy of the new method is not affected by moderate heterogeneity (water hole/gap, Gd fuel, zoned fuel). For problems with strong heterogeneities (AIC rod, mixed UO2 and MOX fuel), slightly biased reaction rates are observed for some groups with small resonance absorption at the pins near the heterogeneity, which is primarily due to the assumption of similar pins in the ESSM derivation. However, the overall eigenvalue still agrees well with the reference solution. As shown in the assembly cases, the new method should be ready for full core configurations. In addition, a straightforward extension of the method is sufficient for treating the azimuthal dependent self-shielding effect.

The computational efficiency of ESSM-X was examined. The resonance calculation in ESSM-X costs an additional 30%~100% computing time over that for ESSM, depending on the size of energy mesh and material complexity. For the worst case, the total computing time of ESSM-X rises by 20% compared to that of ESSM. For the assembly cases, ESSM-X may save total computing time since the equivalence cross section is calculated for each single mesh of the fuel, which converges much faster than those for the fuel subregions using ESSM. The memory demand of the slowing-down calculation depends primarily on the number of isotopes and the range of temperatures in the problem. Since the slowing-down calculations for the fuel pins are independent, the memory requirement of the model does not increase with the geometrical size of the problem. Overall, the new method is very promising for the deterministic resonance treatment of direct transport calculation.

6.2 Future Work

A few issues have been identified for further study. First, since ESSM has slightly biased results on treating problems with strong heterogeneities, refinement of the method is required if one wants to further improve local reaction rates. The possibilities could be to (1) ignore the high-order inter-pin interference for different isotopes by performing the fixed source problem using category concept, which is similar to the subgroup strategy; (2) resolve the effect using a slowing-down model with multiple-pin consideration. In practice, Option (1) would be easier to incorporate into the current implementation of ESSM. Either category dependent ESSM or subgroup method could be options to compute the effective cross section of the fuel region with a single mesh. An additional ESSM iteration without category separation would then be needed to produce the region-wise equivalence cross sections for the quasi-1D slowing-down calculation. Second, solving the quasi-1D slowing down equation could be expensive when the number of isotopes becomes very large (depleted fuel), because the scattering source has to be accumulated independently for each isotope. A possible approach for saving computing time is to combine the isotopes of similar atomic weights for the scattering source calculation, since the asymptotic scattering kernel is only dependent on the atomic weight. Further investigation is required to devise this isotopic combination scheme to accelerate the scattering source calculation given the accuracy of the slowing-down calculation is guaranteed. Third, extensive analysis should be performed to investigate the axial effect on the resonance calculation. Currently, the resonance calculation is performed independently for each 2-D plane with reflective axial boundary conditions. However, the axial effect might become non-negligible for the boundary nodes with reflector instead of reflecting boundary conditions. Improvement to account for axial heterogeneity might be needed if the boundary nodes have significant errors with the current methodology.

Some of the assumptions applied at the starting point of the slowing-down equation could also be replaced by ‘true’ physics in the future work. In the current work, the epithermal up-scattering is neither considered in the multigroup library generation, nor in the quasi-1D slowing-down solver. As the asymptotic scattering treatment could bias the fuel temperature coefficient by more than 10%, the epithermal up-scattering should be modeled for heavy nuclides such as U-238 to improve the effective scattering and absorption. Additionally, if one wants to extend the new method for fast reactor applications, the fission source might be considered for the slowing-down calculation in an extended energy range. In the meantime, the current work does not consider the unresolved resonance separately from the resolved resonance for the slowing-down calculation. Since the CE cross section library includes infinite diluted data in the unresolved resonance energy range, probability table method should be utilized in order to shield the unresolved resonance cross section, which becomes important for fast reactor applications.

Appendix A

Carlvik Method for Computing Collision Probability of 1-D Cylindrical Geometry

It is customary to eliminate the axial coordinate to facilitate the calculation of collision probability for 1-D cylindrical geometry. First we consider the probability that neutrons emitted in a small azimuthal angle of $d\alpha$ will travel through a path of R without any collision. As shown in Figure A.1, by introducing the neutron path projected on to the plane perpendicular to z, where the projected length is $t = R\sin\theta$ or $\tau = \rho\sin\theta$ in optical length, the probability of uncollided neutron can be written as $\exp(-\tau / \sin\theta)$.

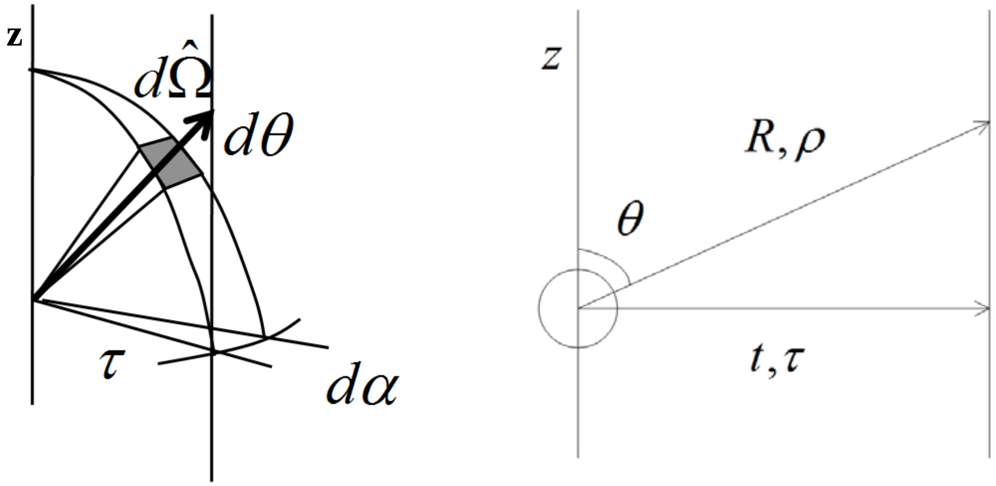

Figure A.1 Elimination of coordinate z for 1-D cylindrical calculation

Assuming the neutrons are emitted from an isotropic line source S along z, the neutrons emitted into $d\alpha$ are given as

$$N\left(d\alpha\right)=S\frac{d\alpha}{2\pi} \tag{A.1}$$

Also, we can evaluate the number of neutrons emitted into $d\alpha$ and horizontally reaching τ without any collision by integrating neutrons emitted into $d\Omega$ and horizontally reaching τ without any collision over all possible θ

$$N_{uncol}\left(d\alpha\right)=S\frac{d\alpha}{4\pi}\int_0^{\pi}e^{-\tau/\sin\theta}\sin\theta d\theta \tag{A.2}$$

Therefore, the probability of neutron travelling by an optical length of τ at the projection plane without collision is given as

$$\begin{aligned} P_{un-col}(\tau)&=\frac{N_{uncol}\left(d\alpha\right)}{N\left(d\alpha\right)}=\frac{1}{2}\int_0^{\pi}e^{-\tau/\sin\theta}\sin\theta d\theta \\ &=\int_0^{\pi/2}e^{-\tau/\sin\theta}\sin\theta d\theta=\int_0^{\pi/2}e^{-\tau/\cos\theta}\cos\theta d\theta=Ki_2(\tau) \end{aligned} \tag{A.3}$$

where $Ki_2(x)$ is the Bickley function of second order. Note that θ dependence has been embedded into the uncollided probability $P_{un-col}(\tau)$. The following content will focus on the collision probability calculation in the projection plane, which was developed by Carlvik [57].

Consider an azimuthally symmetric problem, in which the physical quantities only depend on radius *r*. As shown in Figure A.2, for a unit isotropic neutron source in V_i, the first flight collision probability from subregion *i* to *j* is equal to the collision probability computed by the shadowed quadrant of subregion *i* to *j* due to the geometrical symmetry. If we consider a thin strip Δy in which $t_i(y)\Delta y$ isotropic neutron sources are born, the probability that the neutron flies to the left and has its first collision in subregion *j* can be written as

$$P_{i\to j}^{left}(y)=\frac{1}{2t_i(y)\Delta y}\left(\int_0^{t_i(y)}Ki_2(\tau_{i,j-1}^{-}+\tau_{i,i-1}^{-}-\Sigma_i t)dt-\int_0^{t_i(y)}Ki_2(\tau_{i,j}^{-}+\tau_{i,i-1}^{-}-\Sigma_i t)dt\right)\Delta y \tag{A.4}$$

For the first integral, let $l=\tau_{i,j-1}^{-}+\tau_{i,i-1}^{-}-\Sigma_i t$

$$\int_0^{t_i(y)} Ki_2(\tau^-_{i,j-1}+\tau^-_{i,i-1}-\Sigma_i t)dt = \frac{1}{\Sigma_i}\int_{\tau^-_{i,j-1}}^{\tau^-_{i,j-1}+\tau^-_{i,i-1}} Ki_2(l)dl = \frac{1}{\Sigma_i}\int_{\tau^-_{i,j-1}}^{\tau^-_{i-1,j-1}} Ki_2(l)dl \qquad \text{(A.5)}$$

Using $\int_a^b Ki_n(x)dx = Ki_{n+1}(a) - Ki_{n+1}(b)$,

$$\int_0^{t_i(y)} Ki_2(\tau^-_{i,j-1}+\tau^-_{i,i-1}-\Sigma_i t)dt = \frac{1}{\Sigma_i}\left(Ki_3(\tau^-_{i,j-1}) - Ki_3(\tau^-_{i-1,j-1})\right) \qquad \text{(A.6)}$$

Similarly, the second integral can be written as

$$\int_0^{t_i(y)} Ki_2(\tau^-_{i,j}+\tau^-_{i,i-1}-\Sigma_i t)dt = \frac{1}{\Sigma_i}\left(Ki_3(\tau^-_{i,j}) - Ki_3(\tau^-_{i-1,j})\right) \qquad \text{(A.7)}$$

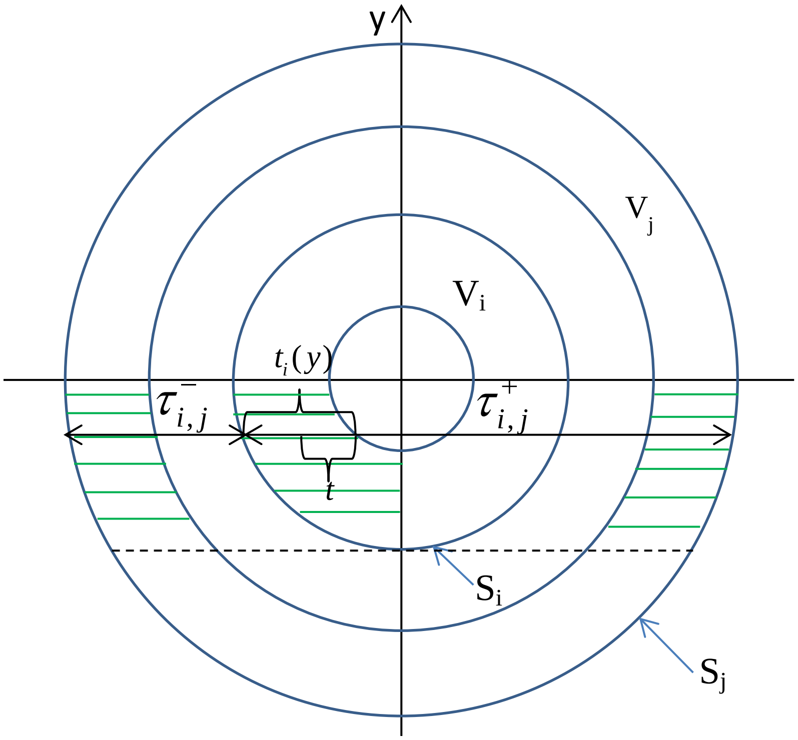

Figure A.2 Collision probability on 1-D cylindrical geometry

Definition:

V_i - the volume of subregion *i*

S_i - the surface boundary of subregion *i*

t_i - the physical thickness of the neutron travels through in the quadrant of subregion *i*

t - the variable of physical length

$\tau_{i,j}^{-}$- the shorter optical length from subregion boundary *i* to *j*

$\tau_{i,j}^{+}$- the longer optical length from subregion boundary *i* to *j*

y - the variable of vertical location of a chord

All the optical and physical lengths are a function of y, but we omit it for simplicity

Therefore,

$$P_{i\to j}^{left}(y) = \frac{1}{2\Sigma_i t_i(y)}\left(Ki_3(\tau_{i,j-1}^{-}) + Ki_3(\tau_{i-1,j}^{-}) - Ki_3(\tau_{i-1,j-1}^{-}) - Ki_3(\tau_{i,j}^{-})\right) \tag{A.8}$$

Using the same approach, the probability that neutron flies to the right and has the first collision in subregion *j* is written as

$$P_{i\to j}^{right}(y) = \frac{1}{2\Sigma_i t_i(y)}\left(Ki_3(\tau_{i-1,j-1}^{+}) + Ki_3(\tau_{i,j}^{+}) - Ki_3(\tau_{i-1,j}^{+}) - Ki_3(\tau_{i,j-1}^{+})\right) \tag{A.9}$$

The overall collision probability from subregion *i* to *j* is obtained by integrating the sum of Equation (A.8) and Equation (A.9) over the volume of quadrant,

$$P_{i\to j} = \frac{1}{2}\int_0^{R_i}\left[P_{i\to j}^{left}(y) + P_{i\to j}^{right}(y)\right]\frac{t_i(y)dy}{V_i/4} \tag{A.10}$$

where R_i is the radius of ring *i*.

The fuel escape probability of subregion *i* can be obtained by slightly modifying Equation (A.4),

$$P_{i,esc}^{left}(y) = \frac{1}{2t_i(y)\Delta y}\left(\int_0^{t_i(y)} Ki_2(\tau_{i,j}^{-} + \tau_{i,i-1}^{-} - \Sigma_i t)dt\right)\Delta y \tag{A.11}$$

By substituting the variable and applying $\int_a^b Ki_n(x)dx = Ki_{n+1}(a) - Ki_{n+1}(b)$

$$P_{i,esc}^{left}(y) = \frac{1}{2\Sigma_i t_i(y)}\left(Ki_3(\tau_{i,j}^-) - Ki_3(\tau_{i-1,j}^-)\right) \tag{A.12}$$

The escape probability on the right flying neutrons is given as

$$P_{i,esc}^{right}(y) = \frac{1}{2\Sigma_i t_i(y)}\left(Ki_3(\tau_{i-1,j}^+) - Ki_3(\tau_{i,j}^+)\right) \tag{A.13}$$

So the overall escape probability of subregion *i* is given as

$$P_{i,esc} = \frac{1}{2}\int_0^{R_i}\left[P_{i,esc}^{left}(y) + P_{i,esc}^{right}(y)\right]\frac{t_i(y)dy}{V_i/4} \tag{A.14}$$

The integration over y for Equation (A.10) and Equation (A.14) are usually split into intervals from R_i to R_{i+1}, in which each integration is numerically treated by Gauss-Jacobi quadrature. This completes the calculation of region to region collision probability and region-wise escape probability.

Appendix B

A Problem-Dependent Energy Mesh Scheme for Quasi-1D Slowing-down Calculation

Depending on the number of isotopes and temperatures existing in the problem, the CE cross section data are heavily used in the correction method. Since the cross section data of each isotope at a specific temperature has its own energy mesh, several issues need to be addressed properly:

a. What energy mesh is used to solve the problem? Since the slowing-down calculation is performed for each pin cell, is it better to unionize the energy mesh for each pin cell or unionize the energy mesh for the whole problem?
b. What is a better scheme of cross section interpolation for temperature? Is it better to compute and store the cross section sets for all the temperatures occurring in the problem before slowing-down calculation, or only store the few cross section sets of temperatures available in the library and do the interpolation on the fly of slowing-down?

The current work manipulates the CE data as follows:

a. Scan the whole problem and find all isotopes in the fuel regions.
b. Read the cross section data of these isotopes from the CE library at several discrete temperatures according to the library availability (say 296K, 600K, 900K, 1200K and 2400K).
c. Map the cross section of each isotope to the energy mesh of the lowest temperature (say 296K) so that every isotope ends up with a uniform energy mesh of cross sections for different temperatures.
d. Generate a union mesh for each fuel material composition using an approach similar to CENTRM. The energy meshes of isotopes in a material are unionized

and thinned in such a manner that the macroscopic total cross section can be linearly interpolated according to a specific tolerance.

e. Combine the energy meshes of all fuel materials to a final union mesh ‘M’ (this will be used for slowing-down calculation). Alternatively, different union mesh ‘M_i’ can be produced for different pin *i*. The former is better for fresh fuel case where the number of different materials (composition & temperature) is relatively small, while the latter is better for depleted case or with thermal feedback where the number of different materials is large.
f. On the fly of slowing-down calculation, interpolation is needed to obtain the cross section at a specific temperature on the union mesh ‘M’ or ‘M_i’.
g. When collapsing the MG cross section of an isotope using point-wise spectrum, the union mesh ‘M’ or ‘M_i’ should be combined with the cross section energy mesh of the isotope in order to retrieve the subtleties of cross section variation upon energy for the isotope.

This procedure is open to discussion, as it is very important to the efficiency and memory requirement of the method. Parallelization of the pin cell slowing-down calculation might require further design of this procedure.

Bibliography

1. G. I. Bell and S. Glasstone, *Nuclear Reactor Theory*, Van Nostrand Reinhold Inc., U.S. (1970).
2. K. Shibata, O. Iwamoto, T. Nakagawa, N. Iwamoto, A. Ichihara, S. Kunieda, S. Chiba, K. Furutaka, N. Otuka, T. Ohsawa, T. Murata, H. Matsunobu, A. Zukeran, S. Kamada, and J. Katakura, "JENDL-4.0: A New Library for Nuclear Science and Engineering," *J. Nucl. Sci. Technol.*, **48**, 1 (2011).
3. J. J. Duderstadt and L. J. Hamilton, *Nuclear Reactor Analysis*, John Wiley & Sons, U.S. (1976).
4. F. Leszczynski, "Neutron Resonance Treatment with Details in Space and Energy for Pin Cells and Rod Clusters," *Ann. Nucl. Energy*, **14**, 589 (1987).
5. M. L. Williams and M. Asgari, "Computation of Continuous-Energy Neutron Spectra with Discrete Ordinates Transport Theory," *Nucl. Sci. Eng.*, **121**, 173 (1995).
6. K. S. Kim and S. G. Hong, "The Method of Characteristics Applied to Solving Slowing Down Equation to Estimate the Self-shielded Resonance Cross Sections with an Explicit Geometrical Effect," *Ann. Nucl. Energy*, **38**, 438 (2011).
7. K. S. Kim and M. L. Williams, "The Method of Characteristics for 2-D Multigroup and Pointwise Transport Calculations in SCALE/CENTRM," *Proc. PHYSOR-2012*, Knoxville, TN, April 15-20 (2012).
8. Z. Zhong, T. J. Downar and Y. Xu, "Continuous-Energy Multidimensional SN Transport for Problem-Dependent Resonance Self-Shielding Calculations," *Nucl. Sci. Eng.*, **154**, 190 (2006).
9. I. I. Bondarenko, *Group Constants for Nuclear Reactor Calculations*, Consultants Bureau, New York (1964).
10. R. J. J. Stamm'ler and M. J. Abbate, *Methods of Steady-state Reactor Physics in Nuclear Design*, Academic Press, London (1983).
11. J. R. Askew, F. J. Fayers, and P. B. Kemshell, "A General Description of the Lattice Code WIMS," *J. British Nucl. Energy Soc.*, **5**, 564 (1966).
12. L. B. LEVITT, "The Probability Tables Method for Treating Unresolved Neutron Resonances in Monte-Carlo Calculations," *Nucl. Sci. Eng.*, **49**, 450 (1972).
13. D. E. Cullen, "Application of the Probability Table Method to Multigroup Calculations of Neutron Transport," *Nucl. Sci. Eng.* **55**, 387 (1974).
14. A. Hébert, "A Review of Legacy and Advanced Self-Shielding Models for Lattice Calculations," *Nucl. Sci. Eng.*, **155**, 310 (2007).

15. S. G. Hong and K. S. Kim, “Iterative Resonance Self-Shielding Methods Using Resonance Integral Table in Heterogeneous Transport Lattice Calculations,” *Ann. Nucl. Eng.*, **38**, 32 (2011).
16. M. L. Williams and K. S. Kim, “The Embedded Self-shielding Method,” *PHYSOR-2012*, Knoxville, TN, April 15-20, (2012).
17. K. S. Kim and Mark L. Williams, “Preliminary Assessment of Resonance Interference Treatment by Using 0-D Slowing Down Calculation in the Embedded Self-Shielding Method,” *Trans. Am. Nucl. Soc.*, **107**, 1128 (2012).
18. Y. Liu, W. R. Martin, K. S. Kim and M. L. Williams, “Modeling Resonance Interference by 0-D Slowing-down Solution with Embedded Self-shielding Method,” *Proc. M&C-2013*, Sun Valley, Idaho, May 5-9 (2013).
19. D. Lee, K. Smith and J. Rhodes, “The Impact of ^{238}U Resonance Elastic Scattering Approximations on Thermal Reactor Doppler Reactivity,” *Ann. Nucl. Energy*, **36**, 274 (2009).
20. S. Z. Ghrayeb, A. M. Ougouag, M. Ouisloumen and K. N. Ivanov, “Multi-group Formulation of the Temperature-dependent Resonance Scattering model and its Impact on Reactor Core Parameters,” *Ann. Nucl. Energy*, **63**, 751 (2014).
21. N. Sugimura and A. Yamamoto, “Resonance Treatment Based on Ultra-fine-group Spectrum Calculation in the AEGIS Code,” *J. Nucl. Sci. Technol.*, **44**, 958 (2007).
22. B. Meftah and R. A. Karam, “Space, Energy and Anisotropy Effects on ^{238}U Effective Capture Cross Sections in the Resonance Region,” *Ann. Nucl. Energy*, **11**, 59 (1984).
23. P. H. Kier and A. A. Robba, “RABBLE, A Program for Computation of Resonance Absorption in Multiregion Reactor Cells,” ANL-7326, Argonne National Laboratory (1967).
24. D. G. Cacuci (Ed.), *Handbook of Nuclear Engineering*, Lattice Physics Computations, Chapter 9, Springer, New York (2010).
25. R. Goldstein and E. R. Cohen, “Theory of resonance absorption of neutrons,” *Nucl. Sci. Eng*., **13**, 132 (1962).
26. Z. Gao, Y. Xu and T. J. Downar, “The Treatment of Resonance Interference Effects in the Subgroup Method,” *Ann. Nucl. Energy.*, **38**, 995 (2011).
27. A. M. Weinberg and E. P. Wigner, *The Physical Theory of Neutron Chain Reactors*, University of Chicago Press, Chicago (1958).
28. G. I. Bell, “Theory of Effective Cross Sections,” LA-2322, Los Alamos National Laboratory (1959).
29. I. Carlvik, “A Simplified Treatment of Spectrum Hardening in a Fuel Rod Caused by Selective Absorption,” RFR-174, AB Atomenergi, Stockholm, Sweden (1962).
30. M. M. Levine, “Resonance Integral Calculations for ^{238}U Lattices,” *Nucl. Sci. Eng.*, **16**, 271 (1963).
31. Y. A. Chao and A. S. Martinez, “On Approximations to the Neutron Escape Probability from an Absorbing Body,” *Nucl. Sci. Eng.*, **66**, 254 (1978).

32. I. Carlvik and B. Pershagen, *The Dancoff Correction in Various Geometries,* AB Atomenergi, Stockholm, Sweden (1959).

33. N. Sugimura and A. Yamamoto, “Evaluation of Dancoff Factors in Complicated Geometry using the Method of Characteristics,” *J. Nucl. Sci. Technol.*, **43**, 1182 (2006).

34. S. Feher, J. E. Hoogenboom, P. F. A. de Leege, and J. Valko, “Monte Carlo Calculation of Dancoff Factors in Irregular Geometries”, *Nucl. Sci. Eng.*, **117**, 227 (1994).

35. B. Fredin, U. Decher, A. Jonsson, A. Ferri and R. J. J. Stamm’ler, “Processing and Application of ENDF/B-VI in LWRs: Critical Experiments”, *Trans. Am. Nucl. Soc.*, **73**, 419 (1995).

36. R. J. J. Stamm’ler, et al., *HELIOS Methods,* Studsvik Scandpower (2003).

37. K. S. Kim, C. C. Lee, M. H. Chang and S. Q. Zee, “Monte Carlo Resonance Treatment for the Deterministic Transport Lattice Code”. *J. Korean Nucl. Soc.*, **35**, 581 (2003).

38. H. G. Joo, G. Y. Kim and L. Pogosbekyan, “Subgroup Weight Generation Based on Shielded Pin-cell Cross Section Conservation,” *Ann. Nucl. Energy*, **36**, 859 (2009).

39. A. Hébert and M. Coste, “Computing Moment-Based Probability Tables for Self-Shielding Calculations in Lattice Codes”, *Nucl. Sci. Eng.*, **142**, 245 (2002)

40. G. Chiba and H. Unesaki, “Improvement of moment-based probability table for resonance self-shielding calculation,” *Ann. Nucl. Energy.*, **33**, 1141 (2006).

41. K. S. Kim and S. G. Hong, “A New Procedure to Generate Resonance Integral Table with an Explicit Resonance Interference for Transport Lattice Codes”, *Ann. Nucl. Energy.*, **38**, 118 (2011).

42. M. L. Williams, “Correction of Multigroup Cross Sections for Resolved Resonance Interference in Mixed Absorbers,” *Nucl. Sci. Eng*., **83**, 37 (1983).

43. K. Smith and B. Forget, “Challenges in the Development of High-Fidelity LWR Core Neutronics Tools,” *Proc. M&C-2013*, Sun Valley, Idaho, May 5-9 (2013).

44. C. Stoker and Z. Weiss, “Spatially Dependent Resonance Cross Sections in a Fuel Rod,” *Ann. Nucl. Energy.*, **23**, 765 (1996).

45. M. Williams and R. Raharjo, “Space-Dependent Resonance Self-shielding,” *Nucl. Sci. Eng.*, **126**, 19 (1997).

46. H. Matsumoto, M. Ouisloumen and T. Takeda, “Development of Spatially Dependent Resonance Shielding Method,” *J. Nucl. Sci Technol.*, **42**, 688 (2005).

47. W. J. M. de Kruijf and A. J. Janssen, “The Effective Temperature to be Used for Calculating Resonance Absorption in a $^{238}UO_2$ lump with nonuniform temperature profile,” *Nucl. Sci. Eng.*, **123**, 121 (1996).

48. H. G. Joo, B. S. Han, C. H. Kim and K. S. Kim, “Implementation of Subgroup Method in Direct Whole Core Transport Calculation Involving Nonuniform Temperature distribution,” *Proc. M&C-2005*, Palais des Papes, Avignon, France,

September 12-15 (2005).

49. C. A. Wemple, R. J. J. Stamm'ler and A. A. Ferri, "Improved Temperature-Dependent Resonance Treatment in HELIOS-1.9," *Trans. Am. Nucl. Soc.*, **96**, 657 (2007).
50. "Consortium for Advanced Simulation of Light Water Reactors (CASL)," http://www.casl.gov/.
51. H. G. Joo, J. Y. Cho, K. S. Kim, C. C. Lee, M. H. Chang and S. Q. Zee, "Methods and Performance of a Three-Dimensional Whole-Core Transport Code DeCART," *Proc. PHYSOR-2004*, Chicago, IL, April 25-29 (2004).
52. S. M. Bowman, "SCALE 6: Comprehensive Nuclear Safety Analysis Code System," *Nucl. Technol*. **174**, 126 (2011).
53. M. E. Dunn and N. M. Greene, "AMPX-2000: A Cross-Section Processing System for Generating Nuclear Data for Criticality Safety Applications," *Trans. Am. Nucl. Soc*., **86**, 118 (2002).
54. M. B. Chadwick, et al., "ENDF/B-VII.0: Next Generation Evaluated Nuclear Data Library for Nuclear Science and Technology," *Nucl. Data Sheets*, **107**, 2931 (2006).
55. X-5 Monte Carlo Team, "MCNP-A General Monte Carlo N-Particle Transport Code, Version 5", LA-UR-03-1987, Los Alamos National Laboratory (2000).
56. R. E. MacFarlane and D. W. Muir, "NJOY99.0 Code System for Producing Pointwise and Multigroup Neutron and Photon Cross Sections from ENDF/B Data," Report PSR-480/NJOY99.0, Los Alamos National Laboratory, New Mexico (2000).
57. I. Carlvik, "A Method for Calculating Collision Probabilities in General Cylindrical Geometry and Applications to Flux Distributions and Dancoff Factors," *Proc. Int. Conf. Peaceful Uses of Atomic Energy in Geneva*, **2**, 225, United Nations, New York (1965).